Photoluminescence Characterization of Cadmium Zinc Telluride

by

Mohamed Alshal
B.Sc., Mansoura University, 2016

A Thesis Submitted in Partial Fulfillment
of the Requirements for the Degree of

MASTER OF APPLIED SCIENCE

in the Department of Electrical and Computer Engineering

Supervisory Committee

Photoluminescence Characterization of Cadmium Zinc Telluride

by

Mohamed Alshal
B.Sc., Mansoura University, 2016

Supervisory Committee

Dr. Thomas Tiedje, Department of Electrical and Computer Engineering
Supervisor

Dr. Fayez Gebali, Department of Electrical and Computer Engineering
Departmental Member

Abstract

Supervisory Committee
Dr. Thomas Tiedje, Department of Electrical and Computer Engineering
Supervisor
Dr. Fayez Gebali, Department of Electrical and Computer Engineering
Departmental Member

The demand for wide bandgap semiconductors for radiation detector applications has significantly increased in recent years due to an ever-growing need for safeguard measures and medical imaging systems amongst other applications. The need for these devices to be portable and efficient, and to operate at room temperature is important for practical applications. For radiation detectors, the semiconductor materials are mainly required to have an optimal energy gap, high average atomic number, good electrical resistivity and charge transport properties as well as purity and homogeneity.

Cadmium zinc telluride (CZT) distinctly stands out among the other choices of semiconductor materials for radiation detector applications, due to its attractive material properties and the room temperature operation possibility.

A tremendous amount of research is being conducted to improve CZT technology and its implementation into more commercial systems. Applications of CZT detector technology in national security, high energy physics, nuclear spectroscopy, and medical imaging systems are of special interests. However, CZT devices still face challenges that need to be understood and overcome in order to have more efficient radiation detector systems. One such challenge lies in the understanding of the surfaces of CZT detectors and surface recombination effects on charge transport, charge collection efficiency, and detector performance. Another common issue is the degradation of CZT detectors due to the presence of defects which can act as traps for the charge carriers and cause incomplete

charge collection from the detectors. Thus, a major challenge is that, the commercial CZT crystals have large concentrations of defects and impurities that need to be characterized, and their effects on the detector performance should be studied.

Photoluminescence (PL) spectroscopy is a sensitive, non-contact and non-destructive method, suitable to characterize lower concentrations of point defects, such as substitutional impurities (donors, acceptors) and native defects in CZT crystals. A PL spectrum provides information regarding the defect nature of the crystal by determining the presence and the type of vacancies, interstitials, and impurities in the lattice.

The main objective of this thesis is to address the presence of the defects in CZT crystals, identify their types, and study their roles in the performance of x-ray radiation detectors using PL spectroscopy. Additionally, using PL method and different excitation sources including UV excitation, this thesis studies the surface of CZT samples and investigates the PL signature of the surface oxide of the samples, in an effort to optimize the surface processing and thereby improve CZT detector performance.

Table of Contents

List of Tables

List of Figures

Acknowledgments

I would like to express my sincere gratitude to my supervisor Dr. Tom Tiedje for giving me the opportunity to work with him on this project, and for his intellectual and financial support during the course of this work. Thank you, Tom, for the opportunities you made possible for me during my master; from giving me the opportunity to work under your supervision, to the collaborations we had. Thanks for always having faith in my work, and for always being available to discuss, and give advice for both, my research and my life. Thanks for the guidance and for sharing so much of your knowledge and experience with me. Your breadth of knowledge and passion for science are always sources of inspiration to me.

Thanks to my committee member, Dr. Fayez Gebali, for the time and effort he put in to this project! Thanks for guiding me when I first came to Canada, and for letting me know about Dr. Tiedje.

I would like to extend my sincere thanks to people at Redlen Technologies for providing me with the CZT samples, and helping me throughout this work. Special thanks to my friend and colleague Niloofar Sadeghi, the friendly and kind supervisor Dr. Georgios Prekas, Dr. Jason McKenzie, and Dr. Joseph Kumar.

I would also like to thank my laboratory colleagues Peng Wu, Mahsa Mahtab, Svetlana Kostina, and Akira Engelbrecht for their continuous help and extended discussions.

Dedication

To the Almighty God, who gave me the strength, and the ability to learn, research, and contribute to humanity.

To my parents, thank you for always being there for me. My father, my source of inspiration and support. My mother, the closest although she is miles away, my source of energy and unconditional love and care. Thank you for continuing to call to check on me and wish me well every single morning. Your little son will have a master's degree soon.

To my brother, Ahmed. My sisters, Amira, Lialy, Amany, and Faten. My nieces and nephews. My brothers and sister in law. My extended family. You all are always my source of encouragement and kindness.

To my friends, my source of support. To all the helpful and inspiring people in my life, Nabila Khayal (my elementary school teacher), Hisham Alnagar, Mohamed Alnaghy, Mohamed Abdeldayem, Mohamed Zidan, Dana Dawod, Ahmed Elmogy, Walid Gomaa, Ali Abdeldayem, Dr. Mustafa Alagamy, Dr. Ahmed Abdallah, Dr. Nageh Allam (my undergraduate research supervisor), and others.

1 Introduction

1.1 Semiconductor radiation detectors.

A variety of materials including germanium, silicon, mercuric iodide, cadmium telluride, and cadmium zinc telluride can be used to fabricate solid state radiation detectors. For a given application, the best detector depends on several parameters. Ge detectors have excellent resolution due to the large number of charge carriers per absorbed x-ray photon as a result of the narrow bandgap of less than 1 eV [1].

However, the narrow bandgap factor creates a high potential for thermally generated noise which can only be decreased by operating the detector at low temperatures. Consequently, Ge detectors need cryogenic cooling, which makes them bulky, expensive, and impractical for portable applications [2]. Additionally, silicon has a low stopping power for high-energy photons that limits its application for hard x-ray and gamma-ray detection [81-82].

In the last few years detectors fabricated from high atomic number semiconductor materials have obtained attention due to their ability to operate at room temperature and their high stopping power. Therefore, cadmium telluride, and cadmium zinc telluride detectors are commonly used [3].

For the realization of high performance, good spectral resolution, and high counting efficiency, there are certain key properties that x-ray and gamma ray detector materials should possess. Some of these requirements are as follows [4]:

- **High atomic number (Z) for efficient radiation-atomic interactions.** The photoelectric interaction is the prominent interaction in the operation of radiation

detector devices. The cross-section for photoelectric absorption in a material of atomic number Z varies as Z^n, where $4 < n < 5$.

- **Large enough bandgap for room temperature operation with low noise level.** Low leakage current is critical for low noise operation. By using larger bandgap materials with low intrinsic carrier concentrations and by controlling the extrinsic and intrinsic defects to pin the Fermi-level near midgap, the necessary high resistivity ($>10^9 \Omega$ cm) can be achieved.
- **Small enough bandgap so that the electron-hole ionization energy is small.** This ensures that the number of electron-hole pairs created is reasonably large.
- **High intrinsic $\mu\tau$ product.** The carrier drift length is given by $\mu\tau E$, where μ is the carrier mobility, τ the carrier lifetime, and E the applied electric field. Ideally, the carrier drift length would be greater than the detector thickness to ensure complete charge collection.
- **High-purity, homogeneous, defect-free materials.** Trapping of carriers due to discrete levels in the bandgap introduced by defects affects the average carrier lifetime and mobility. Homogeneity and low defect density is to ensure good charge transport properties, low leakage currents, and no conductive short circuits between the detector contacts. It is worth mentioning that, a thickness of 2 mm of CZT stops 85% of x-rays at 100 keV [85]. The absorption length of CdTe at 80 keV is 382μm.
- **Surfaces with low surface recombination and generation current.** To prevent surface recombination and surface leakage current over the lifetime of the detector, the surfaces should be stable and passivated.

1.2 Motivation for CZT research

The advantages of using CZT over other semiconductor materials are evident from Table 1, where some properties of the major semiconductors used for radiation detection are listed.

Table 1 - Properties of the major semiconductors used for radiation detection at 300K [5, 83].

Material	**Si**	**Ge**	**HgI_2**	**CdTe**	**$Cd_{0.9}Zn_{0.1}Te$**
Atomic number	14	32	80, 53	48, 52	48, 30, 52
Density (g/cm^3)	2.33	5.33	6.4	6.2	5.78
Bandgap (eV)	1.12	0.67	2.13	1.44	1.57
Pair creation energy (eV)	3.62	2.96	4.2	4.43	4.6
Electron mobility (cm^2/Vs)	1350	3900	100	1000-1100	1100
Hole mobility (cm^2/Vs)	480	1800	4	80	50
Electron $\mu\tau$ product (cm^2/V)	2.7×10^{-2}	0.72	10^{-4}	10^{-3}	10^{-3} - 10^{-2}
Hole $\mu\tau$ product (cm^2/V)	9.6×10^{-3}	0.84	10^{-5}	5×10^{-5}	3×10^{-5}

Considering the requirements listed above and the properties illustrated in Table 1, CZT has come to the forefront among other semiconductor materials for x-ray and gamma-ray detection. Substituting 10% of Cd atoms with Zn atoms increases the bandgap to about 1.57 eV. The increased bandgap gives an immediate solution to the problem of noise due to leakage current, and the bulk resistivity also becomes higher. The addition of Zn, which has a lower vapor pressure than Cd, into the melt of Cd and Te during crystal growth helps

to reduce the dislocation density [6]. Additionally, CZT has much higher atomic number than Si, which increases the effective interaction cross section between the atoms and incident photons, and results in a higher efficiency of electron-hole pair generation over the incident photons. Also, the higher operating temperature of CZT in comparison to Ge is an important advantage. The relatively high electron mobility of CZT (1100 cm^2/Vs) is another advantage, as it results in a high charge collection efficiency of the electrons in the conduction band [7].

1.3 Current challenges of CZT for commercial x-ray detector

A pure defect-free material is desirable for fabricating high resolution CZT radiation detectors that function at room temperature. The corresponding crystal growth and fabrication processes are challenges. The material is usually grown using the Vertical-Bridgman-Method (VGF) or the Travelling-Heater-Method (THM) [8]. Typically, various defects and impurities are introduced in the material during growth, post growth annealing, and during fabrication processes. These defects and impurities introduce shallow and deep levels and thereby hinder the higher resistivity and lower dark current desired. A defect or impurity causing a deep level in the middle of the bandgap can also be induced. The mostly used n-type dopants for the compensation process are chlorine or indium [9]. Some of the point defects act as trapping centers for free carriers and distort the drift and collection of the carriers, and the space charge can result in severe field distortions, and degradation in detector performance. As these point defects typically have a feature size of a single or multiple atoms, they cannot be inspected visually.

Low temperature measurements are useful in semiconductor defect investigations. At low temperature, the thermal excitations are diminished in a lattice, and the non-radiative recombination processes are reduced. The carriers concentrated at the band edges and in the defect states can participate further in optical and electrical transitions, and thus we can get important information about their density and energy in the semiconductor. Peak intensities, and energy positions in the low-temperature PL spectra of CZT give a great deal of information concerning the defects and impurities near the surface and inside the bulk of the material [10].

One of the typical problems associated with detector fabrication is surface recombination, which greatly influences detector performance by the dark current which is a source of noise in the detector. To reduce the surface leakage current and consequently improve energy resolution of CZT detectors, much work has been done using chemical etching. These efforts were aimed at restoring surface stoichiometry and removing damaged surface layers resulted from mechanical polishing. However, detector performance is still limited by the surface component of the dark current. Recent studies have indicated that this current can be further decreased by intentional surface oxidation [11].

1.4 The goal of this thesis

In this work, we use PL spectroscopy to examine the quality of different CZT crystals, and study the defects and impurities and their signatures in the PL emission spectra. We also investigate the correlations between these defects and compare the spectra of different CZT samples, in order to determine the impact of these defects on the yield of the CZT detectors.

Additionally, we use the PL technique and different excitation sources with different photon energies including UV excitation, to investigate the initial bromine-in-methanol (Br-MeOH) etching treatment. We also examine the surface oxide layer formed through the use of different surface passivation treatments, attempting to optimize the surface processing and thereby enhance detector performance.

We believe that the work in our thesis can be considered as feedback to the CZT crystal growth and detector fabrication industry in order to improve the quality of the material and the performance of the detector.

1.5 Thesis outline

This thesis structure is as follows:

Chapter 2 is an overview of CZT Properties, CZT crystal growth, CZT detector fabrication, the operational characteristics of the detector, radiation interactions with the detector, CZT device operation, and the theory behind photoluminescence

Chapter 3 introduces photoluminescence spectroscopy as the experimental method employed in this project, and provides information about the CZT samples used in this study.

Chapter 4 Presents the results of all the experiments performed throughout the project, followed by discussions and comparisons that investigate the presence and the origin of the defects near the surface and in the bulk of the CZT samples that were studied.

Chapter 5 provides a summary of the work in this thesis, and suggests further investigations for the future.

During this work, a collaboration was developed with Redlen Technologies Inc. as the industrial partner of the project. Different CZT samples with nominal zinc molar concentration of 10% have been provided by Redlen.

2 Background

This chapter provides an overview of CZT Properties, CZT crystal growth, CZT detector fabrication, the operational characteristics of the detector, radiation interactions with the detector, CZT device operation, and the theory behind photoluminescence.

2.1 CZT Properties

2.1.1 Crystal Structure

The $Cd_{1-x}Zn_xTe$ alloy is a CdTe crystal, in which a fraction x of the Cd atoms are randomly substituted with Zn atoms. CdZnTe crystals have a zinc blende structure with two interpenetrating face centre cubic (FCC) sub-lattices, one for the Te atoms and the other for Cd (or Zn), which are separated by one-quarter of a unit-cell body diagonal. The CdZnTe atoms exhibit covalent bonding, hence valence band electrons are shared. Figure 1 shows a schematic diagram of the zinc blende crystal structure of CdZnTe [13].

The crystals used for our studies are cut perpendicular to the <111> orientation defined by the Miller indices on the plane. This arrangement leaves one surface of the crystal (top) occupied by the anion atoms and the other (bottom) occupied by the cation atoms [12].

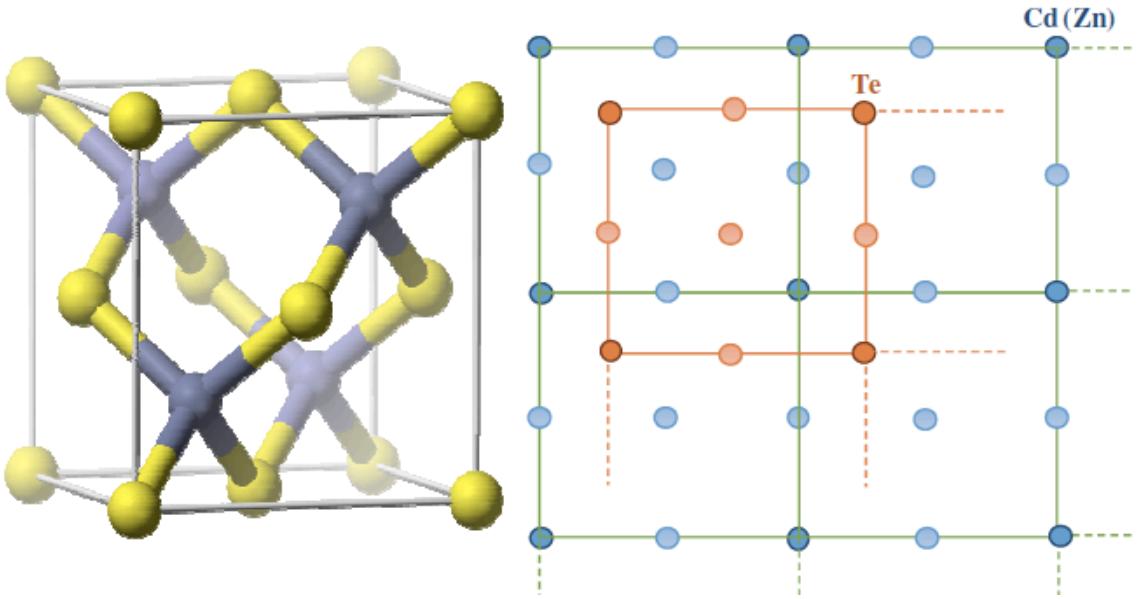

Figure 1 - Schematic diagram of the zinc blende crystal structure of CdZnTe; a) 3D model and b) 2D projection along (100) [13].

2.1.2 Resistivity

For good performance of the detector, high resistivity and long lifetime of charge carriers are desired attributes of the material. The increase in the resistivity translates to a decrease in leakage current. Alloying CdTe with Zn increases the bandgap and thereby increases the intrinsic resistivity of CZT. The bandgap of CZT depends on the Zn fraction x and at room temperature the bandgap varies between 1.5 eV (CdTe) and 2.2 eV (ZnTe). It has been previously observed that an increase in zinc fraction x from 0 to 0.2 results in an increase in the resistivity from 3 x 10^9 to 2.5 x 10^{11} Ω cm [14]. Moreover, material resistivity can be typically controlled in CZT by a compensation mechanism involving both deep and shallow level defects in the material [13-14]. Compensation is the process of adding donors to p-type material or acceptors to n-type material to reduce the carrier density.

2.1.3 Charge Transport Properties

Ideally the charge carrier mean free path should be larger than the detector thickness. This allows all photo-generated carriers to be collected at the electrodes and avoids incomplete charge collection. Carrier mean free path is the product of mobility, lifetime, and electric field. Mobility-lifetime product is a fundamental attribute of the detector's performance. It is worth mentioning that, impurity levels can affect the values of charge mobility. The carrier lifetime can be improved by enhancing the purity and crystallinity of the CZT material. The reported values of mobility-lifetime products vary between 2×10^{-2} - 5×10^{-3} cm^2/V for electrons and 3×10^{-5} - 8×10^{-4} cm^2/V for holes [81]. Holes have low charge collection efficiency which results in incomplete hole collection, widening of photopeak, and low energy resolution. Co-planar grid is one of the CZT detector designs that were reported to eliminate the effect of holes in signal formation [15].

Deep impurities present energy levels near the middle of the bandgap. They can behave as traps for charge carriers by restraining a hole or electron. Also, they can act as recombination centers by alternately capturing electrons and holes. Trapping and recombination result in a loss of charge carriers and a decrease of the average lifetime of carriers. Structural defects such as anti-sites, interstitials, and dislocations can also cause trapping and charge carrier loss [16].

Microstructural defects, such as precipitates, inclusions, bubbles, and pipes may provide pathways for electrical conductivity, increase leakage current, reduce carrier lifetime, and thus, deteriorate the detector electrical transport properties [17].

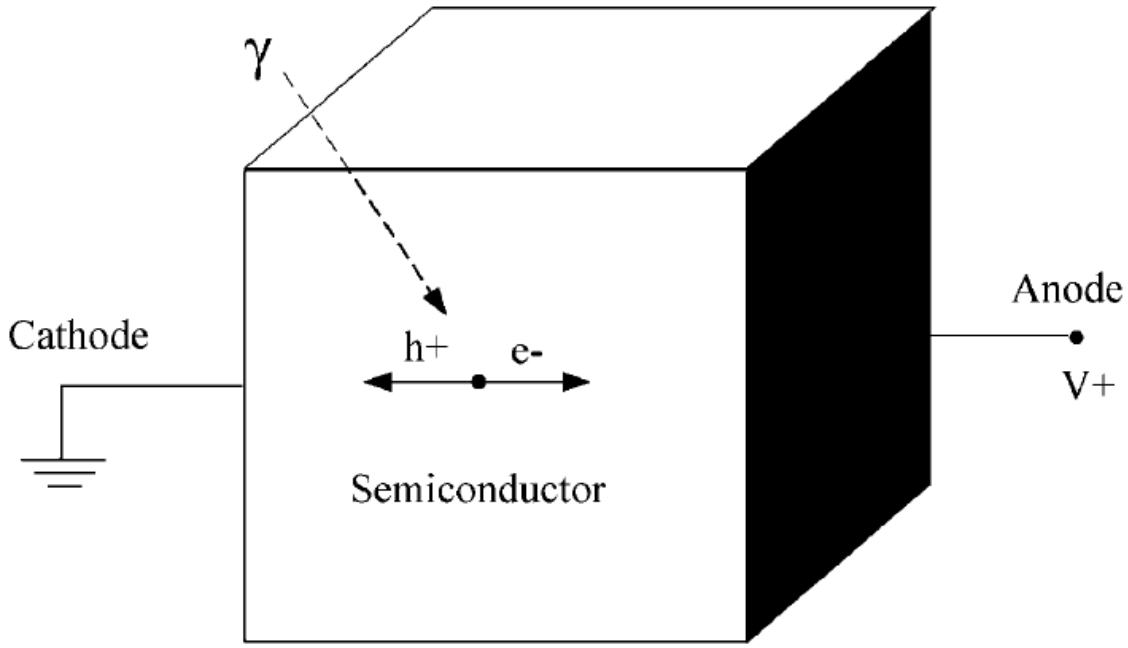

Figure 2 - Created carriers under the influence of an electric field [18].

2.2 CZT crystal growth

Commercializing large volume CZT radiation detectors is still facing some challenges regarding the defects and crystal quality. Most of the defects affecting CZT detectors are introduced during the crystal growth process. Thus, the crystal growth of CZT is still under ongoing research efforts to obtain large volume, defect and crack free, homogeneous, and stoichiometric with high resistivity ingots. Crystal growth techniques include the Bridgman method, the high-pressure Bridgman, the low-pressure Bridgman, the physical vapor transport method, and the travelling heater method (THM) [19]. The samples studied in this project are grown by the travelling heater method, which is the method currently used in Redlen Technologies.

The travelling heater method (THM) is a seeded growth technique that functions by precipitation of solid material from a melt. A CZT seed crystal is placed in the bottom of a quartz ampoule, then Te-rich CZT alloy is added as solvent while the polycrystalline CZT is added on top as feed material. The heater is adjusted in front of the ampoule such that it first melts the Te-rich CZT compound and moves up to melt the polycrystalline CZT. The polycrystalline CZT dissolves into molten tellurium. As the travelling heater is moved, CZT crystal precipitates from the tellurium solvent and grows on the CZT seed to form homogenous single grains of CZT crystal [20].

2.3 CZT detector fabrication

After growing the crystals then slicing, polishing, and etching the device wafers, CZT radiation detector devices are fabricated by applying metallic contacts on the surfaces, then bonding the device to the external circuitry and final packaging. The contacts function as the electrodes that collect charges under an internal electric field from the applied bias [22]. As shown schematically in Figure 3, the three generic device configurations for room temperature semiconductor radiation detectors are simple planar, co-planar grid and pixelated array [22]. Each of these configurations may be used for purposes where certain performance factors are to be optimized. Simple planar and co-planar grid configurations are employed for large-volume single element detectors. Regarding the coupled electronics, planar devices are simpler, but co-planar configurations can operate as electron-only devices to offer better spectral resolution. Pixelated detectors are preferred in imaging systems where position information is obtained from individual pixels. Photolithography is employed to design the geometry of the electrodes [21].

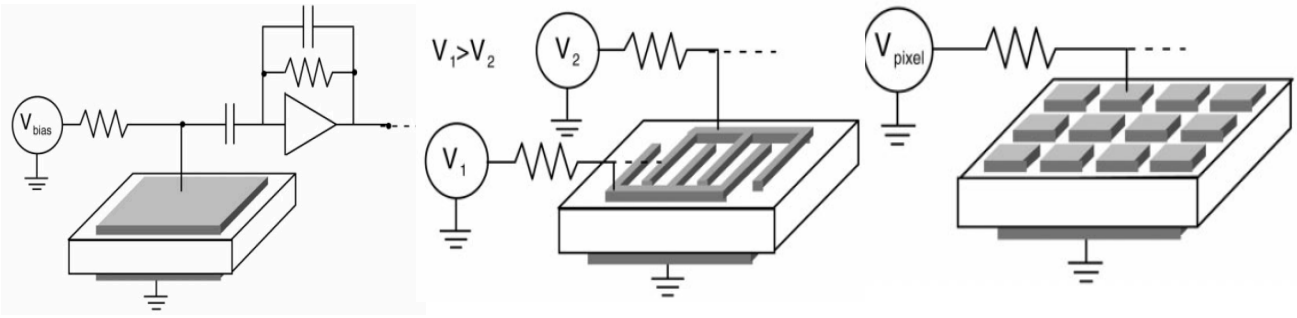

Figure 3 - Schematic diagram of three basic radiation detector geometries: (a) planar detector; (b) co-planar grid detector; (c) pixelated detector.

2.4 Operational characteristics of semiconductors

2.4.1 Band structure

The periodicity of the lattice in crystalline materials forms electron energy bands. In crystalline solids, electrons are restricted to energy bands. There are two important bands. The valence band is the lower band which is filled with electrons. Electrons in the valence band are bound to certain lattice sites within the crystal. Next higher band is the conduction band which is normally empty. Electrons excited into the conduction bands determine the electrical conductivity of the material, as they are free to move through the crystal. The two bands are separated by an area of prohibited energies known as the bandgap [23].

Without thermal excitation, insulators and semiconductors have entirely full valence band and completely empty conduction band, and there is no conductivity. For electrons in the valence band to reach the conduction band, they must first cross the bandgap. At higher temperatures where there is sufficient thermal energy, a number of electrons can make this transition leaving behind a number of vacancies known as holes. On the other hand, the highest occupied energy band in metals is not filled, so electrons can move throughout the

material even at zero temperature, as slight incremental energy is required for the electron to migrate above occupied states [24].

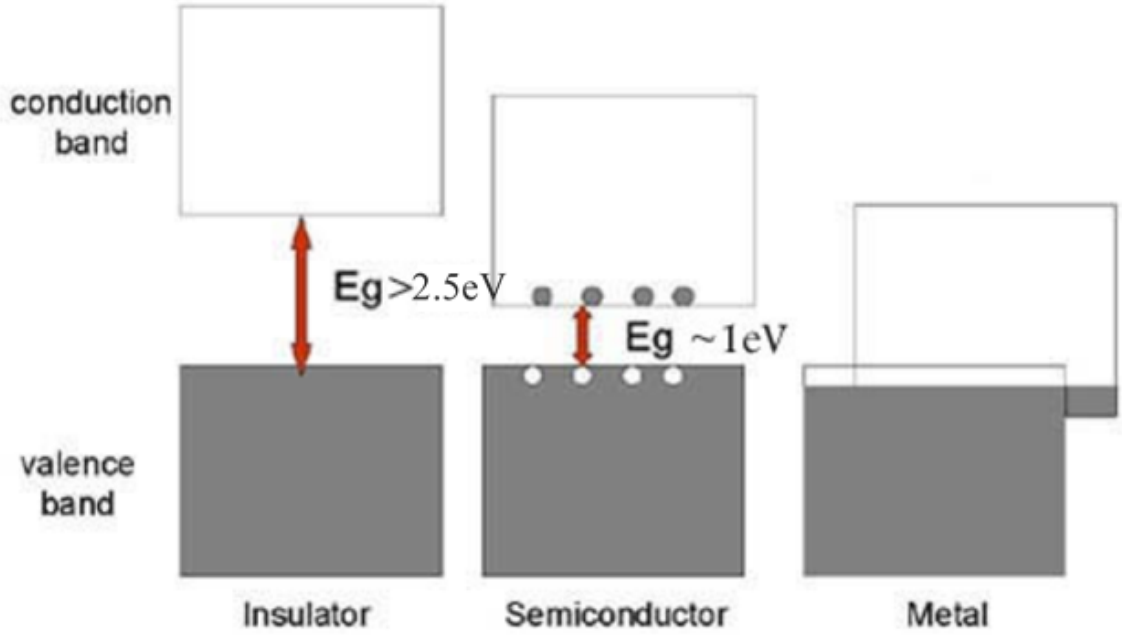

Figure 4 - Band structure for electron energies in materials [81].

CdTe is a II-VI compound semiconductor with a bandgap energy of 1.5eV at room temperature. If a certain fraction x of Cd atoms is replaced by Zn, then the bandgap will be raised, see Figure 5 [27]. Thus, $Cd_{1-x}Zn_xTe$ has the advantage of non-fixed and wider bandgap energy. $Cd_{1-x}Zn_xTe$ bandgap ranges from 1.5eV to 2.2eV [28]. $Cd_{0.9}Zn_{0.1}Te$ has a bandgap of 1.57 eV [5, 83]. Additionally, CdZnTe is a direct bandgap semiconductor material. Thus, there is no momentum change following the transition from one band to the other [25]. Figure 6 schematically shows the inter-band transition for a direct band-gap semiconductor [26].

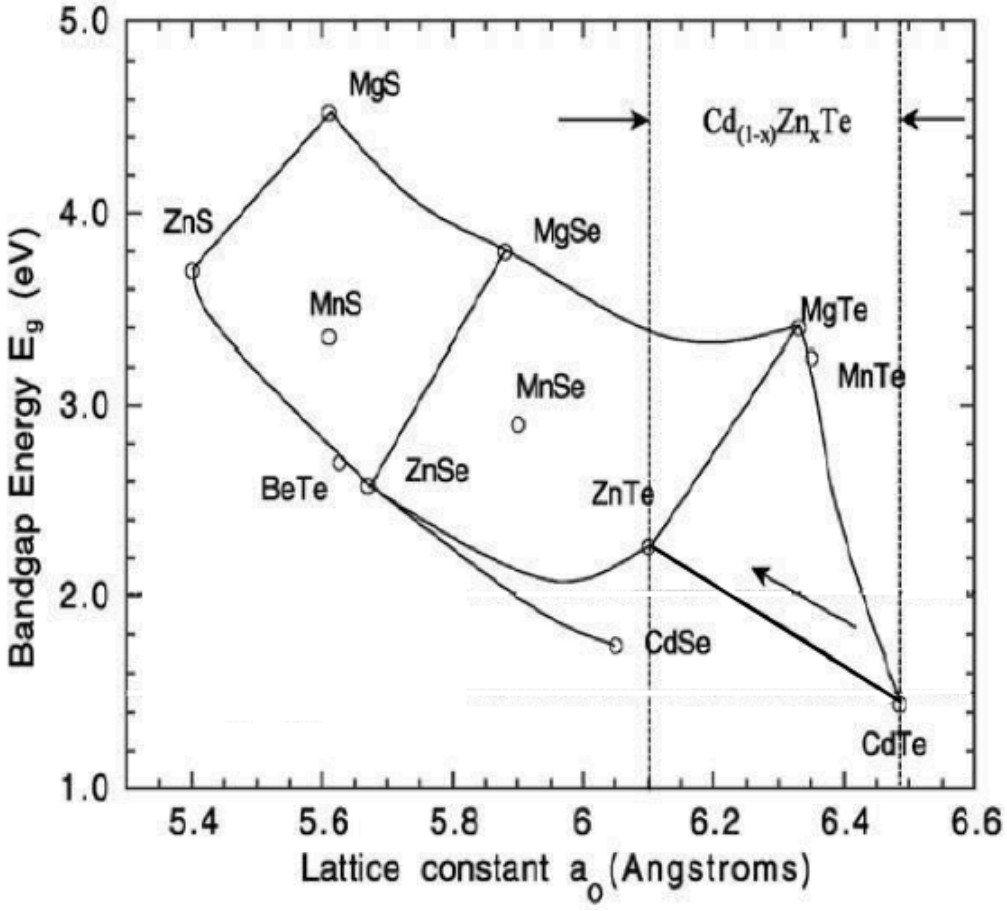

Figure 5 - The bandgap energy of II-VI compounds as a function of lattice constant [27].

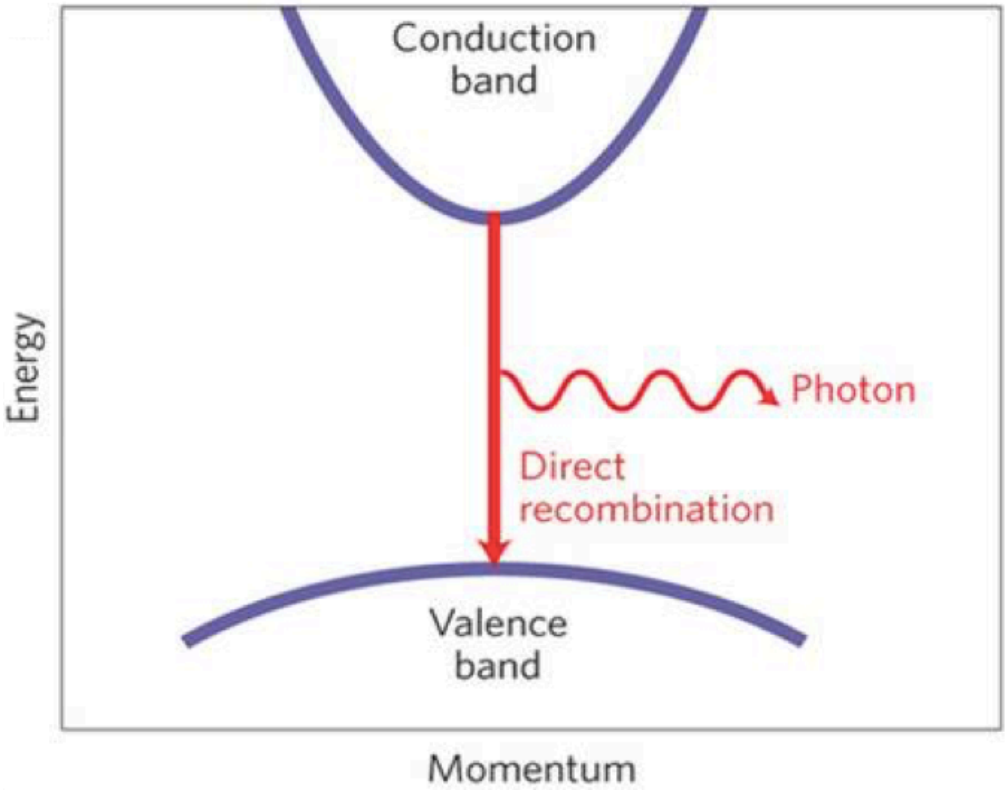

Figure 6 - A schematic diagram showing the inter-band optical transition for a direct bandgap semiconductor [26].

2.4.2 Charge carriers

At non-zero temperature, valence electrons can get enough thermal energy to move across the band gap to the conduction band leaving behind a hole. Electrons and holes are the charge carriers and their mobility contributes to the conductivity of a material.

The density of thermally generated electrons and holes is given by

$$n(T) = AT^{\frac{3}{4}} \exp\left(-\frac{E_g}{2kT}\right) \tag{2.1}$$

where T is the absolute temperature, E_g is the bandgap energy, k is the Boltzmann constant, and A is a proportionality constant characteristic of the material. The larger the E_g the lower the n(T).

Electrons and holes experience a net migration caused by an applied electric field. Electrons drift in the opposite direction of the electric field, whereas holes move in the same direction as the electric field [29].

2.4.3 Impurities and dopants

For intrinsic semiconductors, the numbers of electrons in the conduction band and holes in the valence band are the same. On the other hand, extrinsic semiconductors have impurities or dopants. Extrinsic semiconductors are either n-type or p-type semiconductors.

In n-type semiconductors, impurities are donors, as they donate electrons to conduction band. The extra electrons may have energies near the top of the gap, and thus can occupy a position within the prohibited gap. With the extra electrons added, the equilibrium between electrons and holes shifts. Oppositely, p-type semiconductors form an unsaturated covalent bond acting as a hole in the lattice. The acceptor sites lie near the bottom of energy band. Both donors and acceptors are shallow impurities [30].

2.4.4 Trapping and recombination

Deep impurities create energy levels near the middle of the band gap. They behave as traps for charge carriers by immobilizing a hole or electron. Also, they can act as centers of recombination by trapping electrons and holes sequentially. Both trapping and recombination result in losses of charge carriers, and hence reduce the efficiency of carrier collection in the detector. Additionally, point defects within the crystal lattice can cause trapping and loss of charge carriers [31].

2.4.5 Leakage current

Leakage current comes from recombination currents in the bulk and surface of the detector. Minority carriers transferred throughout the junction, and the thermally generated electron-hole pairs within the depletion region can generate leakage currents in the detector. The rate of thermal generation of electron hole pairs within the depletion region can be decreased by cooling. The higher the semiconductor bandgap, the lower the rate of thermal generation of electron-hole pairs. Additionally, surface recombination centres can create leakage paths. Surface passivation has been reported to reduce surface leakage current [32].

2.4.6 Reverse biasing

An unbiased p-n junction has a narrow depletion region. Thus, an external voltage is applied in a reverse biased direction. When a reverse bias is applied to the junction, the thickness of the depletion region increases, which enlarges the volume for collecting charge carriers produced from radiation. Applying the largest possible voltage leads to a better energy resolution. However, maximum operating voltage must be maintained less than the breakdown voltage to prevent destruction of the detector. Reverse biased p-n junction collects the charge carriers created within the depletion region faster and more efficiently [33].

2.5 Radiation interaction with detector

Radiation is the release of energy either in the form of waves or sub-atomic particles. Radiation can be classified as charged or uncharged. Charged radiation includes beta particles (electrons and positrons), protons, and alpha particles. Uncharged radiation

includes gamma rays, x-rays and neutrons. Most of the radiation types are directly ionizing, as after collision with matter it ionizes a number of atoms. Gamma rays are produced by radioactive decay of an excited nucleus. X-rays are produced when an electron in a higher energy orbital falls to a lower energy orbital during the relaxation of an excited atom. X-rays have energies between 1 KeV – 100 KeV. Gamma ray energies are above 100 KeV [34].

For radiation to be detected, it must first undergo interaction with the medium. Gamma rays and x-rays interact with matter by photoelectric absorption, Compton scattering, and pair production. The main concept revolves around the ejection of an orbital electron by an incident photon through an ionization process. The ejected electron then moves typically in a different direction from the incident photon, producing more ion pairs, in secondary ion processes [35].

2.5.1 Photoelectric absorption

The photoelectric effect is typically an ideal process for a radiation detector as all of the energy of the incident photon is absorbed by a tightly bound inner electron usually in the K-shell. This photoelectron has a kinetic energy equal to the incident photon energy minus the atomic binding energy of the electron. The photoelectron then loses its kinetic energy by Coulomb interactions with the semiconductor lattice creating many electron-hole pairs. The number of electron-hole pairs created depends on the energy of the incident photon. Besides, some x-ray photons may be generated and reabsorbed by photoelectric absorption with less tightly-bound shell. Equation 2.2 gives an approximation of the probability, τ, of the photoelectron absorption to occur,

$$\tau \sim \frac{Z^n}{E_\gamma^{3.5}} \quad (2.2)$$

where the exponent n varies between 4 and 5 over the energy region of interest, Z is the atomic number of the material, and E_γ is the gamma ray energy. It is clearly obvious that the photoelectric absorption is enhanced for materials with high atomic number and for relatively low photon energies. Accordingly, photoelectric absorption is the predominant mode of interaction at low photon energies (10eV-100KeV) [36].

2.5.2 Compton scattering

In Compton scattering, an incoming photon collides with a loosely bound outermost orbital electron. The direction and energy of the incident photon is altered. The incident photon transfers some of its energy to the orbital electron. The emitted electron then loses its energy through creation of electron-hole pairs. The photon of reduced energy is scattered from its original direction after this collision and may further involve photoelectric absorption or Compton scattering. Energy transfers are determined from the conservation of energy and momentum during the collision [37-38].

The interaction probability of x- and gamma rays depends on the atomic number Z of the material. For Compton scattering, it is directly proportional to Z, for pair production it is Z^2, and for photoelectric effect, it is related to Z^n ($4 < n < 5$). This shows that heavier elements are more capable of detecting X- and gamma rays than lighter elements [39].

2.6 CZT device operation

In a CZT detector, the radiation is incident on the CZT crystal, which forms a sandwich between two metal electrodes. The radiation energy is transferred to an orbiting electron in the form of kinetic energy, which is then responsible for creating more electron-hole pairs

in the crystal. When a reverse bias is applied to the detector, a depletion region is created which enables moving of electrons and holes to the respective electrodes due to the applied electric field. The electrodes are connected to the external circuitry that amplifies and shapes the pulse current which can be seen on a display screen or oscilloscope. The magnitude of the pulse is proportional to the energy lost by the incident ionizing radiation. A schematic diagram of the detector is shown in Figure 7 [13]. The time taken to collect the charges reflects the mobility and average distance traveled by charge carriers to reach the collection electrodes [40].

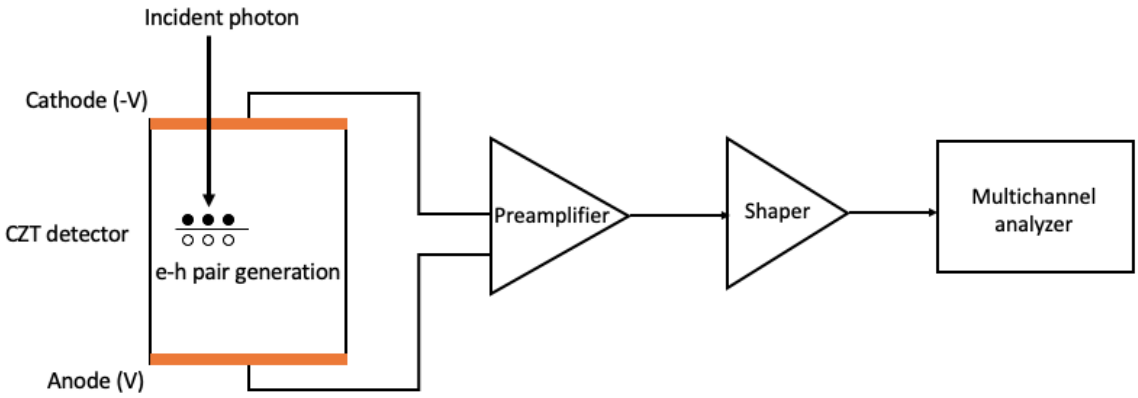

Figure **7** - Schematics of the operation of CZT radiation detector.

2.7 Photoluminescence

When the material is irradiated with photons which have higher energy than the band gap of the semiconductor, the incident photon beam is partially reflected, absorbed, and transmitted by the material. Absorption of these photons results in excitation of electrons from the valence band to the conduction band creating an electron-hole pair. Further, electrons can lose a portion of their energy and move down from the conduction band to energy levels within the gap, through a non-radiative transition. Luminescence occurs

when the excited electrons and holes in the semiconductor recombine and emit photons with energy equal to or lower than the band gap. The resulting emission spectrum is the PL emission spectrum. The variety of emitted photon energies reflects the existence of various energy states within the bandgap of the semiconductor. Different energy states are formed by different defects and impurities in the lattice. Thus, the PL emission spectra offer information about the nature and density of defects and impurities in the lattice.

It is rare to observe direct conduction band to valence band recombination in PL spectra. Even if the recombination occurs, the crystal can reabsorb the emitted photons. Consequently, the observed recombinations in PL spectra are predominantly those with emission energies less than the bandgap, which include excitonic recombinations and recombinations involving the carriers trapped by impurities [41].

2.7.1 Low Temperature PL

Low temperature PL is significantly useful for semiconductor defect investigations. At low temperature, the thermal excitations are reduced, and the non-radiative recombination processes decrease. The carriers are trapped at localized states, and the defect states can contribute further in optical and electrical transitions, and thus we can obtain important information about their density and energy in the semiconductor. Also, as a semiconductor is cooled, the bandgap shifts to a higher energy. The shift in the bandgap results from a combination of a temperature-dependent contraction of the lattice and a temperature dependent electron-lattice interaction. As the sample temperature increases, excitons dissociate, radiative recombination of carriers reduce, and rates of competing non-radiative recombination processes increase [42].

2.7.2 Energetic levels inside the bandgap

Energy bands result from a periodic potential of atoms in a crystal lattice. In reality, there are structural imperfections in the crystalline materials, formed during the growth process. Foreign atoms of different elements can also be inserted into the structure, which can act as impurity centers and disrupting the periodicity of the crystal. To illustrate the influence of impurities in a semiconductor lattice, Figure 8 shows the silicon lattice disrupted by phosphorous atom (donor) and boron atom (acceptor) impurities [44]. After forming covalent bonds with neighboring atoms, the phosphorus atom still has one remaining electron and thus it is considered as a donor. The electron can then be excited, and the excitation energy required depends on the nature of the impurity atom. The energy of the donor electron is lower than the conduction band and represents a new allowed energy state in the bandgap.

On the other hand, the boron atom has less valence electrons than silicon atoms, so it takes an extra electron to form the covalent lattice bond. As a result, a vacancy is created and the defect is named acceptor. A deep level could be formed for example by a Au impurity on a silicon site. The non-bonding d-orbitals from Au create bound states near the centre of the band gap. The deep levels have a larger influence on electron–hole recombination than shallow levels, and thus they affect the detector yield and performance [43].

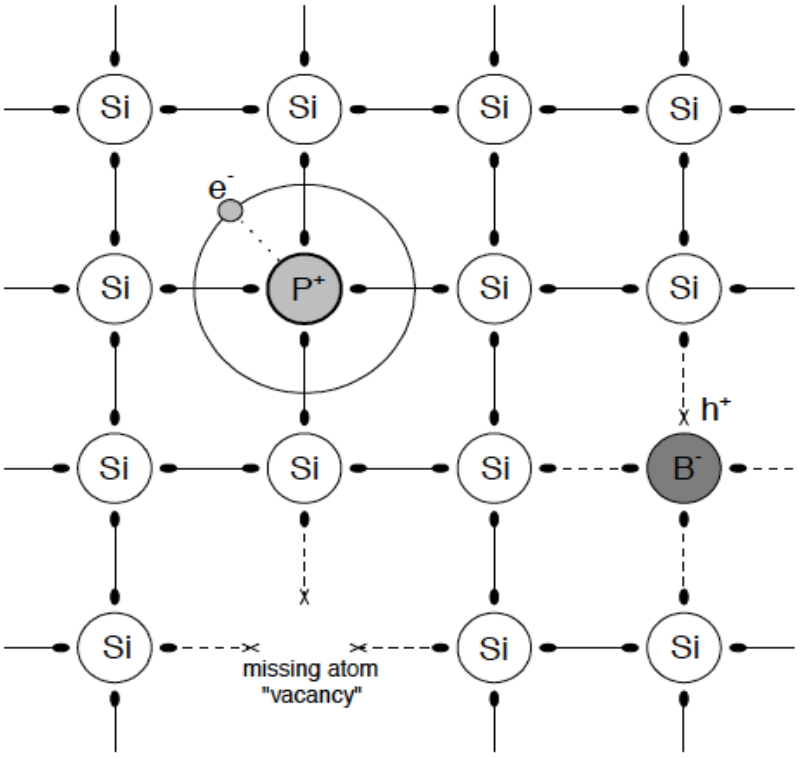

Figure 8 - Phosphorous and boron impurities in a silicon crystal.

Several research studies have been conducted to investigate the deep levels in CdZnTe and match them to certain defects or impurities in the crystal lattice of the material, aiming at adjusting the growth process and enhancing the detector performance. Various deep levels exist inside the bandgap of CdZnTe, and the levels with a higher trapping cross-section have larger effects on the detectors. A PL broad band in the spectral region around 1.1 eV is observed and investigated in chapter 4 of this thesis. The 1.1 eV PL peak results from recombination in deep donor–deep acceptor pairs [45-46].

2.7.3 Electronic point defects

Since CZT is a II-VI compound, all groups I, III, IV, V, and VII elements can in principle act as dopants. Further, transition metal elements tend to give deep levels. The ionization energies of groups I, III, IV, V, and VII elements are listed in Table 2. Substitutional group

V elements on anion (Te) sites act as acceptors. Additionally, group III elements on the cation (Cd) sites and VII elements on the anion (Te) sites are donor states. Further, Group I elements act as acceptors on cation (Cd) substitutional sites, on the other hand, they act as donors on interstitial sites; Li is an acceptor at Zn or Cd sites with a ground state energy of 58 meV but it is a donor at interstitial sites with a ground state energy of 14 meV.

Table 2 - Ionization energies of groups I, III, IV, V, and VII elements in CZT [22].

Element	Photoionization, E (meV)	Thermal ionization, E (meV)	Method
Li	Acceptor: 58.0		PL
Na	Acceptor: 58.7		PL
N	Acceptor: 56.0		PL
P	Acceptor: 68.2		PL
As	Acceptor: 92.0		PL
Cl	Donor: 14		
Cl	Donor: 14.48		PL
Cl–V_{Cd}	Acceptor: 120		PL, ODMR
Cl DX1		Donor: 220	Theory
Cl DX2		Donor: 470	Theory
Cl DX3		Donor: 210	Theory
Al	Donor: 14.05		PL
F	Donor: 13.71		PL
Ga	Donor: 13.83		PL
In	Donor: 14.08		PL
In DX		Donor: 300	Theory for $Cd_{0.8}Zn_{0.2}Te$
Ge	Donor: 950	Acceptor: 730	Photo-EPR
Sn	Donor: 850		Photo-EPR
Sn	Donor: 900		DLTS
Sn	Donor: 890, 430		QTS
Pb	Donor: 1280		Photo-EPR

2.7.4 Native defects:

Native defects are the defects caused by local elements, whereas, non-native defects are the defects caused by impurities. A native defect can be a vacancy, an interstitial, or an anti-site. The native defects in CZT can be donors or acceptors. Their ionization energies are listed in Table 3. Both Cd and Te vacancies are identified in CdZnTe. The V_{Cd}^{2-} position

is less than 0.47 eV above the valence band. Under Te rich conditions, CdZnTe at high temperatures is p-type with V_{Cd} as the dominant acceptor and Te_{Cd} as the compensating donor.

Table 3 - Ionization energies of native defects [22].

Defect	Thermal ionization, E (eV)	Photoionization, E (eV)	Method
V_{Cd}	Acceptor: <0.47		Photo-EPR
V_{Cd}		Acceptor: 0.78	PICTS
V_{Cd}	Acceptor: 0.2, 0.8		Theory
V_{Cd}	Acceptor: 0.1, 0.4, 0.76		DLTS, PICT
V_{Cd}	Acceptor: 0.1		Theory
V_{Cd}	Acceptor: 0.43		TEES
V_{Cd}	Acceptor: 0.21; Donor: 0.73		TEES
Te_{Cd}	Donor: 0, 0.4		Theory
Te_I	Donor		Theory
Te_{Cd}–V_{Cd}	Neutral		Theory
V_{Te}		Donor: 1.4	Photo-EPR
V_{Te}	Donor: 1.1		DLTS, PICT
V_{Te}	Donor: 0.4, 0.5		Theory
Cd_I	Donor: 0.64		DLTS, PICT
Cd_I	Donor: 0.54		PICT
Cd_I	Donor: 0.5		Theory
Cd_I	Donor: 0, 0.2		Theory

2.7.5 Free excitons

A free hole in the valence band and a free electron in the conduction band experience a Coulomb force as a pair of opposite charges and create a composite particle known as an exciton. The electron and the hole are feebly bound to each other by their attractive electrostatic interaction. If the exciton is not bound to a defect or impurity, it is named as a free exciton. The energy of the free exciton can be described by the hydrogen model as:

$$E_x = E_g - \frac{2\pi^2 m_r^* q^4}{h^2 \varepsilon^2} \tag{2.3}$$

where E_g is the band gap energy, h is the Plank's constant, ε is the dielectric constant, and m_r^* is the reduced effective mass of the electron-hole pair. The reduced effective mass is defined as:

$$\frac{1}{m_r^*} = \frac{1}{m_e^*} + \frac{1}{m_h^*} \tag{2.4}$$

where m_e^* is the electron effective mass and m_h^* is the hole effective mass.

In $Cd_{1-x}Zn_xTe$, the bandgap and free exciton binding energies are variable with the zinc concentration x. Thus, the binding energy of the free exciton ranges from about 10 meV for CdTe to 13 meV for ZnTe [47].

2.7.6 Bound Excitons

In reality, semiconductor materials contain impurities and defects. A defect may increase the binding energy of the exciton. If the total energy of the exciton reduces, then the exciton is bound to the defect, and it is called a bound exciton. Bound excitons are normally observed in PL emission spectra at energies slightly lower than the bandgap, and investigating them offers significant information about the impurities and defects inside the semiconductor. Donors and acceptors can trap excitons and produce bound excitons. (D, X) is an exciton bound to a donor, and (A, X) is an exciton bound to an acceptor [48].

2.7.7 Band to Impurity/Defect Level Recombinations

Recombination that involves electron transitions from donor levels to valence band is denoted as (D, h). Further, if the electron transitions are from the conduction band to acceptor levels then they are expressed as (e, A). Donor to valence band recombination can be described by:

$$E_{PL} = E_g - E_D \quad (2.5)$$

where E_{PL} is the PL peak energy of (D, h) emission, E_g is the bandgap energy, and E_D is the ionization energy of the donor impurity. Additionally, the ionization energy of the acceptors of (e, A) peak can be determined according to:

$$E_{PL} = E_g - E_A \quad (2.6)$$

where E_{PL} is the PL peak energy of (e, A) emission, E_g is the band gap energy, E_A is the ionization energy of the acceptor [42].

2.7.8 Shallow Donor-Acceptor Pair Recombination

In CZT, a recombination may occur between shallow donor and shallow acceptor levels, and a peak denoted as DAP can be observed in CZT PL spectra which can be described as follows:

$$E_{PL} = E_g - (E_A + E_D) + e^2/\varepsilon R \quad (2.7)$$

where E_{PL} is the PL peak energy of the DAP emission, E_g is the energy of the bandgap, E_A is the acceptor ionization energy, E_D is the donor ionization energy, e is the electron charge, ε is the dielectric constant, and R is the distance between donor and acceptor atoms [47].

2.7.9 Phonon Replicas

Phonons are vibrational modes of the atoms in the crystal. Beside the recombinations occurring between electrons and holes, electron-phonon interactions may happen and result in emission of one or more phonon replicas of the main recombination peak, these phonon replicas appear in the PL emission spectra. Strong coupling between the localized carriers

and the lattice can lead to the observation of multiple orders of phonon replicas. Optical phonons have two types of modes; longitudinal modes (LO) and transverse modes (TO). In CZT, electron-phonon interactions are dominated by the longitudinal optical mode (LO) [49]. The phonon replica of DAP is often observed in our work and centered at 1.58 eV. The LO phonon energy is roughly 21 meV in CZT [42].

2.7.10 Self-compensation effects and A-centers

CZT PL spectra typically consist of three regions; near band edge region, donor acceptor region, and defect related region. The near band edge region contains exciton peaks. The donor acceptor region has a shallow donor acceptor peak (DAP) and its LO phonon replicas. Further, the defect related region contains a wide peak called $D_{complex}$, and the deep level 1.1ev peak. $D_{complex}$ peak is attributed to A-center complex defects and dislocations. A-center is a complex of a Cd vacancy and a donor $[In_{Cd}^{+} - V_{Cd}^{2-}]^{-}$.

Compensation effect is the process of forming neutral complexes. Cd vacancies exist in CZT crystals due to the high partial pressure of Cd in the growth process. Cd vacancies $[V_{Cd}^{2-}]$ act as shallow acceptors in CZT. A compensation between the intrinsic deep donor Te antisites $[Te_{Cd}^{4+}]$ and the shallow acceptor Cd vacancies $[V_{Cd}]^{2-}$ may occur and produce the neutral defect complex $[Te_{Cd}^{4+} - 2V_{Cd}^{2-}]^{0}$ as illustrated by equation 2.8 and figure 9 [50]. In figure 9, Cd vacancies and Te antisite defects drawn with red color form the neutral defect complex $[Te_{Cd}^{4+} - 2V_{Cd}^{2-}]^{0}$:

$$[Te_{Cd}]^{4+} + 2[V_{Cd}]^{2-} \leftrightarrows [Te_{Cd}^{4+} - 2V_{Cd}^{2-}]^{0} \quad (2.8)$$

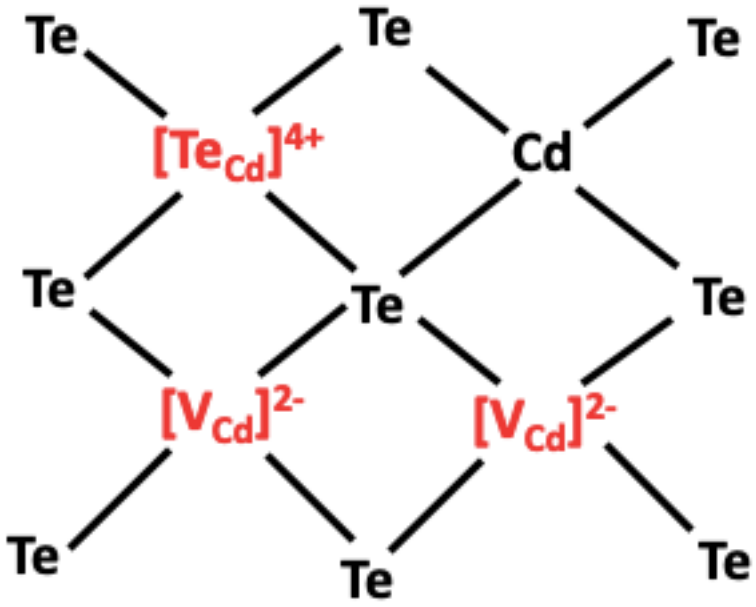

Figure 9 - A model of the neutral defect complex [Te_{Cd}^{4+} - $2V_{Cd}^{2-}$]^0.

Additionally, a group-III donor impurity, typically indium (In), is usually introduced to the CZT crystals during the crystal growth process. The doped indium atoms act as hydrogenic shallow donors [In_{Cd}]$^+$ by substituting for Cd. In donors with surrounding Cd vacancies create the singly negative donor-vacancy complex (A center) [In_{Cd}^{+} - V_{Cd}^{2-}]$^-$.

According to compensation effects, the A-centers complex and an extra indium donor may further form a neutral defect complex [In_{Cd}^{+} - [In_{Cd}^{+} - V_{Cd}^{2-}]$^-$]^0 as illustrated by equation 2.9 and figure 10 [50]. In figure 10, indium donors and cadmium vacancy defects drawn with red color form the neutral defect complex [In_{Cd}^{+} - [In_{Cd}^{+} - V_{Cd}^{2-}]$^-$]^0.

$$[In_{Cd}]^+ + [In_{Cd}^+ - V_{Cd}^{2-}]^- \leftrightarrows [In_{Cd}^+ - [In_{Cd}^+ - V_{Cd}^{2-}]^-]^0 \qquad (2.9)$$

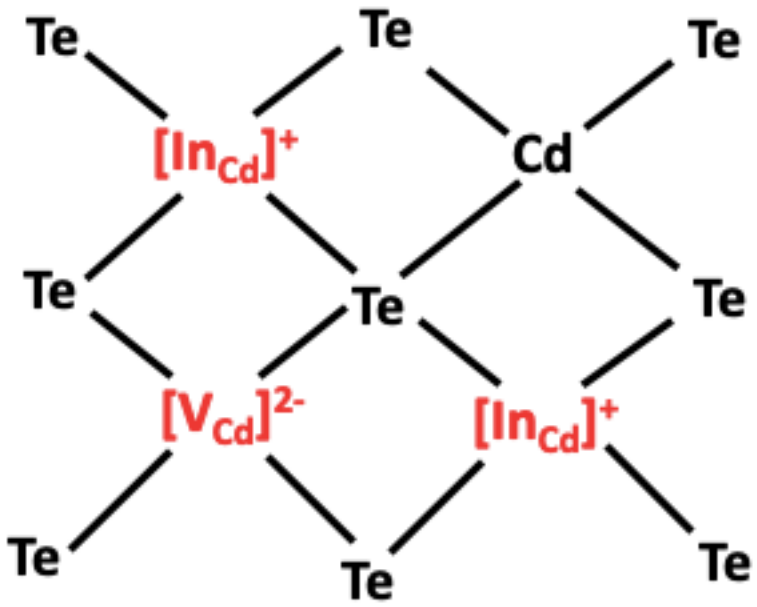

Figure 10 - A model of the neutral defect complex [In_{Cd}^{+} - [In_{Cd}^{+} - V_{Cd}^{2-}]$^{-}$]^{0}.

Cd vacancy compensation by ionized donors increases the electrical resistivity and reduces the leakage current of CZT detectors.

In the near band edge region of CZT PL spectra, donor bound exciton (D, X) and acceptor bound exciton (A, X) peaks are usually observed. Part of the doped indium acts as hydrogenic shallow donors by substituting Cd sites, and thus, the intensity of (D, X) peak may increase with intentional indium doping. Moreover, Cl is employed in CdZnTe to produce high resistivity material. Cl on a Te site is a shallow donor with a binding energy of 14 meV, and the chlorine related A-center has a binding energy of 120 meV [50].

2.7.11 Level positions of the vacancies, A-centers and residual impurities

The singly positively charged V_{Te}^{+} level is at E_{VB} + 200 meV. The cation vacancy V_{Cd}^{2-} is obtained at $E < E_{VB}$ + 470 meV. The A-centers (cation-vacancy donor complexes) act as single acceptors with binding energies approximately 125-170 meV above the valence

band. The donor is either a group-III donor located on the Cd sublattice (such as In) or a group-VII donor located on Te sublattice (such as Cl). These defects contribute to the $D_{complex}$ band in CZT. Donor- and acceptor-level positions are shown in Figure 11 [51].

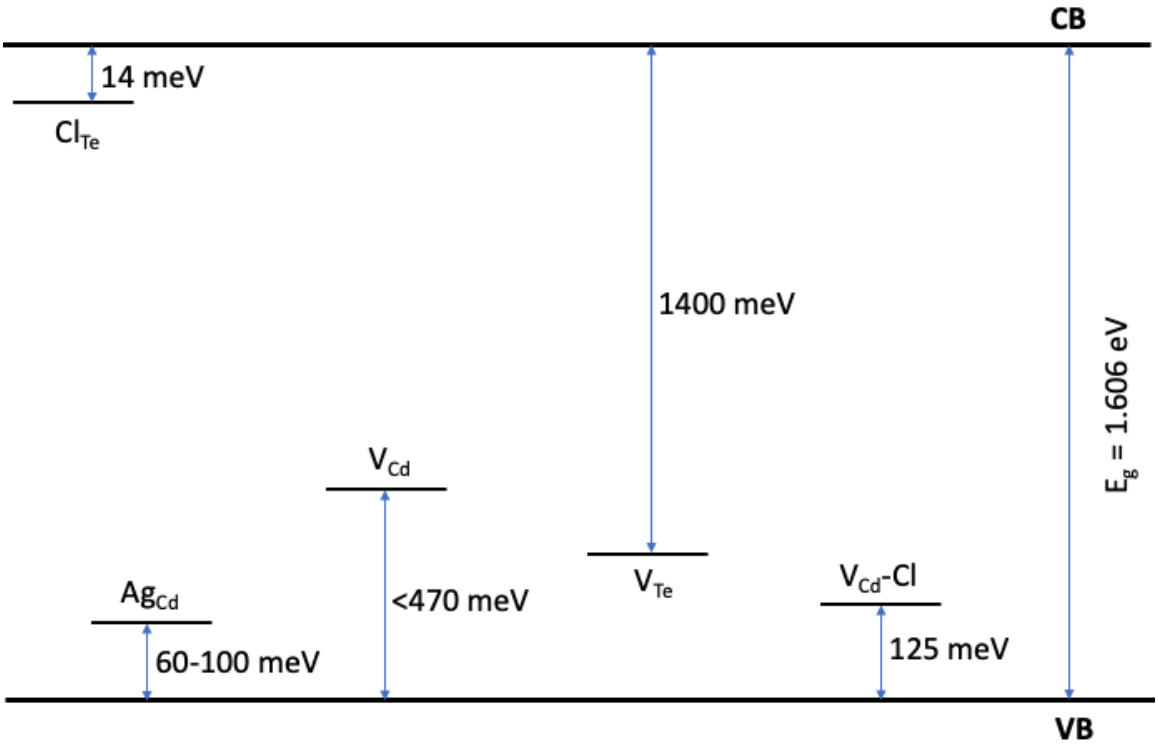

Figure 11 - Level positions of the vacancies, A-centers and residual impurities in CdTe:Cl at 4.2K.

3 Materials and Methods

This chapter introduces photoluminescence spectroscopy as the experimental method employed in this project, and provides information about the CZT samples used in this study.

3.1 Photoluminescence setup

In photoluminescence spectroscopy, photons with energy greater than the bandgap of the material are directed onto the surface of the semiconductor material. A variety of sources are used to excite the samples. A 532nm frequency-doubled diode-pumped YLF laser with 0.2 mW average power, 20 ns long pulses, 2 KHz repetition rate, 2.33 eV photon energy, and about 128nm penetration depth inside CZT material is used as the green excitation source (green laser). Additionally, a 488 nm Ar-ion CW laser with 2.54 eV photon energy, and about 74 nm penetration depth inside CZT material is employed with a line filter (blue laser). Further, a 365 nm UV LED with 3.4 eV photon energy, 9.5 mW power, and about 17 nm penetration depth near the surface of CZT material is used with a bandpass filter, to investigate the surface of the studied CZT samples. Each excitation source provides certain information about the samples. Because the absorption coefficient of the semiconductor is wavelength dependent, longer wavelength light penetrates deeper into the sample. Figure 12 plots the penetration depth in CdTe as a function of the excitation photon energy in the region of our measurements. It is worth noting that the penetration depth depends on the zinc fraction x, and the CZT penetration will be bigger. The penetration depth is inversely proportional to the photon energy in the region of our measurements.

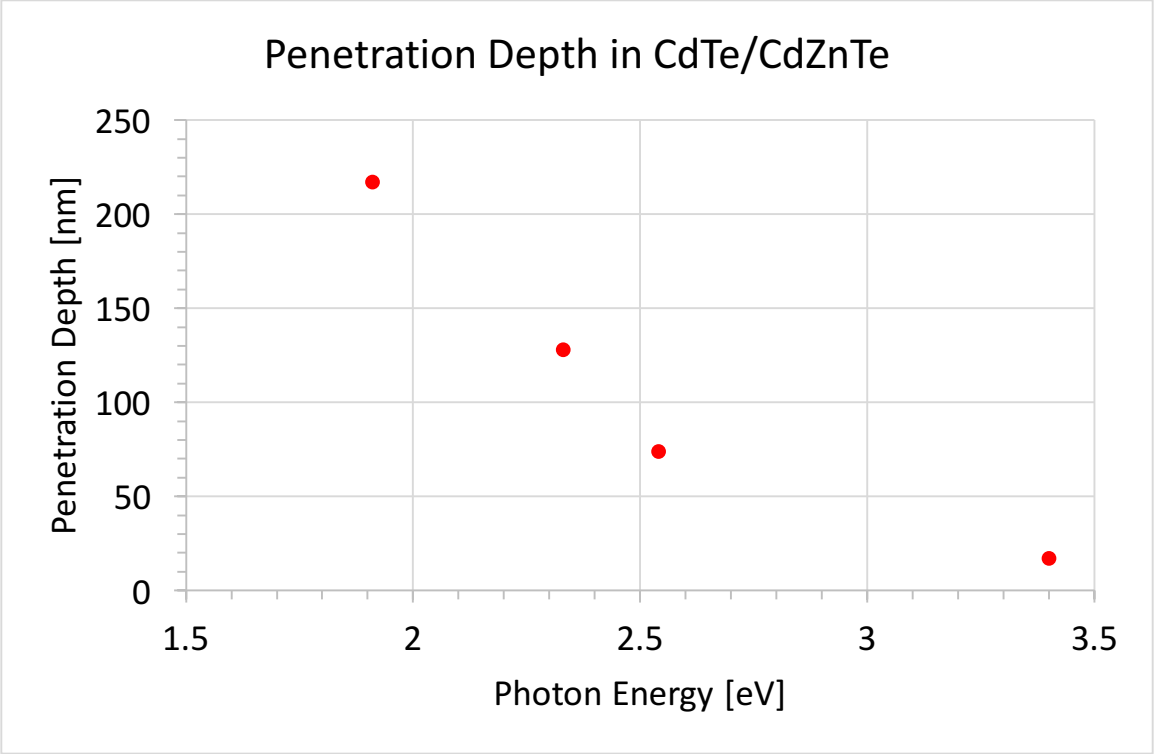

Figure 12 - The penetration depth in CdTe as a function of the excitation photon energy in the region of our measurements.

The electron-hole pair recombine after a certain lifetime and emit photons with different energies. The emission spectrum of the sample is collected by an optical setup. As shown in Figures 13 and 14, the optical setup consists of a parabolic mirror, a lens, and an optical filter. For the UV LED setup, a bandpass filter is used in front of the LED, as shown in Figure 15. The parabolic mirror reflects and collimates the PL emission towards the focusing lens. The focusing lens focuses the PL light on the entrance slit of a SpectraPro 300i monochromator. The widths of the entrance and exit slits of the monochromator are 500 μm, and 100 μm respectively. The optical filter blocks the laser stray light and the harmonics, to ensure that only CZT PL is analyzed. The monochromator disperses the PL onto a liquid nitrogen-cooled InGaAs array detector of 256 pixels. Each pixel has a width

of 100 μm. The detector operates at -100° C. Gratings of 150 lines/mm with a resolution of 22.5 meV, and 600 lines/mm with a resolution of 5.6 meV are used in the monochromator. The detected light spectrum is displayed on a computer screen. Additionally, the background is measured separately with the excitation source off and then subtracted from the sample emission spectrum.

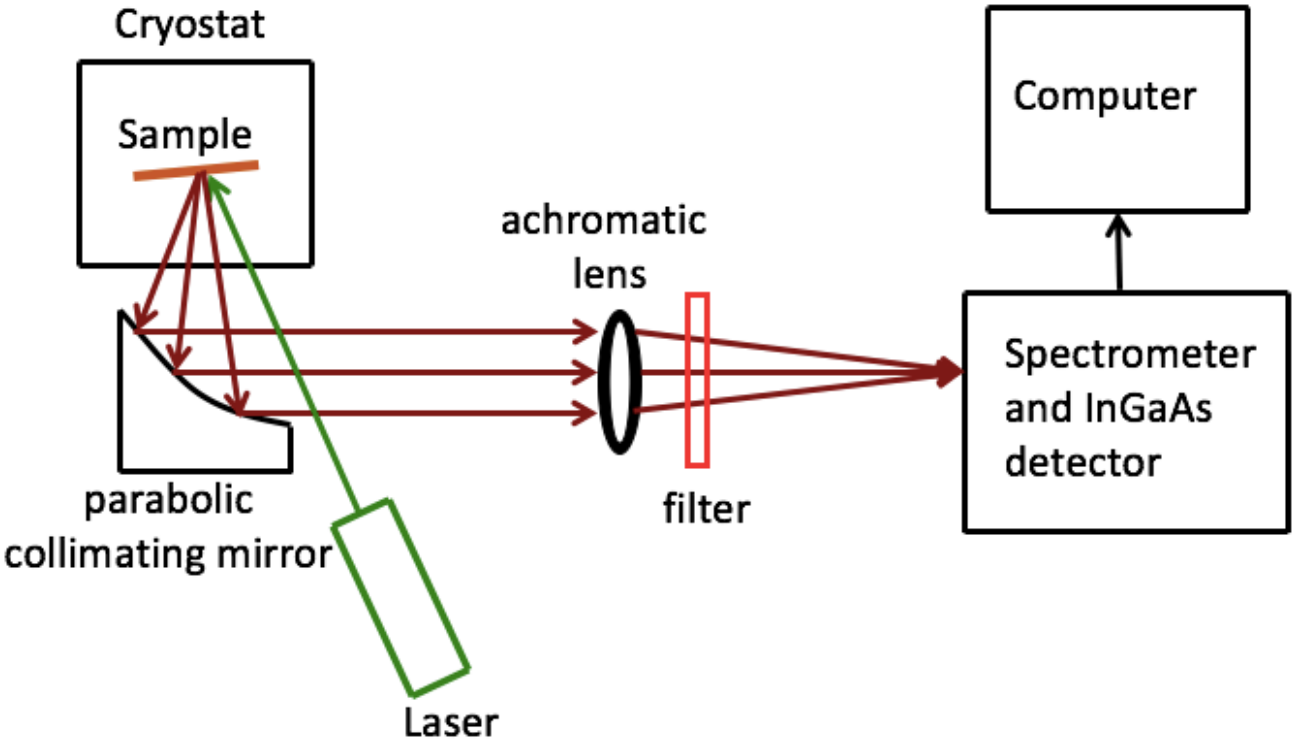

Figure 13 - A schematic diagram of the low temperature photoluminescence set up.

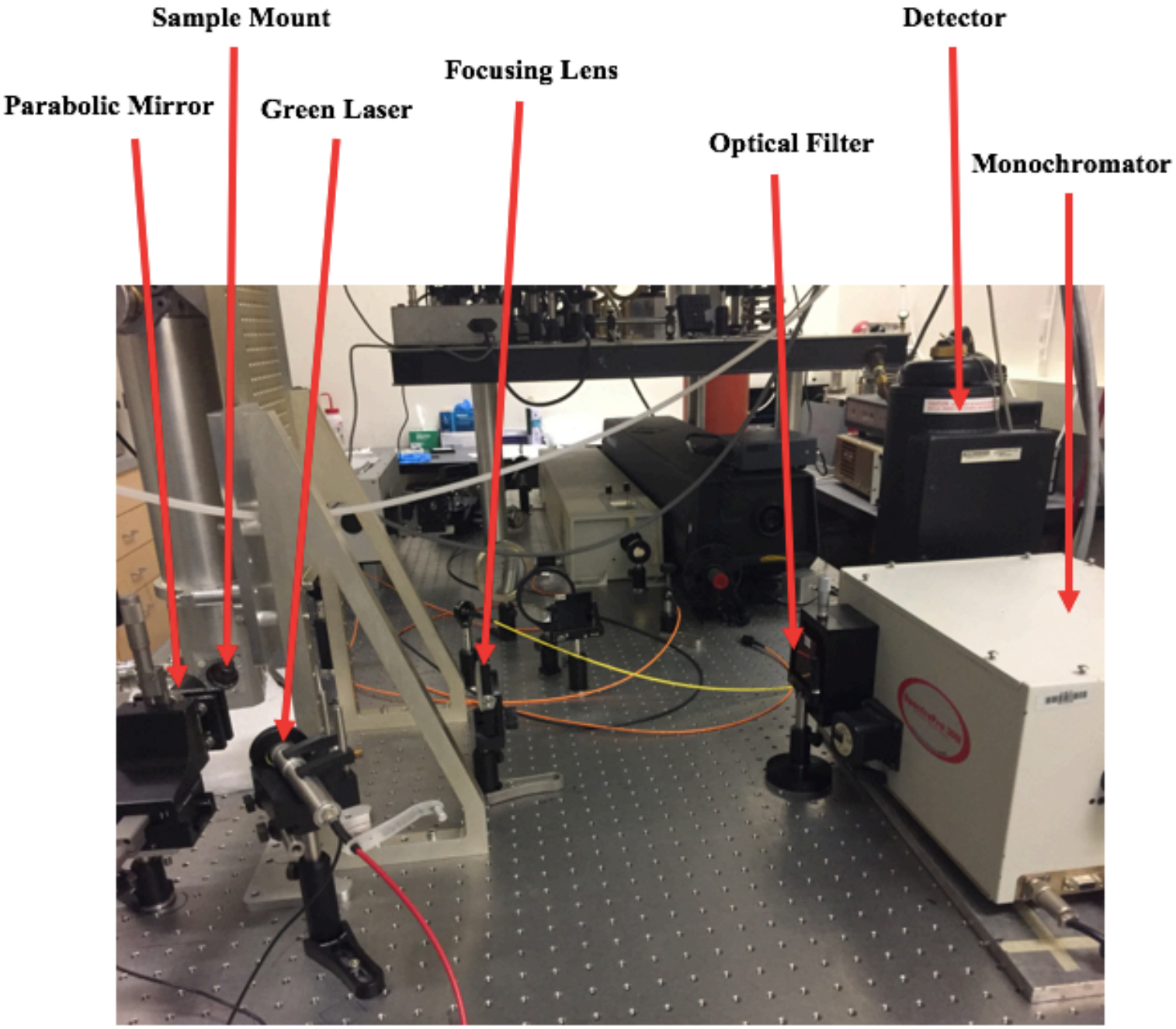

Figure 14 - Low temperature photoluminescence experimental set up using green laser as the excitation source.

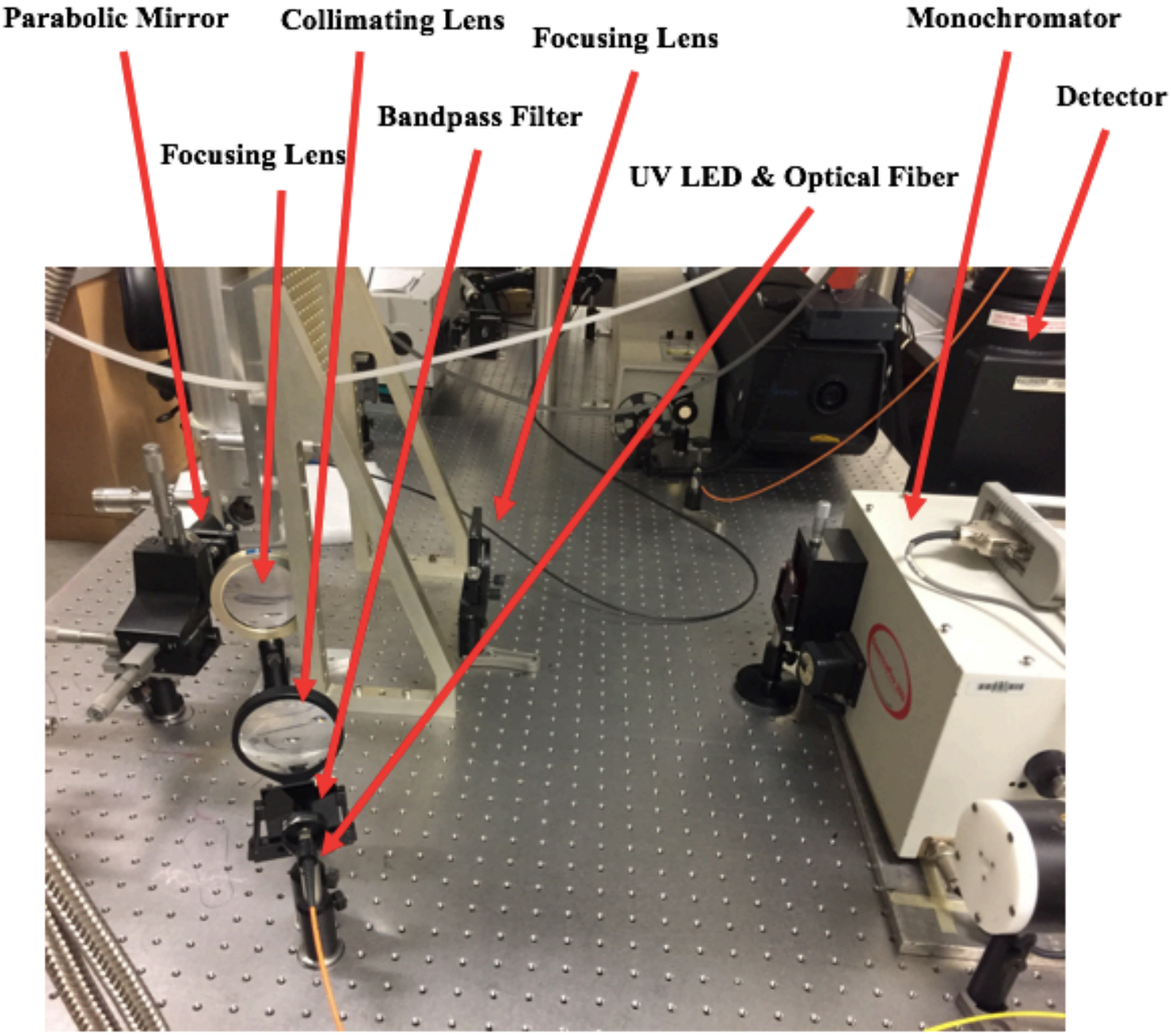

Figure 15 - Photoluminescence experimental set up used for oxide surface investigation using UV LED as the excitation source.

As Figure 16 shows, the monochromator grating disperses different wavelengths into different special positions based on the Bragg's law: $n\lambda = 2d\sin(\theta)$. All the $n\lambda$ wavelengths come out of the monochromator with the same grating angle. A long pass optical filter is used to block the harmonics of the stray lights and prevent them from interfering with the sample PL emission. In our PL setup, a 610nm cut off filter is used for a harmonic free wavelength range, from 600nm to 1200nm.

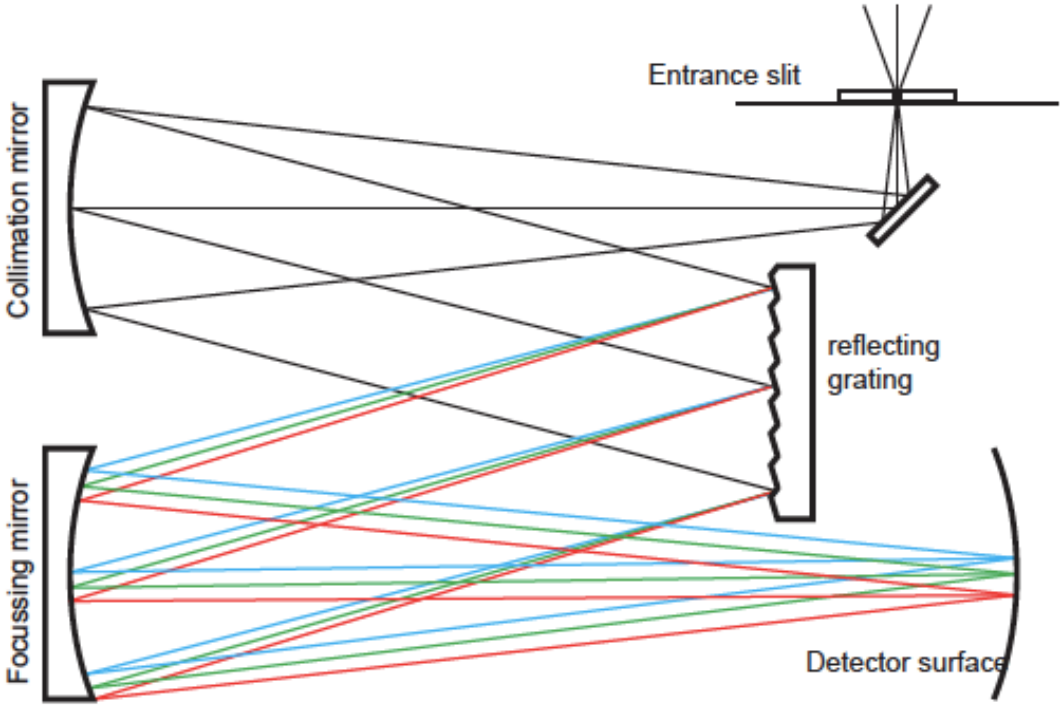

Figure 16 - A schematic diagram of the diffraction grating monochromator.

The components of the optical system have wavelength dependencies which affect the shape of the emission spectrum. Thus, the optical setup was calibrated and the transfer function of the optical setup was calculated as a function of wavelength. The calibration was done by using a tungsten-halogen lamp as a reference, the bulb can be considered as an ideal blackbody at 3200 K. In order to get the final PL spectrum of a sample, we divide

the measured spectrum by the optical system transfer function. Figure 17 shows the transfer function of the optical system used in our experiments. In this figure, the 150 grooves/mm grating is used. Each line of the six overlapping lines in the figure corresponds to a different grating position, which in turn corresponds to a different measured wavelength interval.

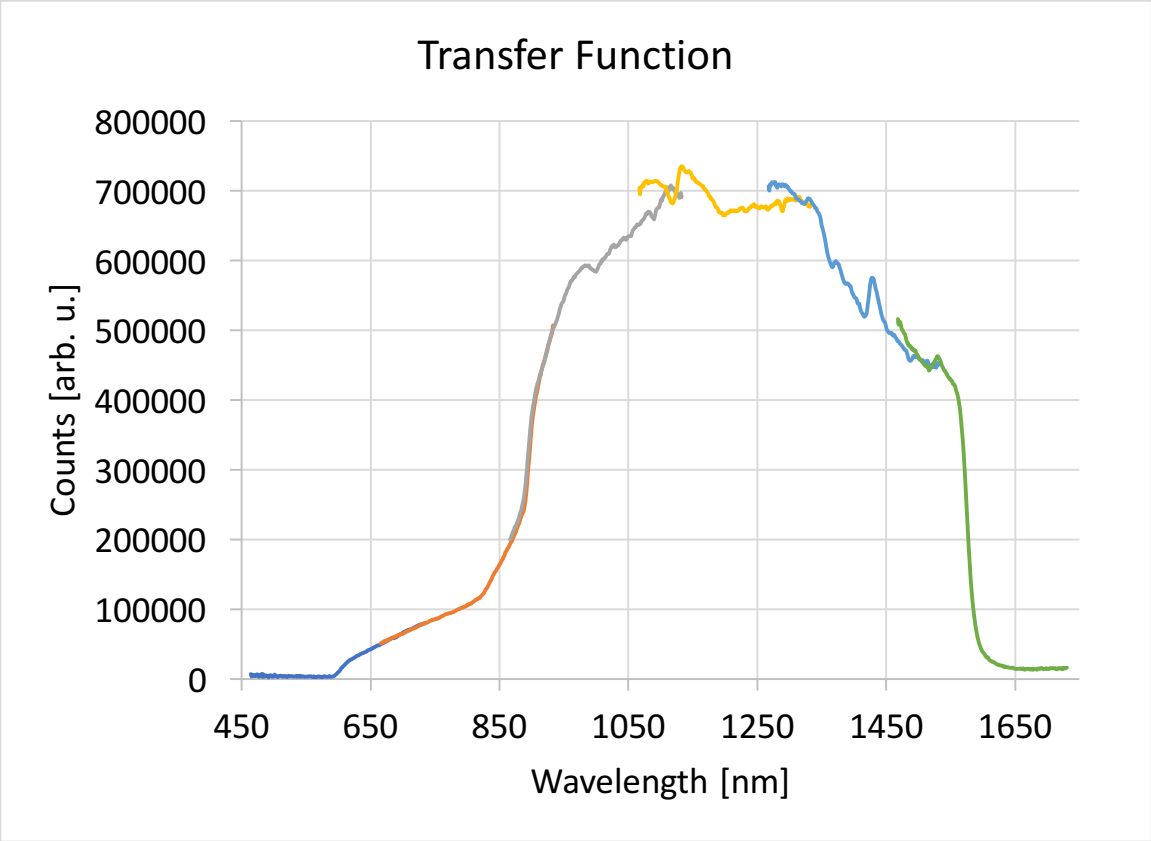

Figure 17 - The transfer function of the optical system used in our experiments.

Low temperature PL has a great significance in semiconductor defect investigations. A cryostat is a device to cool samples down to less than 9K, and it is useful for optical and electrical measurements. Figure 18 shows a schematic diagram of a closed cycle helium cooled cryostat. A refrigerator connected to a helium compressor cools a copper pillar. The copper pillar has a heater and a temperature sensor inside. The sample holder is screwed to

the end of the pillar and covered with a cap. The cap has 4 quartz windows for optical measurements and a pumping line to evacuate the space around the sample. The temperature sensor detects the pillar temperature, and the temperature is set by a controller. A 9-300 K temperature range is accessible with our cryostat.

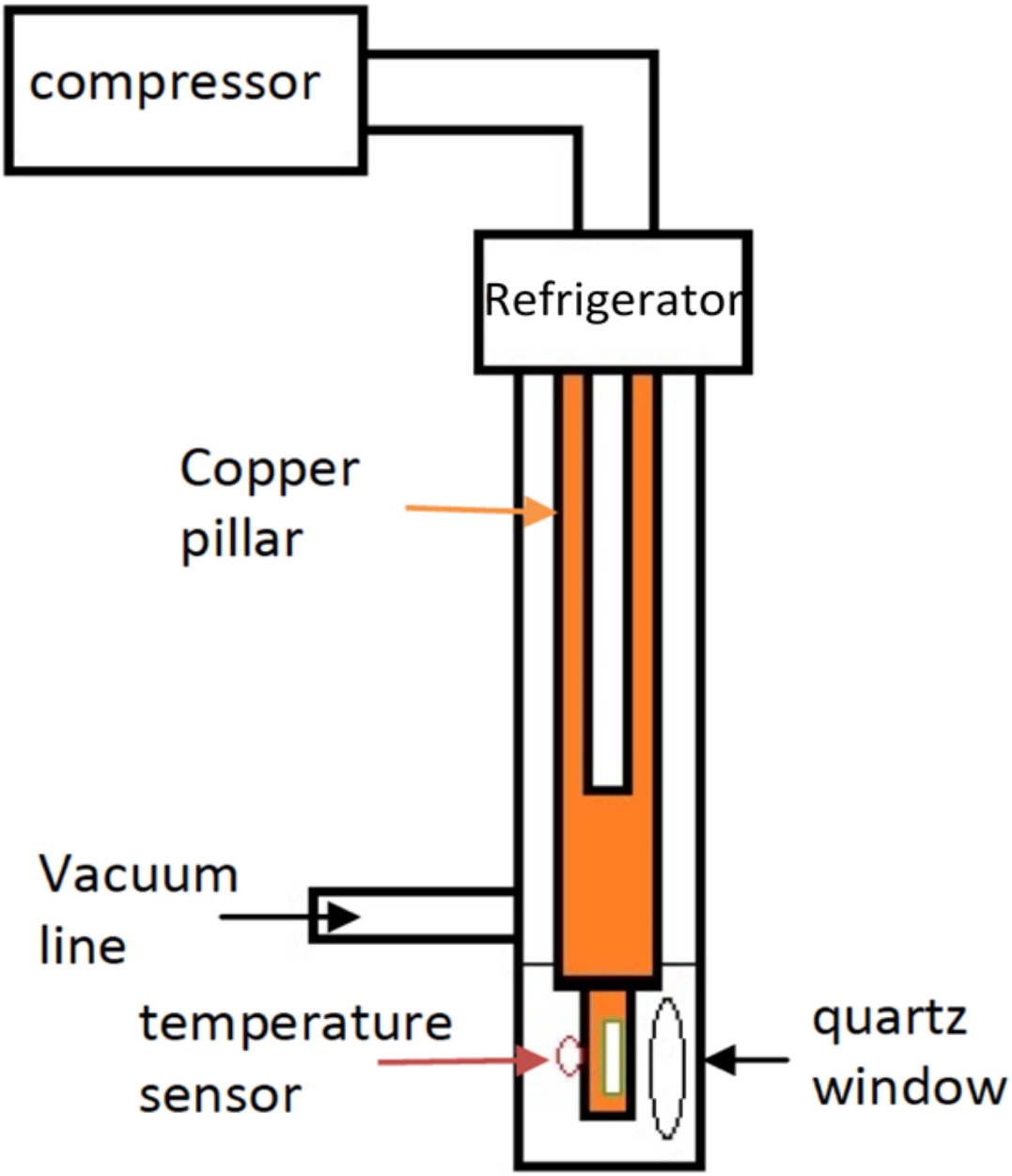

Figure 18 - A closed cycle helium cryostat system used for low temperature PL [54].

3.2 CZT samples

Different CZT samples with nominal zinc molar concentration of 10% were provided by Redlen. The samples surface was mechanically polished in order to remove the damaged surface layer, then they were etched and passivated with H_2O_2 aqueous solution. Besides the values of the resistivity and stability of the samples, no further information about the samples was provided by Redlen due to confidentiality reasons. Stability is the change of the average output counts when the detector is exposed to a constant x-ray flux for one second. The samples have different resistivity and stability and further investigations on the differences among them were needed. No correlations between resistivity, stability, and PL peaks intensity have been found. Nevertheless, PL is used to further study the samples and understand the features of their defects and impurities. In addition to that, PL is used to optimize the surface oxidation processing of these CZT samples. Table 4 shows the resistivity and stability differences among the samples.

Table 4 - CZT samples investigated in our work.

Sample	Resistivity [Ω.cm]	Stability %
5083-98-3	5.55×10^9	-0.76
4912-84-2	5.74×10^9	0.22
4762-85-1	5.85×10^9	-0.91
4392-98-2	7.52×10^9	-1.93
4392-94-4	9.09×10^9	-1.66
4272-98-1	1.17×10^{10}	—
4746-84-1	1.38×10^{10}	-2.16
4746-73-3	1.52×10^{10}	-2.02
4272-98-6	1.86×10^{10}	—

3.3 Surface Processing

There is a significant correlation between surface properties and charge generation, charge collection, and detector performance, thus, it is important to optimize the surface processing in device fabrication. Non-stoichiometric surface, and dangling bonds lead to higher surface leakage currents and lower the radiation detector performance [13]. Mechanical polishing of the crystal surface is performed to reduce crystal damage, scratches and roughness induced from cutting of the ingot. Further, the roughness is decreased by chemical etching, as the surface layer of material is etched away and a flat and smooth surface is left behind. Etching gives a Te-rich surface. Bromine in methanol (Br-MeOH) is a common acidic etchant for CZT surface treatment. Te has a relatively smaller band gap (~0.3 eV), thus, Te enrichment changes the stoichiometry of the surface [13].

Oxidizing the Te rich surface develops surface passivation layer, and hence minimizes the surface leakage current. H_2O_2 passivating agent has been used to passivate CZT surfaces. The thickness and composition of the oxide layer formed depend on the bromine in methanol concentration employed, and the concentration, and exposure duration of the H_2O_2 passivating agent [53].

In photoluminescence, the semiconductor PL is affected by non-radiative recombination at the semiconductor surface. The more surface recombination the weaker the PL. Surface recombination also increases leakage currents. Passivating the surface suppresses surface recombination, and thus increases the PL intensity. Consequently, the semiconductor PL intensity is a proxy for leakage current.

4 Results and Discussion

In this chapter, the results of the experiments and measurements on different CZT samples, followed by discussions on those results are presented. First, we present a typical low temperature photoluminescence spectrum of a CZT crystal obtained from our work. Next, the low temperature (9K) PL spectra of two samples are presented. Then, several comparisons among nine different samples are performed. Also, excitation power dependence and temperature dependence are investigated. Additionally, the uniformity of a CZT sample is examined. Further, the PL spectra of $Cd_{0.9}Zn_{0.1}Te$ and $Cd_{0.96}Zn_{0.04}Te$ are compared. Moreover, the defects and impurities near the surfaces of the two faces (B and A) of sample (4272-98-1) are investigated. We also use different excitation wavelengths to investigate a $Cd_{0.96}Zn_{0.04}Te$ sample at different depths from its surface.

4.1 Typical low temperature PL spectrum

A typical low temperature photoluminescence spectrum of a CZT crystal obtained from our work is shown in Figures 19 and 20.

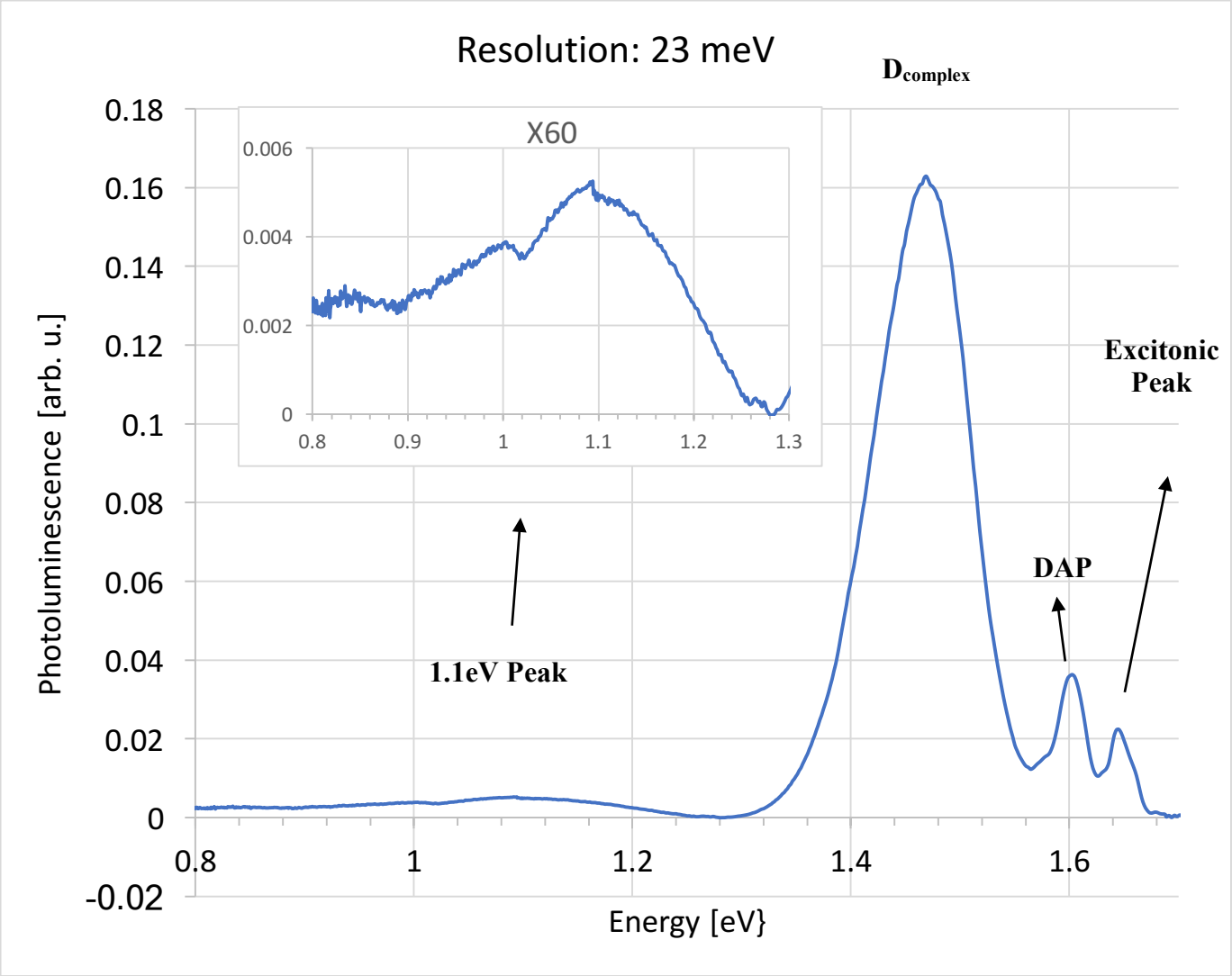

Figure 19 - Typical PL spectrum of CZT crystal of sample (4272-98-1) excited by a blue laser with photon energy of 2.54 eV at 9K temperature using a resolution of 23 meV.

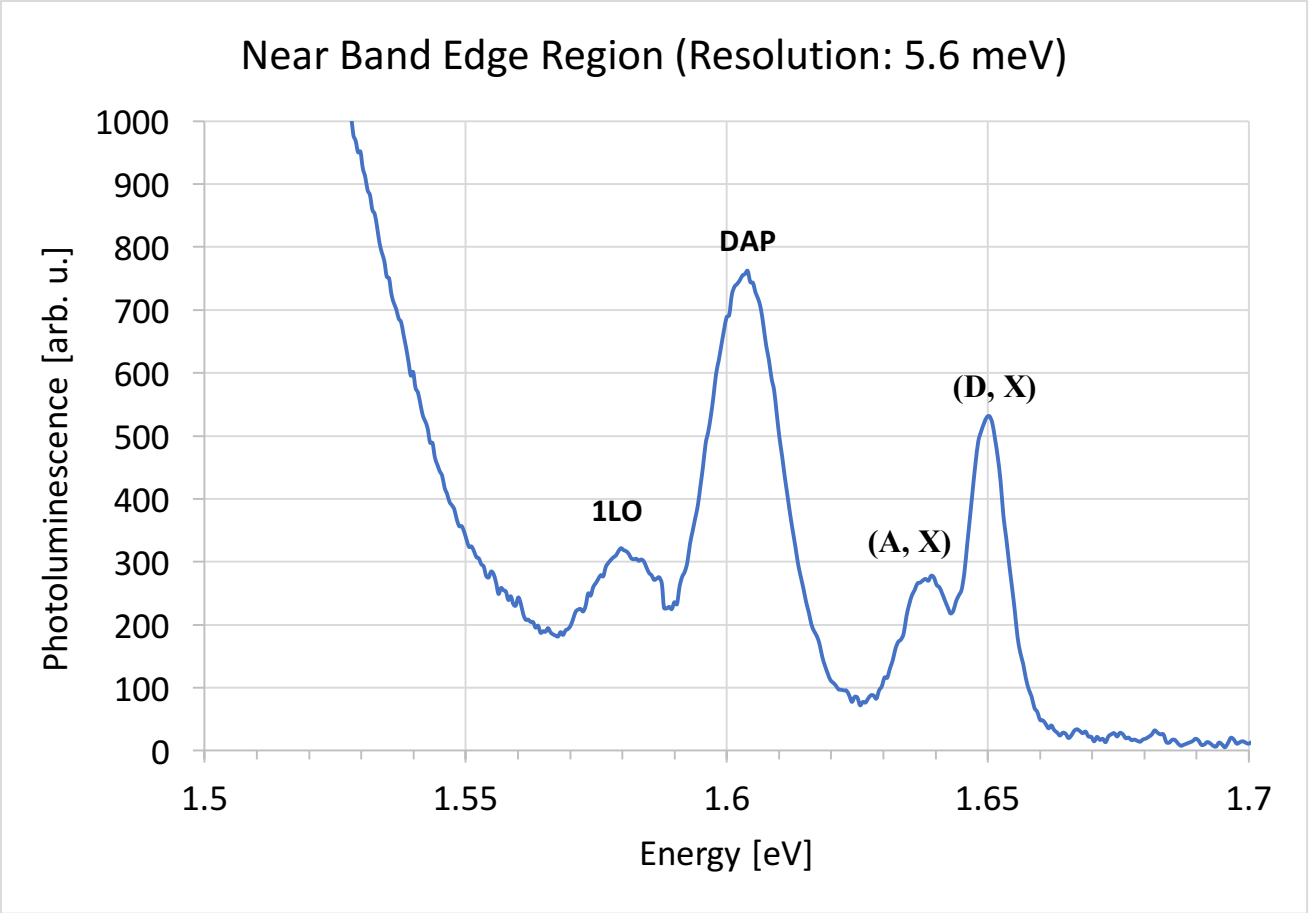

Figure 20 - Typical PL near band edge region spectrum of CZT crystal of sample (4272-98-1) excited by a blue laser with photon energy of 2.54 eV at 10K using a resolution of 5.4 meV.

It is evident from the figures that CZT PL spectra typically consist of three regions; near band edge region, donor acceptor region, and defect related region. The near band edge region contains exciton peaks. The exciton peaks are usually donor bound exciton (D, X) and acceptor bound exciton (A, X). Indium dopants act as hydrogenic shallow donors by substituting Cd sites, and thus, they can bind free excitons to form bound excitons. The (D, X) peak lies 13.0 meV below the bandgap energy E_g. This peak can therefore be used as a reliable indicator of the bandgap E_g. Figure 20 shows that (D, X) is located at 1.65 eV, thus the bandgap of sample (4272-98-1) CZT crystal is 1.663 eV. Acceptor bound excitons (A,

X) may be attributed to excitons bound to Cd vacancies (V_{Cd}^{2-}) that act as shallow acceptors in CZT. (A, X) may also be ascribed to Cu impurities in the material.

The donor acceptor region has a shallow donor acceptor peak (DAP) and its LO phonon replicas. DAP is attributed to a recombination between shallow donor levels and shallow acceptor levels. Further, the defect related region contains a wide peak called $D_{complex}$, and the deep level 1.1eV peak. The identification of the defect related emission is crucial for understanding the effects of crystal defects and impurities. The $D_{complex}$ peak is very broad and it might be related to multiple overlapping emissions with different energies. A-center is likely to contribute to this defect related emission. A-centers originate from a complex of a Cd vacancy and an In donor $[In_{Cd}^{+} - V_{Cd}^{2-}]^{-}$. The doped indium atoms act as hydrogenic shallow donors $[In_{Cd}]^{+}$ by substituting for Cd sites. Indium donors with surrounding Cd vacancies create the singly negative donor-vacancy complex (A center) $[In_{Cd}^{+} - V_{Cd}^{2-}]^{-}$ as described in equation 4.1.

$$[In_{Cd}]^{+} + [V_{Cd}]^{2-} \leftrightarrows [In_{Cd}^{+} - V_{Cd}^{2-}]^{-} \quad (4.1)$$

The wide 1.1 eV PL peak results from recombinations of deep donor–deep acceptor pairs [44-55]. Table 5 lists common impurities in CZT. These impurities were determined using glow discharge mass spectroscopy performed on CZT samples grown at Charles University. Indium, Li, Na, P, and Al are shallow impurities. Copper, Ag, Fe, Sn, and Sb are deep impurities [44, 55].

Table 5 - Common impurities in CZT samples grown at Charles University [44].

Element	Conc. [ppb]	Element	Conc. [ppb]
Li	< 2	Fe	< 20
B	13	Cu	< 10
Na	< 2	In	2000
Al	33	Ag	< 30
Si	20	Cl	8
P	1	Sn	< 15
S	210	Sb	< 15

Figure 21 is a simple energy level model of CZT:In crystal [60]. The figure shows the energy levels introduced by In donors $[In_{Cd}]^{+}$, Te antisites $[Te_{Cd}]^{4+}$, Cd vacancies $[V_{Cd}]^{2-}$, and A-centers $[In_{Cd}{}^{+} - V_{Cd}{}^{2-}]^{-}$.

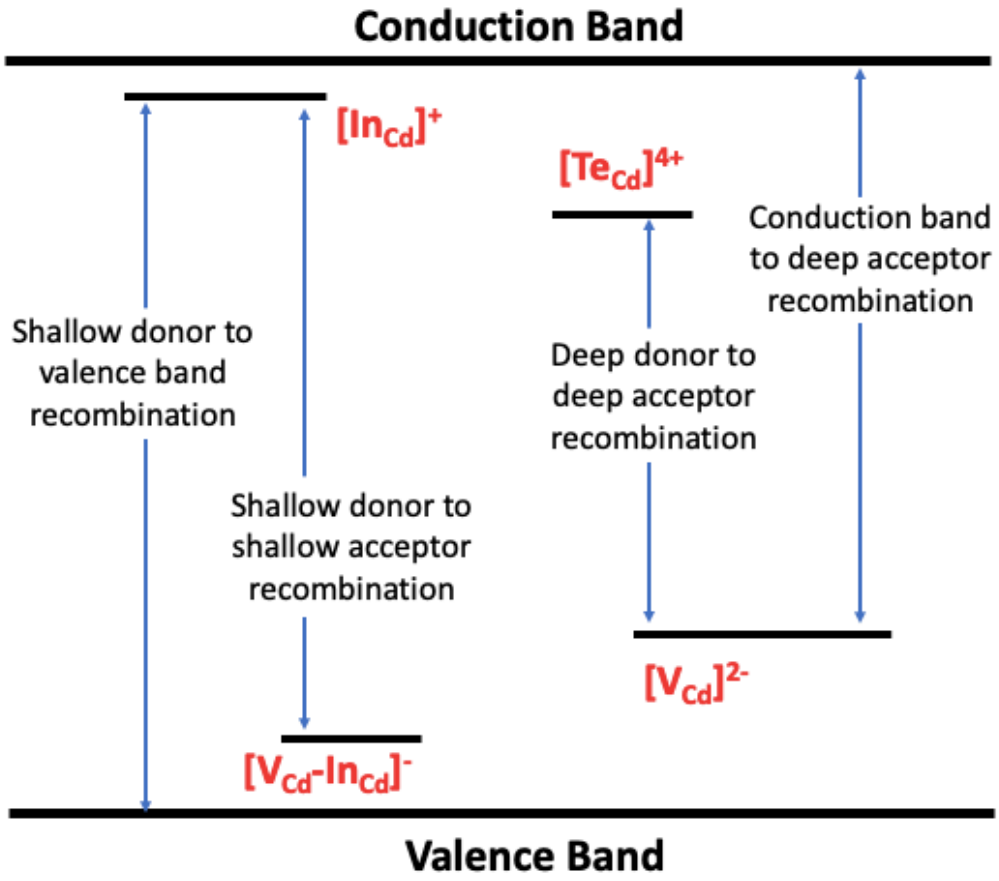

Figure 21 - Energy level model of CZT:In crystal.

Since the absorption coefficient of the semiconductor is wavelength dependent, each excitation source used in our work has a specific penetration depth in CZT [56]. Aiming at obtaining as much information about the characterized CZT crystals as possible, we use three different excitation sources; green laser, blue laser, and UV LED. The spectra of each sample are shown below. Afterwards, we analyze the results and try to further understand the correlations between the peaks and the differences among the samples, in order to learn more about the samples, and their defects and impurities, and to give feedback to crystal growers and fabrication technicians so as to improve the quality of CZT detectors.

4.2 Sample 5083-98-3

4.2.1 Green Excitation

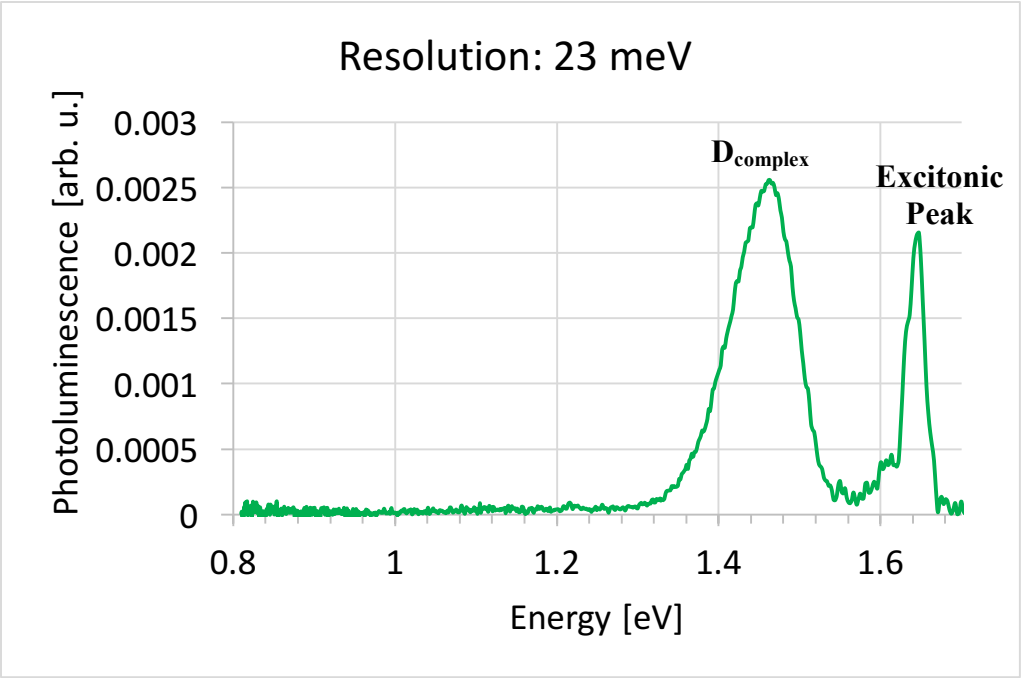

Figure 22 - PL spectrum of sample (5083-98-3) excited by a green laser with photon energy of 2.33 eV at 9K temperature using a resolution of 23 meV.

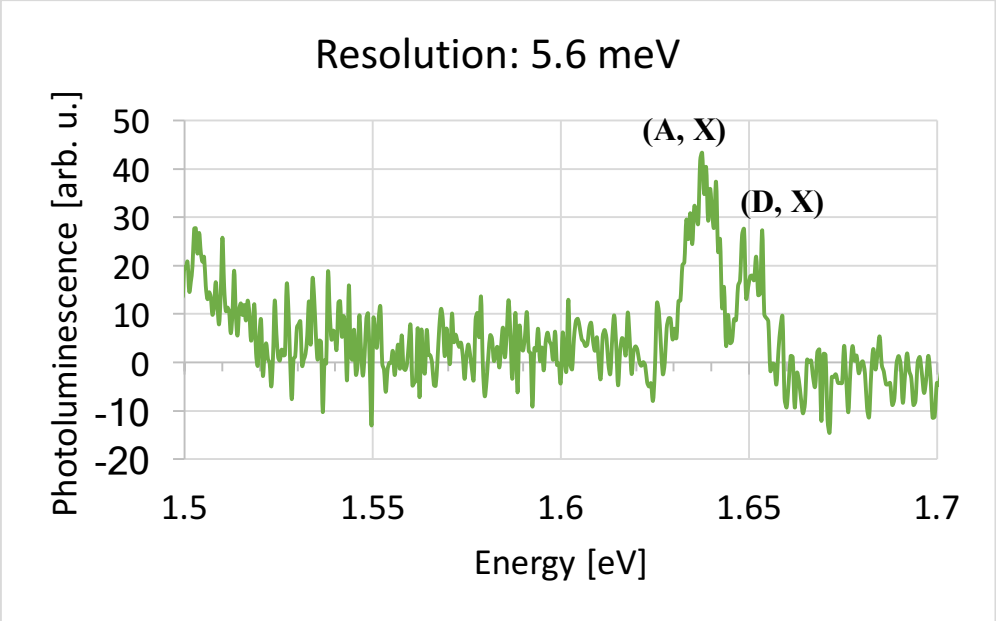

Figure 23 - Typical PL near band edge region spectrum of sample (5083-98-3) excited by a green laser with photon energy of 2.33 eV at 9K using a resolution of 5.6 meV.

4.2.2 Blue Excitation

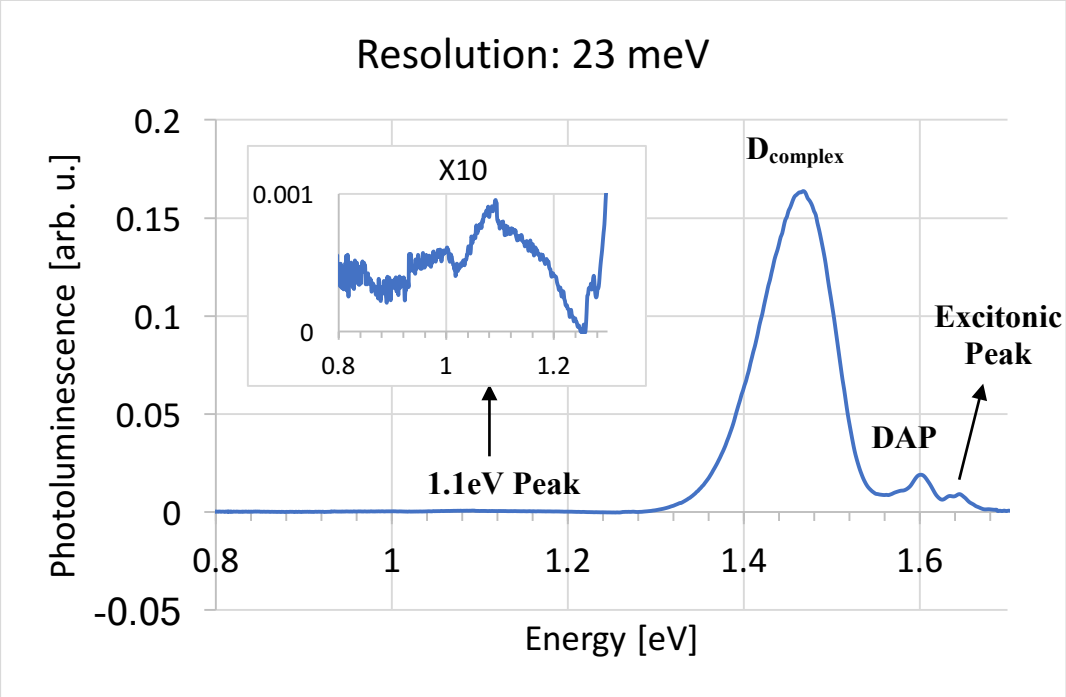

Figure 24 - PL spectrum of sample (5083-98-3) excited by a blue laser with photon energy of 2.54 eV at 9K temperature using a resolution of 23 meV.

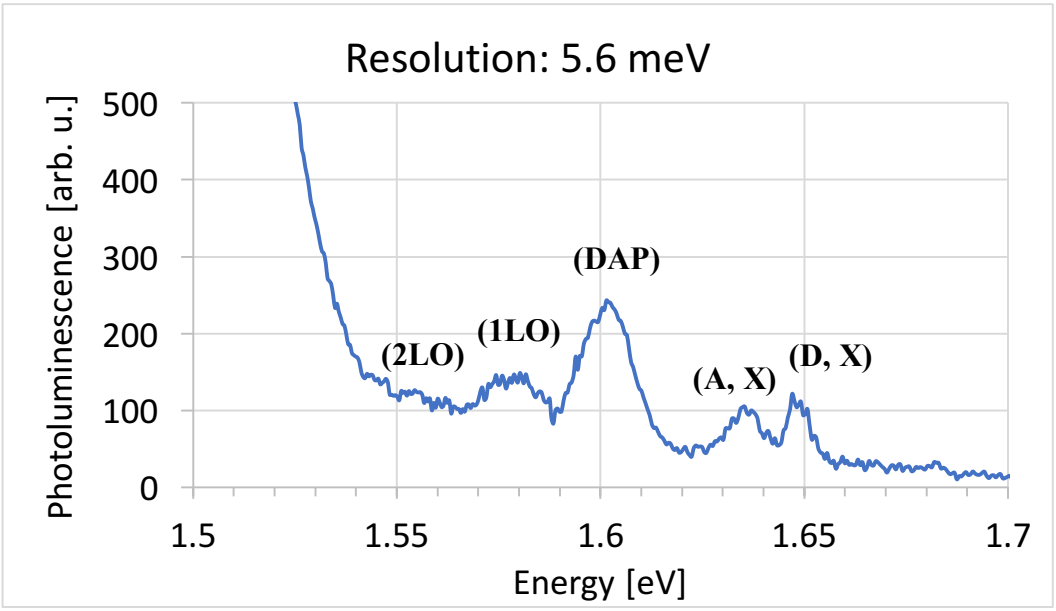

Figure 25 - Typical PL near band edge region spectrum of sample (5083-98-3) excited by a blue laser with photon energy of 2.54 eV at 10K using a resolution of 5.6 meV.

When sample (5083-98-3) is excited with the 2.33eV photon energy green laser, its PL spectrum shows a donor bound exciton (D, X) peak is situated at 1.651 eV. The acceptor bound exciton (A, X) is located at the shoulder of the lower energy side at 1.639 eV. The shallow donor acceptor pair DAP emission and its longitudinal optical phonon replica LO peak also exist. Additionally, the frequently found $D_{complex}$ wide peak is present at 1.467 eV. I(D, X)/I($D_{complex}$) is 0.513, I(A, X)/I($D_{complex}$) is 0.84, and I(D, X)/I(A, X) is 0.61.

When exciting the sample with the 2.54eV photon energy blue laser, the PL spectrum reveals a donor bound exciton (D, X) peak located at 1.649 eV. The acceptor bound exciton (A, X) is situated at 1.636 eV. The shallow donor acceptor pair DAP emission at 1.604 eV and its longitudinal optical phonon replica LO peak at 1.58 eV, are also present. Additionally, the $D_{complex}$ wide peak exists at 1.467 eV. Meanwhile, the 1.1eV deep level defect peak is detected. I(D, X)/I($D_{complex}$) is 0.057, I(A, X)/I($D_{complex}$) is 0.053, I(D, X)/I(A, X) is 1.087, I(DAP)/I($D_{complex}$) is 0.12, and I(1.1eV)/I($D_{complex}$) is 0.00486.

4.3 Sample 4746-73-3

4.3.1 Green Excitation

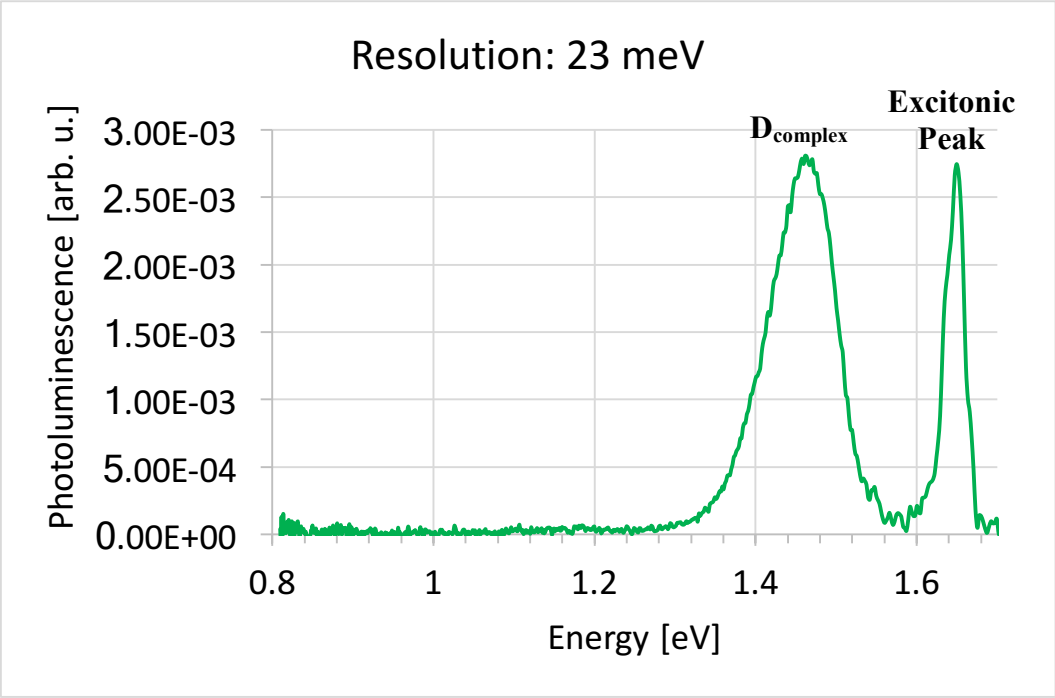

Figure 26 - PL spectrum of sample (4746-73-3) excited by a green laser at 9K temperature using a resolution of 23 meV.

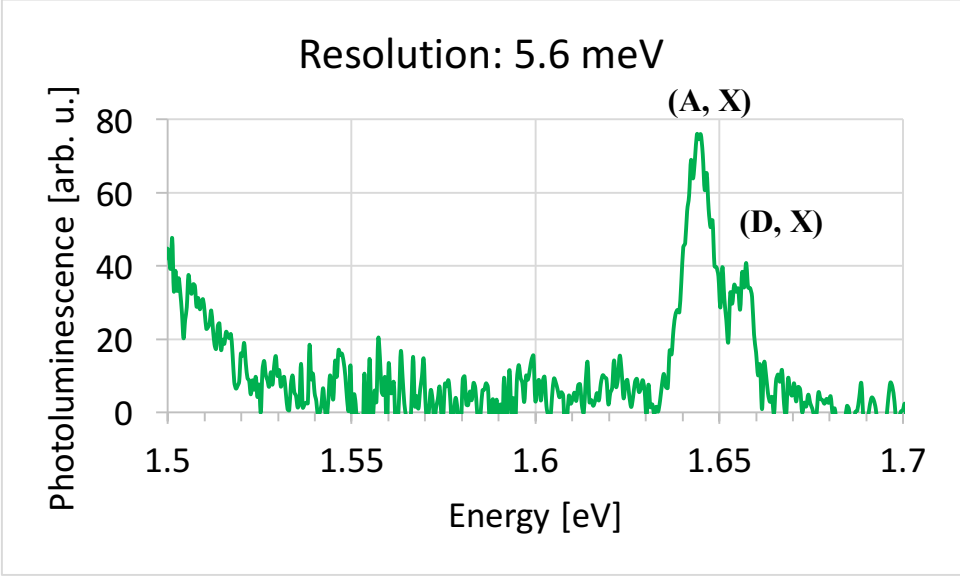

Figure 27 - Typical PL near band edge region spectrum of sample (4746-73-3) excited by a green laser at 9K using a resolution of 5.6 meV.

4.3.2 Blue Excitation

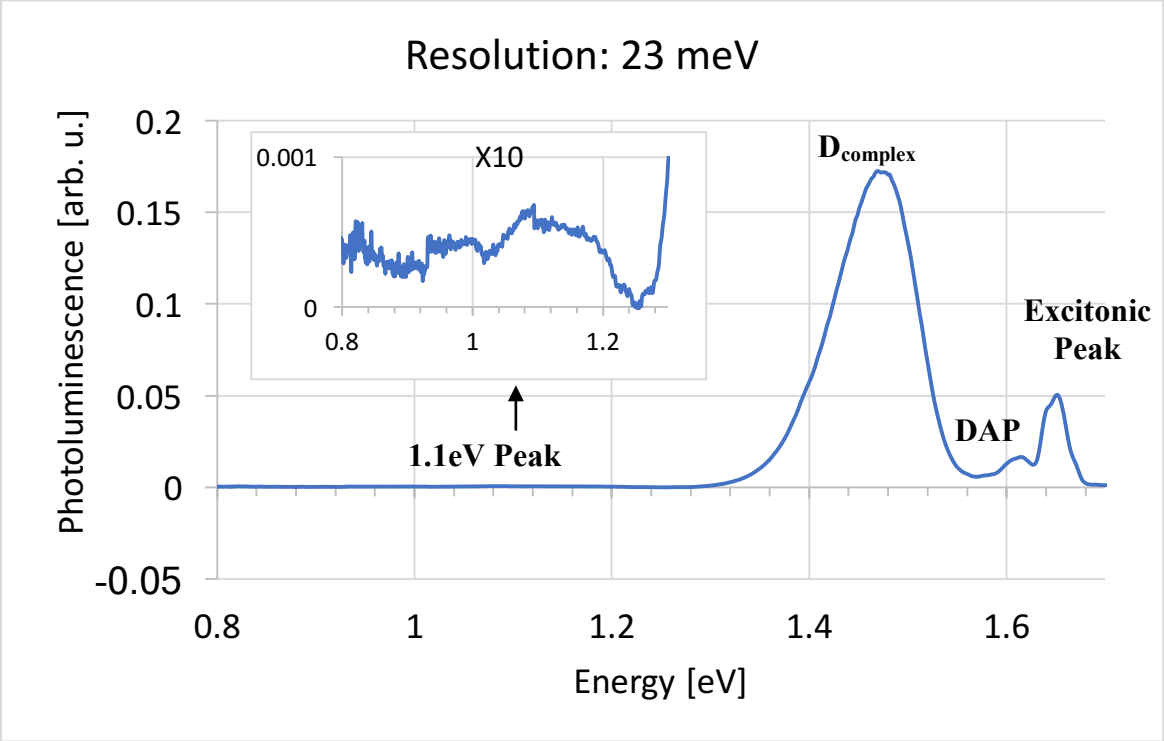

Figure 28 - PL spectrum of Sample (4746-73-3) excited by a blue laser at 9K temperature using a resolution of 23 meV.

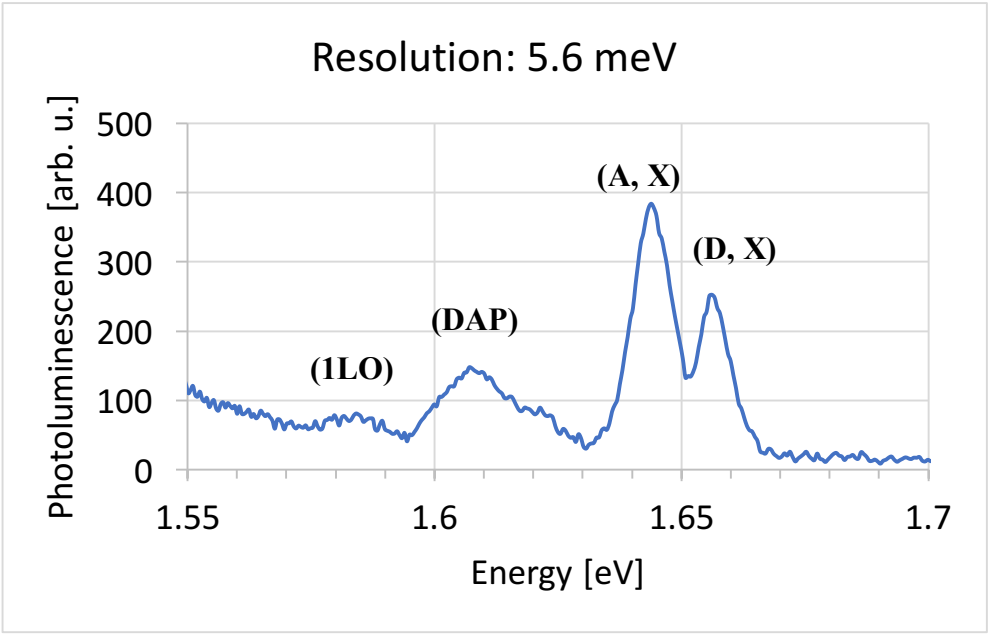

Figure 29 - Typical PL near band edge region spectrum of sample (4746-73-3) excited by a blue laser at 10K using a resolution of 5.6 meV.

When sample (4746-73-3) is excited with the green laser, its PL spectrum shows a donor bound exciton (D, X) peak is situated at 1.657 eV. The acceptor bound exciton (A, X) is located at the shoulder of the lower energy side at 1.644 eV. Additionally, the frequently found $D_{complex}$ wide peak is present at 1.465 eV. I(D, X)/I($D_{complex}$) is 0.526, I(A, X)/I($D_{complex}$) is 0.98, I(D, X)/I(A, X) is 0.538.

When exciting the sample with the blue laser, the PL spectrum reveals a donor bound exciton (D, X) peak located at 1.656 eV. The acceptor bound exciton (A, X) is situated at 1.644 eV. The shallow donor acceptor pair DAP emission at 1.61 eV and its longitudinal optical phonon replica LO peak at 1.585 eV, are also present. Additionally, the $D_{complex}$ wide peak exists at 1.473 eV. Meanwhile, the 1.1eV deep level defect peak is detected. I(D, X)/I($D_{complex}$) is 0.193, I(A, X)/I($D_{complex}$) is 0.293, I(D, X)/I(A, X) is 0.658, I(DAP)/I($D_{complex}$) is 0.11, and I(1.1eV)/I($D_{complex}$) is 0.00324.

4.4 (D, X) peak position and the bandgap energy E_g

The (D, X) peak lies 13.0 meV below the bandgap energy E_g. This peak can therefore be used as a reliable indicator of the bandgap E_g. Provided that a reliable relationship between the bandgap and the zinc fraction is available, the position of the (D, X) peak gives a convenient means of tracking Zn fraction inside the CZT samples [72]. Figure 30 plots the PL spectra of samples (4746-73-3) and (5038-98-3). (D, X) peak is located at 1.656 eV for sample (4746-73-3), however the peak is centered at 1.649 eV for sample (5038-98-3). Using the relation given below, the fractions of zinc deduced for sample (4746-73-3), and sample (5038-98-3) are 0.115, 0.103 respectively.

$$E_g = 1.606 + 0.52x + 0.254x^2, \qquad (4.2)$$

where x is the fraction of Zn concentration in CZT samples, and E_g is the bandgap energy of CZT materials [73].

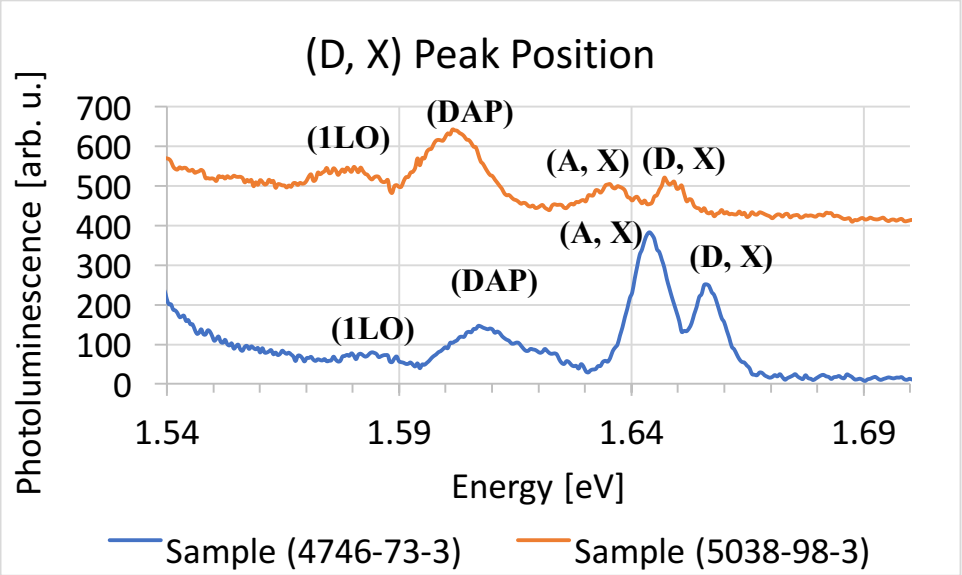

Figure 30 - Low temperature (9K) PL near band edge region spectra of samples (4746-73-3 and 5038-98-3) excited by a blue laser using a resolution of 5.6 meV.

4.5 $Cd_{0.9}Zn_{0.1}Te$ and $Cd_{0.96}Zn_{0.04}Te$

The lattice constant of CZT material depends on the zinc concentration. Manufacturing CZT using a 4% Zn concentration allows the lattice constant to be matched to that of HgCdTe, an infrared detecting material, in order to be used as a growth substrate. These substrates are used for military applications such as night vision googles and IR tracking cameras in drones [75].

(D, X) peak position can be used as a reliable indicator of the bandgap as mentioned above. CZT with 4% zinc concentration is predicted to have a lower bandgap than that of $Cd_{0.9}Zn_{0.1}Te$. Thus, the (D, X) peak of the $Cd_{0.96}Zn_{0.04}Te$ sample is expected to be at a lower energy compared to the $Cd_{0.9}Zn_{0.1}Te$ sample [76]. Figure 31 plots the PL near band

edge region spectra of $Cd_{0.96}Zn_{0.04}Te$ and $Cd_{0.9}Zn_{0.1}Te$ samples. (D, X) peak is located at 1.614 eV for $Cd_{0.96}Zn_{0.04}Te$, however the peak is centered at 1.657 eV for $Cd_{0.9}Zn_{0.1}Te$. It is clear from the figure that $Cd_{0.96}Zn_{0.04}Te$ possesses a lower bandgap energy evidenced by the (D, X) peak position. Applying equation 4.2, the fractions of zinc deduced for $Cd_{0.96}Zn_{0.04}Te$ and $Cd_{0.9}Zn_{0.1}Te$ are 0.0396, 0.116 respectively.

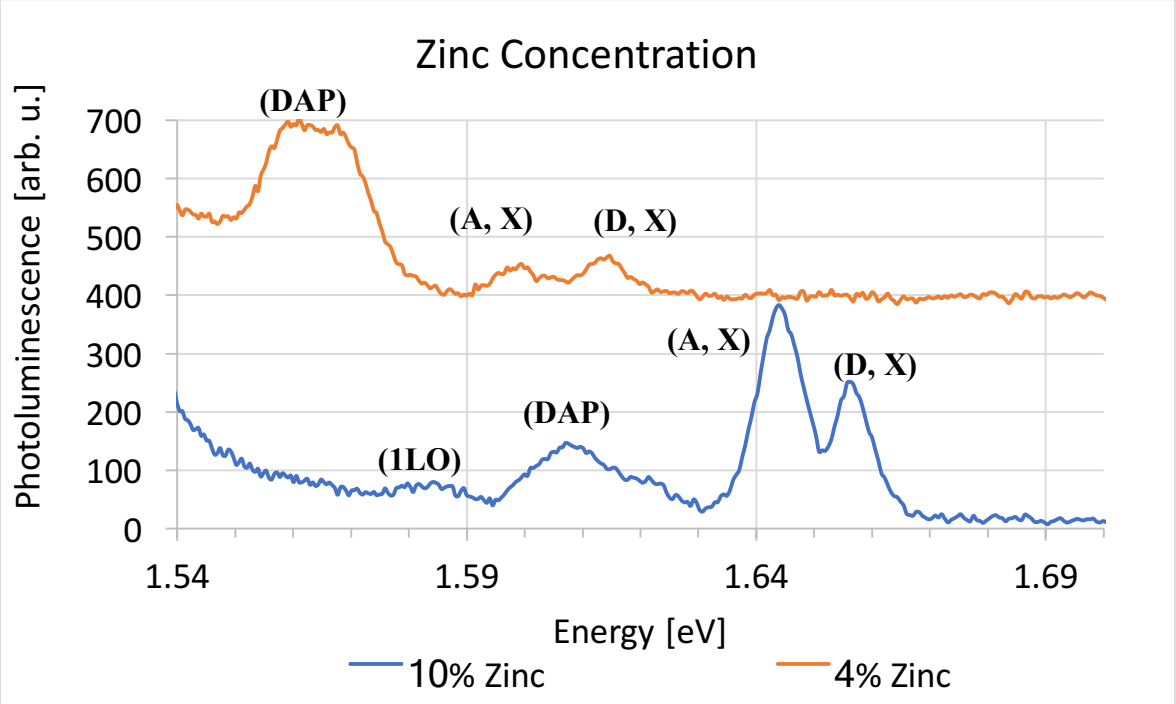

Figure 31 - Low temperature (9K) PL near band edge region spectra of samples ($Cd_{0.9}Zn_{0.1}Te$ and $Cd_{0.96}Zn_{0.04}Te$) samples excited by a blue laser using a resolution of 5.6 meV.

4.6 Uniformity of CZT sample (4746-84-1)

Previous studies indicated that the uniformity of CZT detectors plays an important role in the performance of gamma-ray spectrometers [22]. Since the position of (D, X) peak can be used as a reliable indicator of the concentration of Zn, we use the PL method to investigate the variations of Zn concentration across the CZT sample (4746-84-1), and to examine its uniformity. In this experiment, we scan the sample across the middle of its height, and took 6 low temperature (9K) PL measurements. The scan is done manually, the

spot size is approximately 1mm, and the spacing between spots is roughly equal. The accuracy of measuring zinc concentration in our experiment is 0.3%. Figure 32 plots the low temperature PL near band edge region spectrum of each position. From the PL data, it is revealed that the studied sample has good uniformity evidenced by the (D, X) peak that has the same energy of 1.656 for all positions. Also, the relative peak heights are the same.

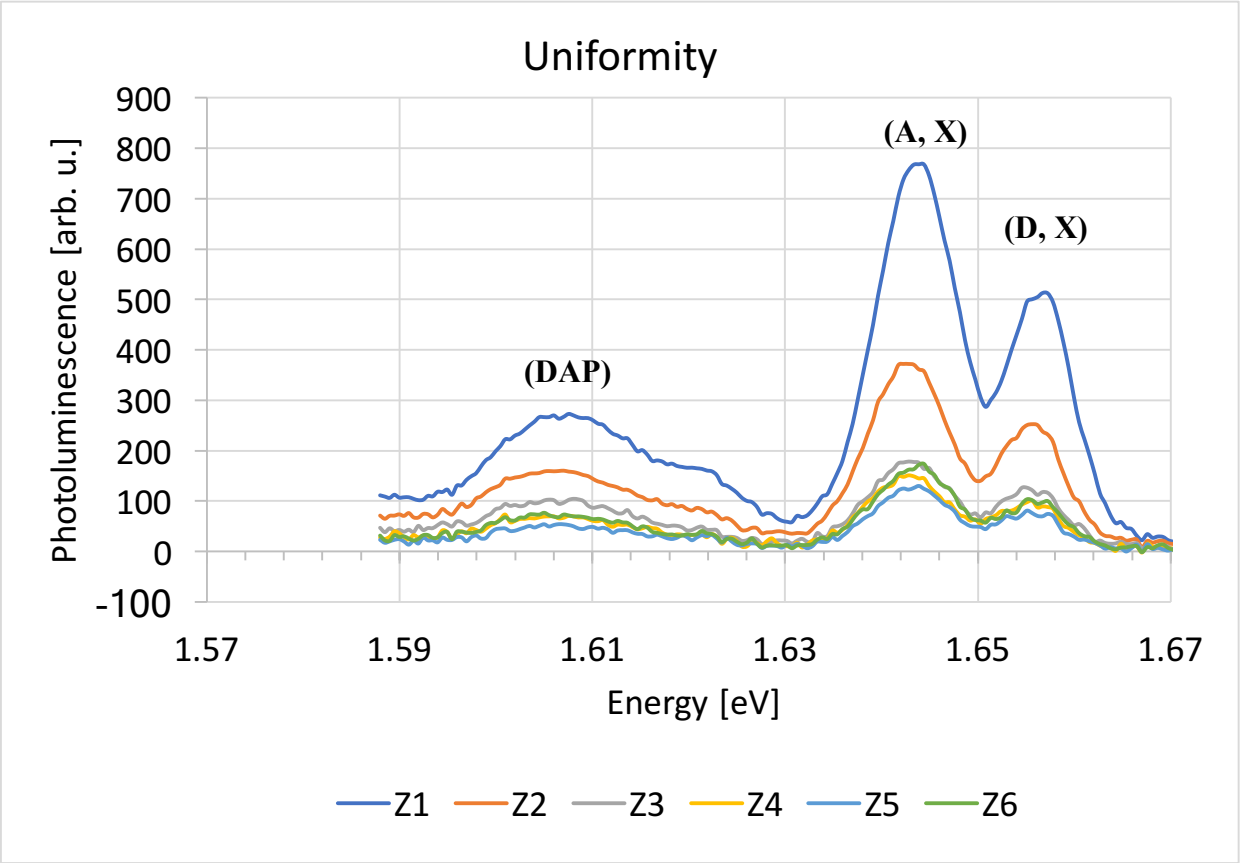

Figure 32 - Low temperature (9K) PL near band edge region spectra of sample (4746-84-1) scanned across the middle of its height by a blue laser of 1 mm spot using a resolution of 5.6 meV.

4.7 $D_{complex}$ and Bound exciton peaks

The defect related emission band located at 1.465 eV is designated as the $D_{complex}$ peak. The identification of the deep energy $D_{complex}$ is crucial for understanding the effects of crystal defects and impurities. Such a band may include two components, one of which

may be associated with the complexes involving Cd vacancies with donors, such as $[\mathrm{In}_{\mathrm{Cd}}^{+} - \mathrm{V}_{\mathrm{Cd}}^{2-}]^{-}$ complex (A-centers), while the other may be ascribed to a luminescence yielded by the recombination of excitons bound to dislocations [57]. The core of dislocations can easily trap impurities such as indium atoms. At higher dislocation density, V_{Cd} defects can be trapped into the dislocations, and thus, the dislocations may play the role of acceptor centers [58].

$D_{complex}$ band is broad which may be caused by multiple overlapping emissions with different energies, it can also be due to variable spacing of the A-centers. The binding energy of a cation vacancy-donor complex in CZT is distributed in a domain from about 120 to about 160 meV. Accordingly, the A-center might be the $[In_{Cd}^{+} - V_{Cd}^{2-}]^{-}$ complex with the binding energy of approximately about 132 meV. Additionally, substitutional impurities like Cu and Ag can give transitions in the same energy range. The Ag ion located at a Cd site could act as an acceptor. The binding energy of the acceptor impurity Ag is about 107 meV, so Ag may partially contribute to the $D_{complex}$ peak [59]. During the growth of CZT, due to the high partial pressure of the Cd component, a large number of Cd atoms evaporate during growth. Hence, a lot of Cd vacancies are formed in the as-grown crystals. This may result in formation of the large number of so-called A-centers complexes comprising a cadmium vacancy and shallow donor. Such complexes have a negative effect on the detector performance, because A-centers can act as effective charge carrier traps. Also, dislocation defects may diminish charge collection in radiation detectors. Carriers can be trapped into the core of a dislocation. In fact, the A-center $[V_{Cd} - In_{Cd}]^{-}$ might greatly contribute to the $D_{complex}$ band. The creation of $[V_{Cd} - In_{Cd}]^{-}$ complex is seen as the evidence of self-compensation. These defect complexes act as acceptors and are responsible for the

self-compensation through the balance between the doped indium donors and the defect complex acceptors. In this case, the $D_{complex}$ recombination is between the shallow donors (e.g., In_{Cd}) and the A-center acceptor level. On the other hand, it has been reported before that $D_{complex}$ emission peak might be attributed to complexes [V_{Cd}-Te_{Cd}]. It has also been thought that, $D_{complex}$ peak could be ascribed to the transition of a donor to cadmium vacancies [60].

Excitonic signatures in the low temperature PL spectra of semiconductor of high optical quality usually appear as the intense lines caused by the excitons bound to donor and acceptor centers. In this case the energy levels of the bound excitons move down from the free exciton level by the amount equal to their energy binding. This energy depends on the nature of the impurities or intrinsic defects. General speaking, the PL spectra for a high-quality sample is dominated by the excitonic luminescence, while that of a poor-quality sample is dominated by defect-related luminescence. Thus, the intensity of the exciton related luminescence relative to the impurity and defect band can be used as an indicator of the overall crystal quality. It is generally accepted that a larger intensity ratio I(bound exciton)/I($D_{complex}$) indicates a lower defect concentration, a lower density of detrimental carrier traps, less surface damage, better crystal quality, and good detector performance [61]. $D_{complex}$ is the defect region associated with crystal imperfection and deeper impurity levels. A lower PL intensity of $D_{complex}$ indicates that the crystals have fewer impurities and defects. For quantitative comparison in terms of material quality, Figure 33 compares PL spectra for samples (4746-73-3) and (4272-98-6). I(bound exciton)/I($D_{complex}$) is 0.98 for sample (4746-73-3), however the intensity ratio is 0.42 for sample (4272-98-6). Accordingly, it is evident that sample (4746-73-3) possesses a higher crystal quality.

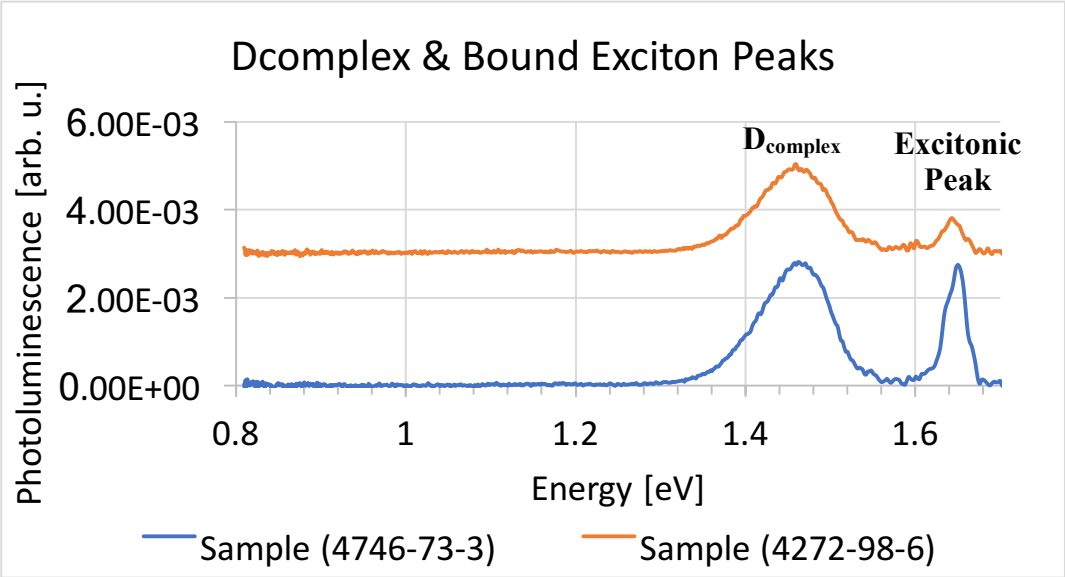

Figure 33 - Low temperature (9K) PL spectra of samples (4746-73-3) and (4272-98-6) excited by a green laser using a resolution of 23 meV.

Several methods can be suggested in order to decrease the intensity of the $D_{complex}$ peak, and hence increase the crystal quality and detector performance. The crystal quality may improve by annealing the sample under CdZn atmosphere due to the reduction of Te precipitates/inclusions and Cd vacancies [67]. Annealing under CdZn atmosphere provides a CdZn rich environment around the sample. In this condition, excess Te may migrate from the inner portion of the sample, and the amount of Te precipitates/inclusions in the inner CZT bulk crystal may be decreased, at the same time Cd atoms may diffuse into the sample and fill Cd vacancies, also the dislocation density may be reduced. Additionally, the defect-related $D_{complex}$ band may further be decreased with annealing in CdZn melt alloy [62]. The liquid environment annealing may remove Ag and other impurities from the CZT wafers, and therefore, partially lower the intensity of the $D_{complex}$ peak. It was previously reported that, aging treatment (the sample was held in dry-air for 72 h at 60 ^{o}C) may decrease the intensity of $D_{complex}$, and reduce the surface trap state and the surface leakage current [48].

It also was stated that adding excess Cd into stoichiometric raw materials may be beneficial for reducing the dislocations in CZT [63]. Cd vacancy acceptors can be compensated by the indium donors [64]. In view of the majority of Cd vacancies compensated by indium shallow donors $[In_{Cd}]^{+}$, the residual Cd vacancies can also be compensated by another donor $[Te_{Cd}]^{4+}$. A simple form of the neutral complex is $[Te_{Cd}^{4+} - 2V_{Cd}^{2-}]^{0}$, which is a complex obtained by one Te antisite and two Cd vacancies [60].

In fact, not all indium dopant locates at the position of Cd atom and form $[In_{Cd}]^{+}$. some of the In atoms exist in the form of In interstitial atom and does not take part in Cd vacancy compensation. Therefore, Cd vacancy acceptors are compensated dominantly by indium $[In_{Cd}]^{+}$ donor and residual by Te antisite $[Te_{Cd}]^{4+}$ donor. Moreover, the high resistivity of CZT crystal is obtained by recombination of acceptor caused by Cd vacancies and indium donors [50, 60]. Cd vacancies make the material conductive (p-type). This can be fixed by adding In which forms complexes with Cd vacancies.

4.8 DAP and (D, X) peaks

The donor acceptor pair DAP peak is associated with transitions from shallow donors to shallow acceptors. The shallow donors may be due to indium. Indium can occupy a Cd vacancy to form In_{Cd}, a shallow donor state. The DAP peak centered at 1.606 eV is deduced to lie at about 60 meV below the conduction band, Eg – 60 meV, which is close to the values for Li (E_a=58) and Na (E_a=58.7) in CZT. Therefore, the DAP transition is probably due to shallow acceptors related to the impurities of Li and Na from the raw materials [65]. It is worth noting that the binding energy of In donor is 14.08 meV [22]. It is evident from Figure 34 that DAP structure has a relatively higher emission intensity for sample (4392-

98-2). However, the peak is not detected in sample (4746-73-3). Thus, we can reasonably consider that sample (4392-98-2) may have a higher concentration of donors and/or acceptors.

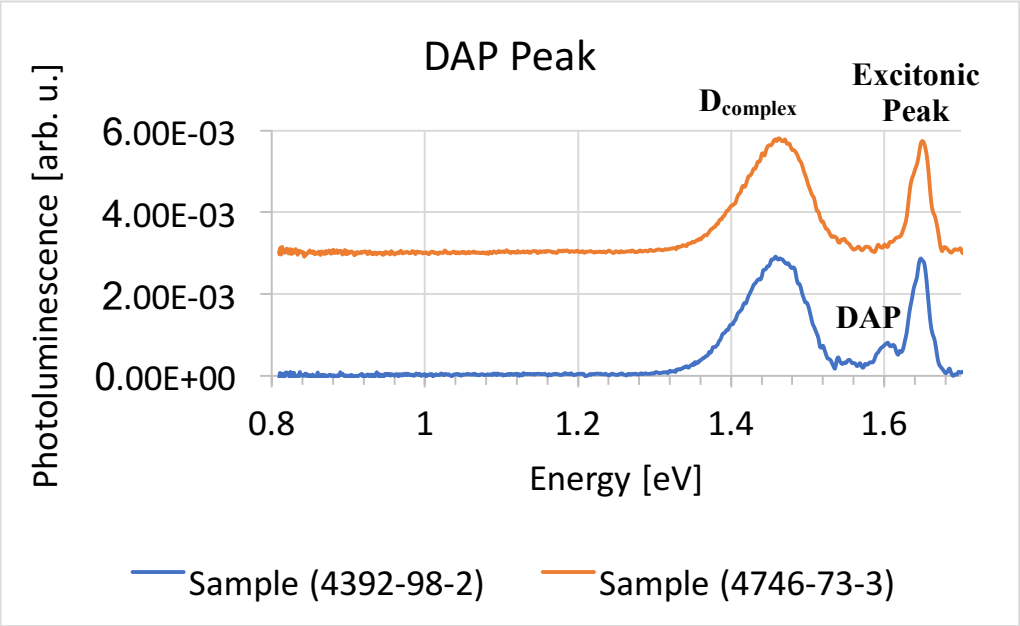

Figure 34 - Low temperature (9K) PL spectra of samples (4392-98-2) and (4746-73-3) excited by a green laser using a resolution of 23 meV.

Since the DAP is broad, we may assume that several shallow acceptors and donors participate in the emission. DAP may be partially attributed to the singly negative complex $[In_{Cd}^{+} - V_{Cd}^{2-}]^{-}$ as the acceptor [66]. Further, the intensity ratio of the DAP emission to the (D, X), I(DAP)/I(D, X), can be related to the density of acceptor levels. Figure 35 plots the PL spectra of samples (4272-98-6) and (4746-73-3). The intensity ratio is 2.82 for sample (4272-98-6), and 0.57 for sample (4746-73-3). Thus, it can be concluded that sample (4272-98-6) has more shallow donors and/or acceptors. In Figure 35, the energy spacing between DAP and 1LO, as well as 1LO and 2LO is about 21.6 meV. This is close to the LO phonon energy of 21.3 meV in CdTe [67].

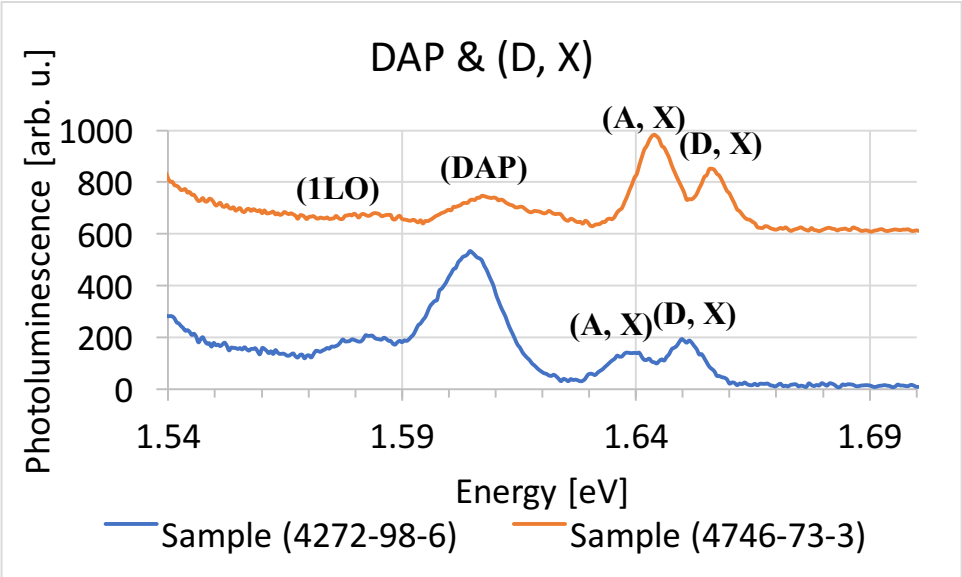

Figure 35 - Low temperature (9K) PL near band edge region spectra of samples (4272-98-6) and (4746-73-3) excited by a blue laser using a resolution of 5.6 meV.

It has been experimentally proved in the literature that, the intensity of the DAP peak decreases with CdZn or Te atmosphere annealing [67-68]. Thus, annealing the samples in CdZn or Te atmosphere may remove part of the impurities. The impurities of Li and Na may migrate from CZT samples to the annealing medium, and the reduction of Li and Na may cause a reduction in the DAP emission [68]. Also, the Cd-saturated annealing may result in the dissociation of the defect complexes $[In_{Cd}^{+} - V_{Cd}^{2-}]^{-}$.

4.9 Free Exciton Peak

Typically, free excitons can migrate in the crystals. During this process, some defects in the crystals can bind free excitons and form bound excitons [63]. The excitation energy of free excitons is slightly less than the bandgap energy E_g of the semiconductor. The detection of the free exciton line is an indication of the good crystal quality of the sample. A good CZT material quality is required to enhance the free-carrier transport properties.

Because of the greater degree of alloy broadening for x = 0.1, the free exciton peak is barely resolvable from the donor-bound exciton [69]. Figure 36 illustrates that the free exciton might be resolvable in the spectrum of sample (4746-84-1), accordingly, sample (4746-84-1) might have a better crystal quality. However, in sample (4392-94-4), the free exciton peak is not resolvable, indicating that the crystal of sample possesses a lower quality.

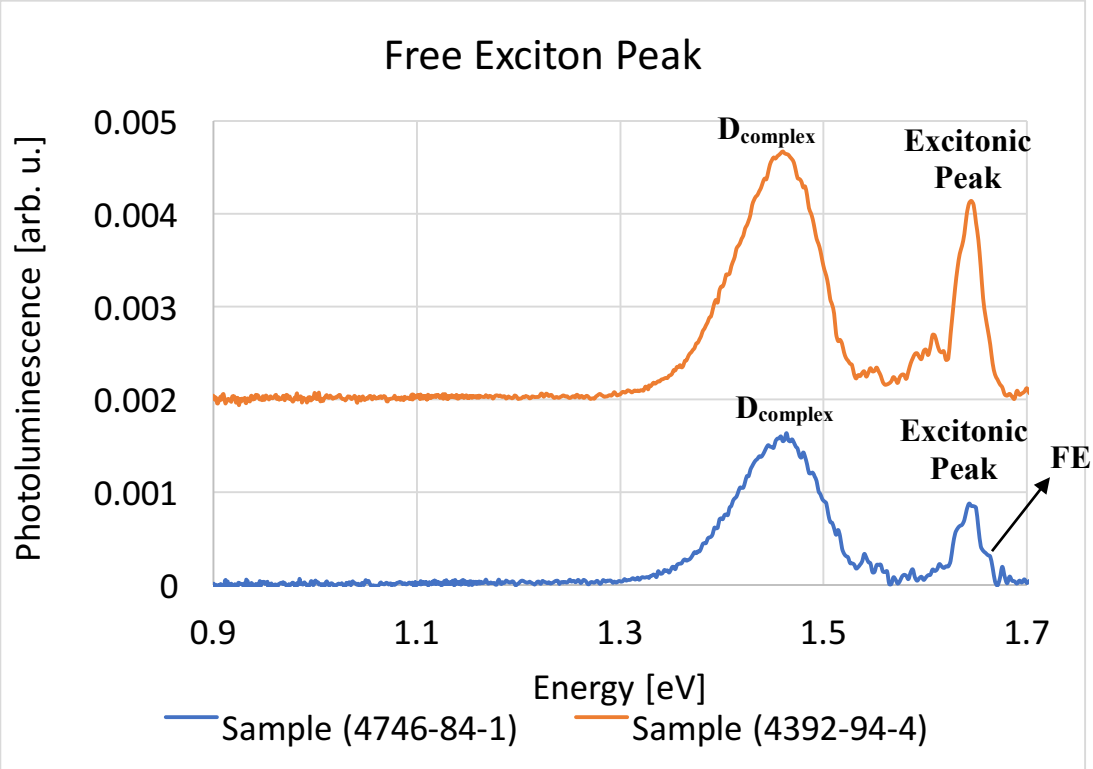

Figure 36 - Low temperature (9K) PL spectra of samples (4746-84-1) and (4392-94-4) excited by a green laser using a resolution of 22.5 meV.

4.10 (D, X) and (A, X) peaks

The excitonic PL lines are very sensitive to various defects in semiconductors. Excitonic signatures in the low temperature PL spectra of semiconductors of high optical quality usually appear as the intense lines caused by the excitons bound to donor and acceptor centers. In this case the energy levels of the bound excitons move down from the free exciton level by the amount equal to their energy binding. This energy depends on the

nature of the impurities or intrinsic defects. Therefore, the energy position of the bound excitons may let us determine the nature of defects participating in the formation of the excitonic complexes. Determination of the type of a CZT material, whether it is n-type or p-type, depends on the type of the dominant electrical carrier (electrons for n-type or holes for p-type) and thus, it depends on the impurity content and stoichiometry of the CZT material. Further, the material can be defined as n- or p-type according to the excess of either Cd + Zn or Te, respectively. Thus, we may define p-type CZT as material whose atomic ratio r=Te/(Cd+Zn) is >1. P-type CZT is also defined by the prominence of the acceptor bound exciton recombination over the donor bound exciton photoluminescence spectrum. However, when r < 1 and the donor bound exciton is significantly larger than the acceptor bound exciton, we may refer to the CZT material as n-type [70]. Redlen samples are p-type.

In semiconductors, free excitons can migrate in the crystals. Accordingly, some defects in the crystals can bind free excitons and form bound excitons. For CdZnTe, a higher (D, X) intensity may imply that a larger portion of the doped indium acts as hydrogenic shallow donors by substituting Cd sites. A broadening of (D, X) peak might be caused by macroscopic differences in composition, microscopic alloy fluctuations, and defects. Additionally, Cl on a Te site is a shallow donor with a binding energy of 14 meV, and they might contribute in the donor bound exciton peak (D, X) in the PL [22]. Further, (D, X) peak intensity might be partially attributed to Te antisites (Te_{Cd}) defects [84]. On the other side, Cu is known to be one of the common residual impurities in CdZnTe, and (A, X) may be assigned to Cu residuals in CZT [63, 67].

A broadening in (A, X) peak indicates that, (A, X) is a complex consisting of the overlapping emission of several acceptor bound exciton complexes. Excitons might be bound to different acceptors. (A, X) peak may be attributed to Cd vacancies and shallow acceptors such as Na_{Cd} [60]. Thus, a lower (A, X) peak intensity may be attributed to the compensation between indium donors and the Cd vacancy acceptors that forms A-centers.

The relative emission between (A, X) and (D, X) peaks depends on the defects in the crystal. I(D, X)/I(A, X) ratio may be beneficial as it relates to the prevalence of the concentration of shallow donors over that of shallow acceptors throughout a cross-section of the sample, and it can be an indicator to the density of acceptor levels. Figure 37 shows that in sample (4746-73-3), the intensity of (A, X) outweighs (D, X), which signifies a growth of the shallow acceptors compared to the shallow donors. However, in sample (4272-98-6) the donor-bound exciton (D, X) luminescence is stronger, indicating a smaller proportion of shallow acceptor states in the sample [71].

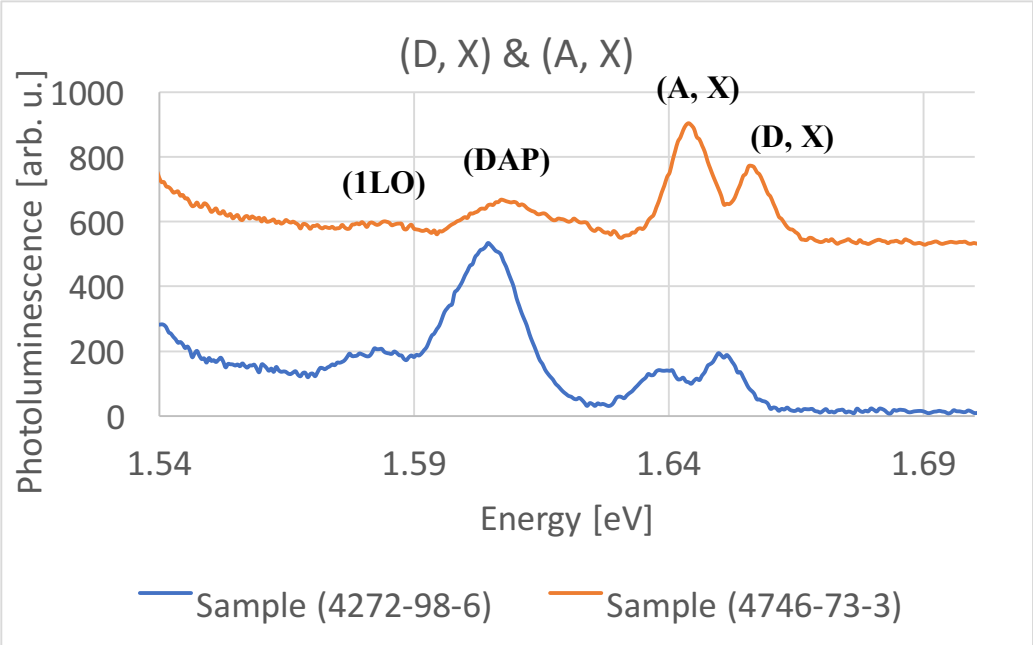

Figure 37 - Low temperature (9K) PL near band edge region spectra of samples (4272-98-6) and (4746-73-3) excited by a blue laser using a resolution of 5.6 meV.

4.11 A, B Faces of CZT

In this experiment, faces A and B of CZT sample (4272-98-1) are investigated and compared. Face B is the cathode of the detector and its surface is occupied by Te atoms. Face A is the anode of the detector and its surface is occupied by Cd atoms [12]. Both surfaces are illuminated by a 60-mW excitation power using the blue laser. The illuminated spots are opposite to each other. Figure 38 plots the PL near band edge region spectra of both faces. It is evident from the figure that DAP peak has a higher emission intensity in the spectrum of face A. Therefore, there might be a higher concentration of impurities and defects such as Li and Na near surface A. Additionally, the figure illustrates that, in face B spectrum the intensity of (A, X) outweighs (D, X), which signifies a growth of the shallow acceptors (Cu residuals and Cd vacancies) compared to the shallow donors. However, in face A spectrum the donor-bound exciton (D, X) luminescence is significantly stronger. Therefore, there might be a larger quantity of In donors near surface A. Figure 39 compares the PL spectra of faces B and A. The figure is plotted in log scale to show the weak 1.1eV deep level peak. The 1.1eV peak is stronger in the spectrum of face A. The 1.1eV broad luminescence band is believed to be attributed to Te vacancies [43, 61]. Thus, there might be a larger proportion of Te vacancies near surface A. Moreover, it is worth noting that the as received surfaces could have different oxides and the surface states might be different, which might result in variations in the relative intensity between the PL peaks of the two surfaces. A summary of intensity ratios between the peaks in the spectra of both faces is listed in Table 6.

Table 6 - Summary of the intensity ratios between the peaks in the spectra of both faces.

Surface	I(DAP)/ I(D, X)	I(A, X)/ I(D, X)	$I(D_{complex})$/ I(Exciton)	I(1.1eV Peak)/ I(Exciton)
Surface B	1.56	1.4	4.5	0.04
Surface A	1.4	0.5	7.57	0.23

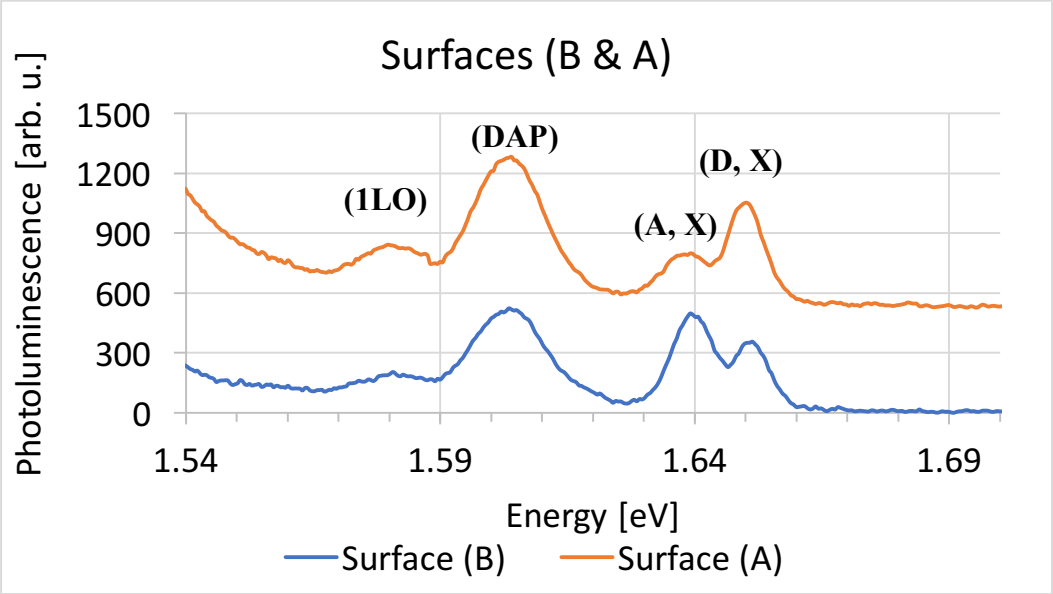

Figure 38 - Low temperature (9K) PL near band edge region spectra for faces (B and A) of sample (4272-98-1) excited by a blue laser using a resolution of 5.6 meV.

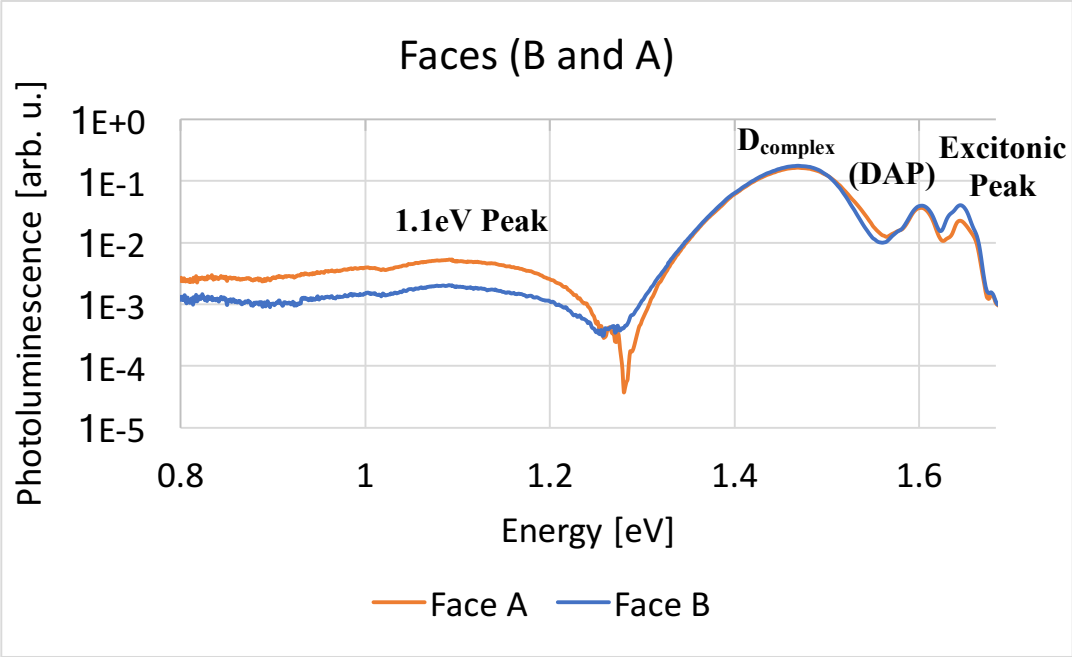

Figure 39 - Low temperature (9K) PL spectra for faces (B and A) of sample (4272-98-1) excited by a blue laser using a resolution of 23 meV.

4.12 PL study of etched and passivated surfaces of CZT sample

Photoluminescence is a useful technique for studying surface recombination in semiconductor materials. Te enrichment introduced by etching with Br-MeOH results in high surface leakage current. Surface passivation treatment can be used in CZT detectors production to create tellurium oxide TeO_2 on the detector surface and to mitigate the negative effect of the surface non-bound Te atoms on the performance of a device. We use low temperature PL to investigate the effect of surface oxidation on sample (1527-121-9) by hydrogen peroxide solution passivation. The sample was first etched in 1% Br-MeOH followed by methanol rinsing. Then, PL measurements were performed on the etched surface. The sample was then oxidized in H_20_2 aqueous solution with a 15% concentration for 8 minutes. PL measurements were carried out on the passivated surface [74].

PL spectra at a low temperature of 9K for the Br-MeOH etched and the H_2O_2 passivated surfaces of sample (1527-121-9) illuminated with green, and UV light, are shown in Figures 40, 41, and 42, respectively. $D_{complex}$ is the peak associated with crystal imperfection and impurity levels. I(bound exciton)/I($D_{complex}$) intensity ratio is 0.38 for the passivated surface, and 0.19 for the etched surface. The surface passivation effect of CZT detector can be seen clearly in Figures 40 and 41, where the passivated surface shows a lower level of traps in the near surface region evidenced by the larger I(bound exciton)/I($D_{complex}$) intensity ratio compared to the etched surface. For UV excitation, Figure 42 shows that, a peak centered at 1.75 eV appeared in the passivated surface PL spectrum, however it was barely detectable in the etched surface PL spectrum. This 1.75 eV peak is possibly due to the surface layer on the passivated sample, and may further be used as an indicator of the surface oxide thickness on the CZT samples. The oxide species on the CZT surface were previously identified as mainly TeO_2 [74]. Other possibilities are $CdTeO_3$ and $ZnTeO_3$ [74].

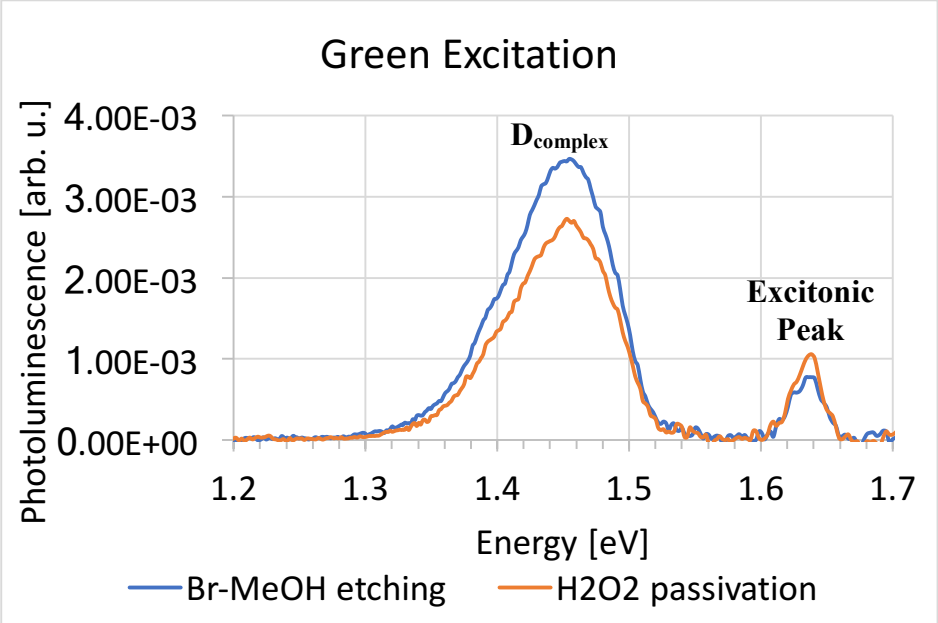

Figure 40 - Low temperature (9K) PL spectra for the Br-MeOH etched and the H_2O_2 passivated surfaces of sample (1527-121-9) excited by a green laser using a resolution of 23 meV.

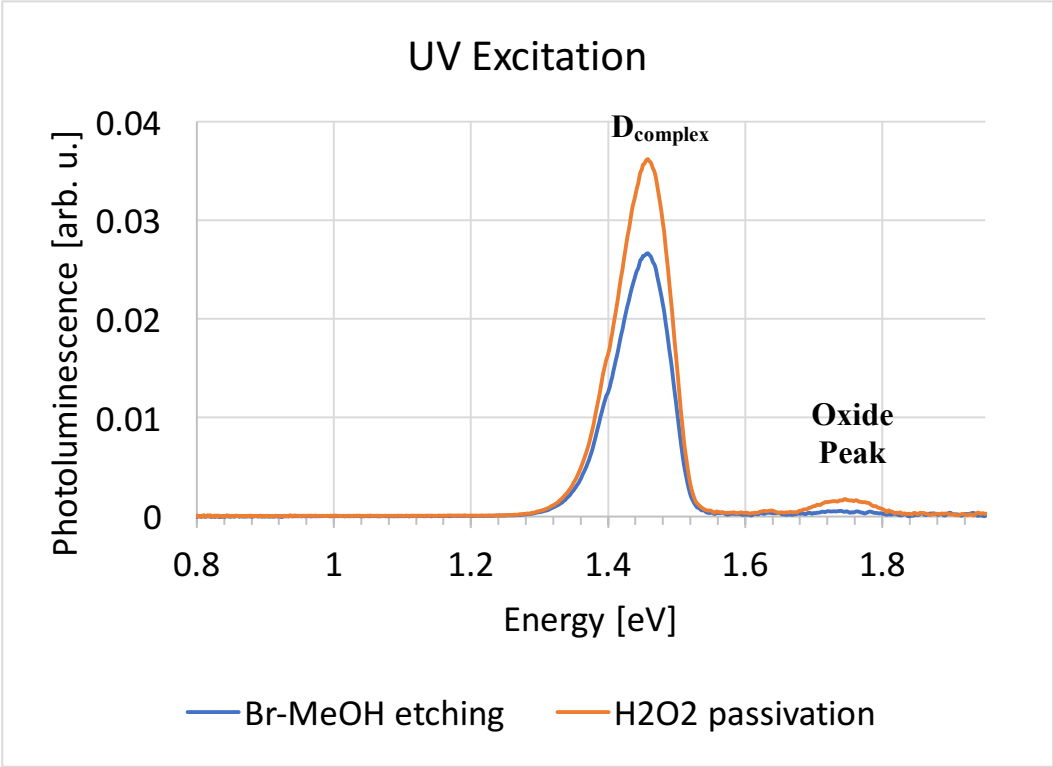

Figure 41 - Low temperature (9K) PL spectra for the Br-MeOH etched and the H_2O_2 passivated surfaces of sample (1527-121-9) excited by a UV LED using a resolution of 23 meV.

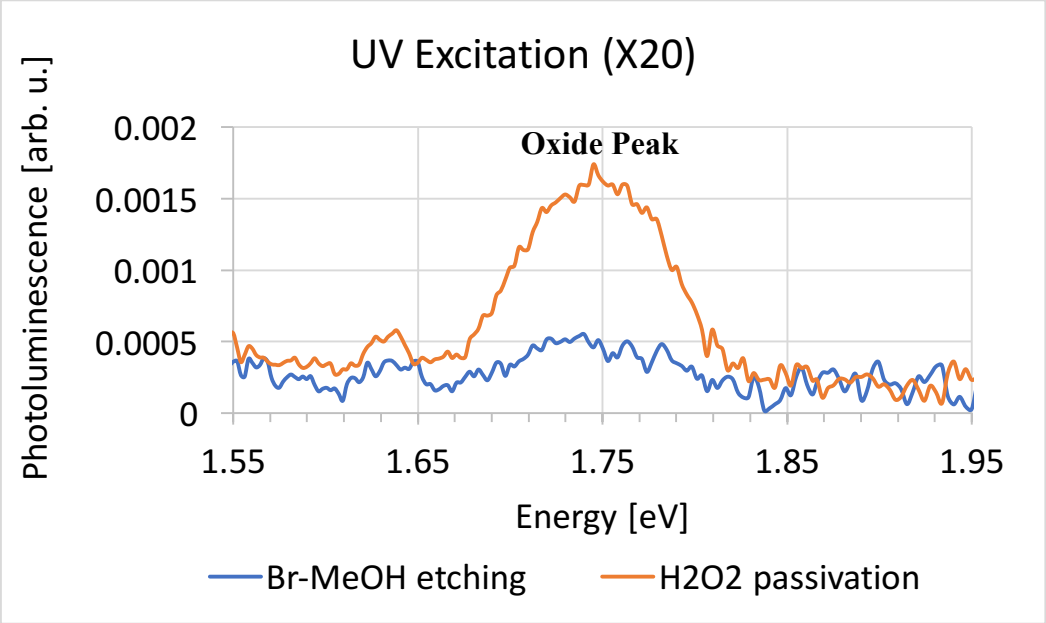

Figure 42 - X20 zoomed 9K PL spectra for the Br-MeOH etched and the H_2O_2 passivated surfaces of sample (1527-121-9) excited by a UV LED using a resolution of 23 meV.

4.13 Excitation wavelength dependence

From the photoluminescence spectra, we can obtain information about the defects' origin and their related concentration in the studied crystal. Using different excitation wavelengths, we can obtain the information about the material quality at different depths from the sample surface. In this experiment, we excite sample $Cd_{0.96}Zn_{0.04}Te$ using three different sources: a UV LED with a penetration depth of 17nm, a blue laser with a penetration depth of 74nm, and a green laser with a penetration depth of 128nm. Each source provides certain information about the sample because of their varied characteristics [77]. It is worth noting that the penetration depth is computed for CdTe, and since the penetration depth depends on the zinc fraction x, the CZT penetration will be bigger.

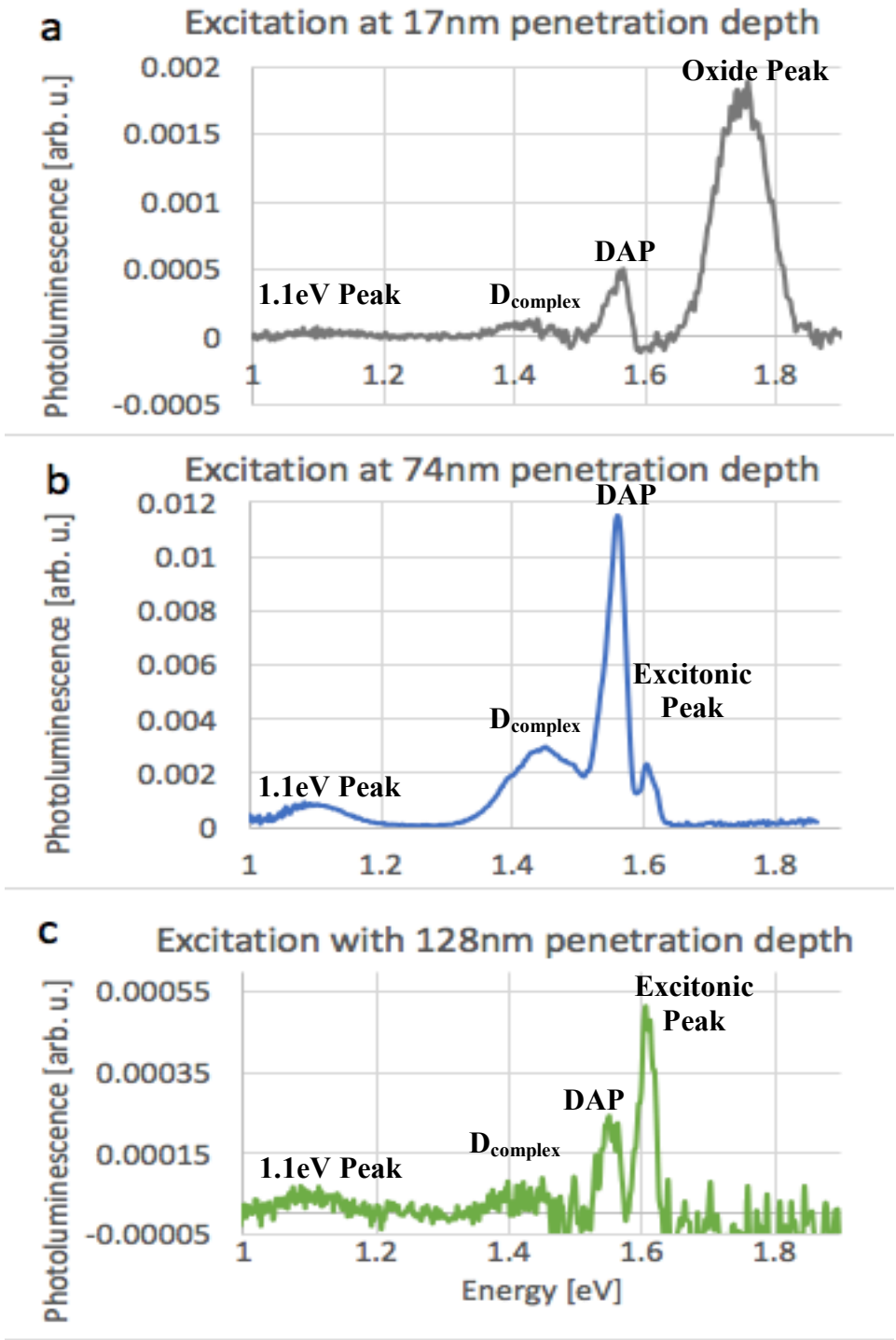

Figure 43 - Low temperature (9K) PL spectra, using a resolution of 23 meV, of sample $Cd_{0.96}Zn_{0.04}Te$ excited by: (a) a UV LED with a penetration depth of 17nm, (b) a blue laser with a penetration depth of 74nm, (c) a green laser with a penetration depth of 128nm.

Figure 43 compares the PL spectra of sample $Cd_{0.96}Zn_{0.04}Te$ excited by the three different sources, and provides information about the defects existing at three different depths and excitation power inside the sample. A peak centered at 1.75 eV appears only in UV excitation spectrum, and it may be attributed to the oxide layer on the CZT surface. The bound exciton peak does not exist in the UV excitation spectrum. However, it appears with the blue excitation, and it further dominates the green illumination spectrum. There might be a high concentration of the defects related to the bound excitons near a 128nm depth. The DAP peak is relatively strong in all excitation cases, and it dominates the blue excitation spectrum. Impurities related to DAP recombinations, such as Li and Na, probably exist near the surface and in the bulk of the sample. We use the $I(D_{complex})/I(DAP)$ and I(1.1eV peak)/I(DAP) intensity ratios as indicators of the A-center related defects concentration, and the Te vacancies concentration, respectively, near the three different depths in the sample. $I(D_{complex})/I(DAP)$ ratio increases from 0.20 near the surface to 0.27 near a 74nm depth, and it slightly reduces to 0.26 near a 128nm depth inside the sample. On the other hand, I(1.1eV peak)/I(DAP) ratio slightly decreases from 0.075 near the surface to 0.072 at a 74nm depth, and it noticeably rises to 0.22 near a 128nm depth inside the sample. The intensity ration of $I(D_{complex})/I(1.1eV\ peak)$ can also be used to relate the intensity change of $D_{complex}$ peak and 1.1eV peak at different depths inside the sample. The ratio is 2.7 near the surface, and it increases to 3.7 near the 74nm depth, however it decreases to 1.2 near the 128nm depth. A summary of intensity ratios between the defect related peaks at all depths is listed in Table 7. Moreover, it is worth noting that the three excitation sources have different instantaneous powers, thus the variations in the relative intensity among the peaks might be due to the instantaneous power differences.

Table 7 - Summary of intensity ratios between the defect related peaks at different depths inside the $Cd_{0.96}Zn_{0.04}Te$ sample.

Excitation	Photon Energy (eV)	Penetration Depth (nm)	$I(D_{complex})$/ I(DAP)	I(1.1eV Peak)/ I(DAP)	$I(D_{complex})$/ I(1.1eV Peak)
UV LED	3.4	17	0.20	0.075	2.7
Blue Laser	2.54	74	0.27	0.072	3.7
Green Laser	2.33	128	0.26	0.22	1.2

4.14 Excitation power dependence and Temperature dependence

It is stated in the literature that the PL spectra is dependent on the incident light power [78-79]. In order to investigate the dependence of the CZT PL on the excitation power, we study the behavior of the PL spectra of sample (4746-84-1) as the excitation power is varied from 15mW to 150 mW with a step of 15mW. Figure 45 gives a typical plot of the PL intensity of (D, X) and (A, X), DAP, $D_{complex}$ peaks vs. excitation power. It is evident from the plot that, the intensity of the peaks increases with increasing excitation power, and the (D, X) peak eventually saturates at high excitation power. The drop that occurs to the intensity of both (A, X) and DAP peaks at higher excitation powers is possibly because at high illumination power the sample heats up, and thus the temperature of the sample increases [80]. This temperature increase also results in a shift of the (D, X) peak towards lower energy, as shown in Figure 44 that plots the low temperature PL near band edge region spectra of sample (4746-84-1). Figure 46 plots (D, X) peak position as a function of excitation power.

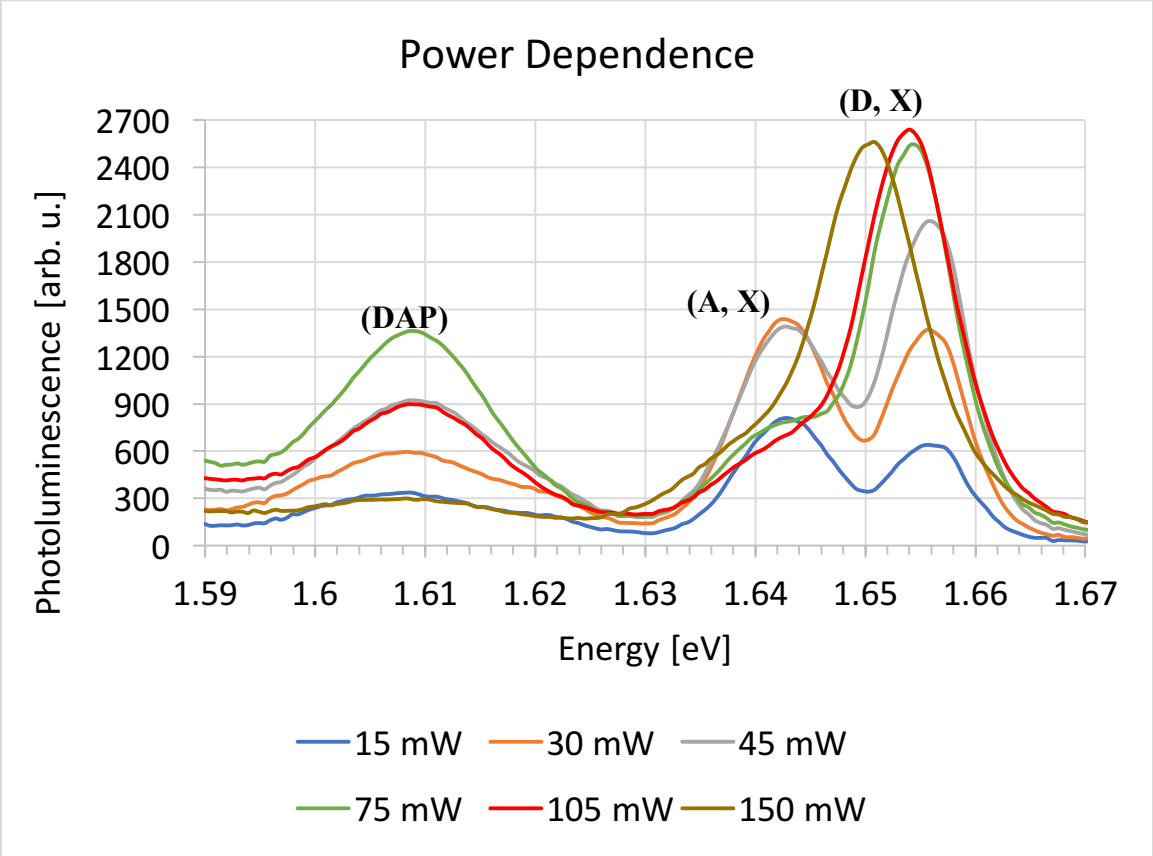

Figure 44 - Power dependent PL spectra of sample (4746-84-1) excited by a blue laser using a resolution of 5.6 meV.

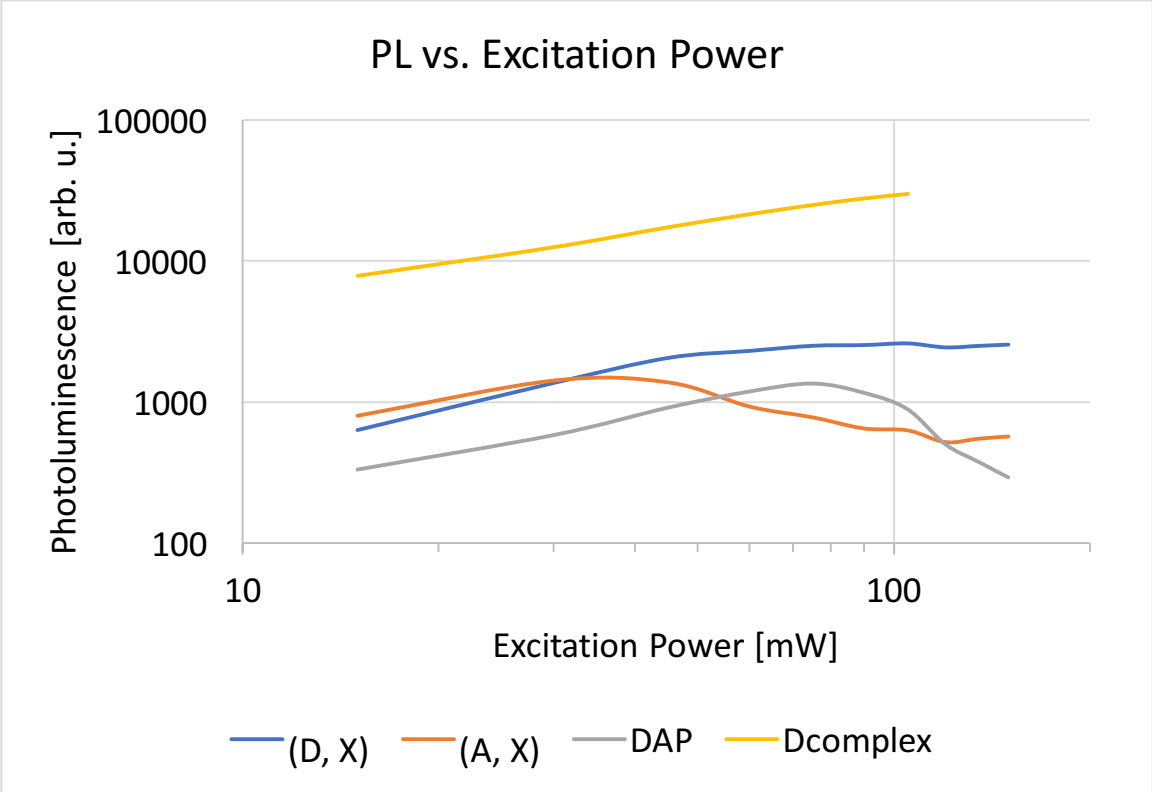

Figure 45 - Power dependence of the intensity for (D, X), (A, X), DAP, and $D_{complex}$ peaks in sample (4746-84-1) excited by a blue laser.

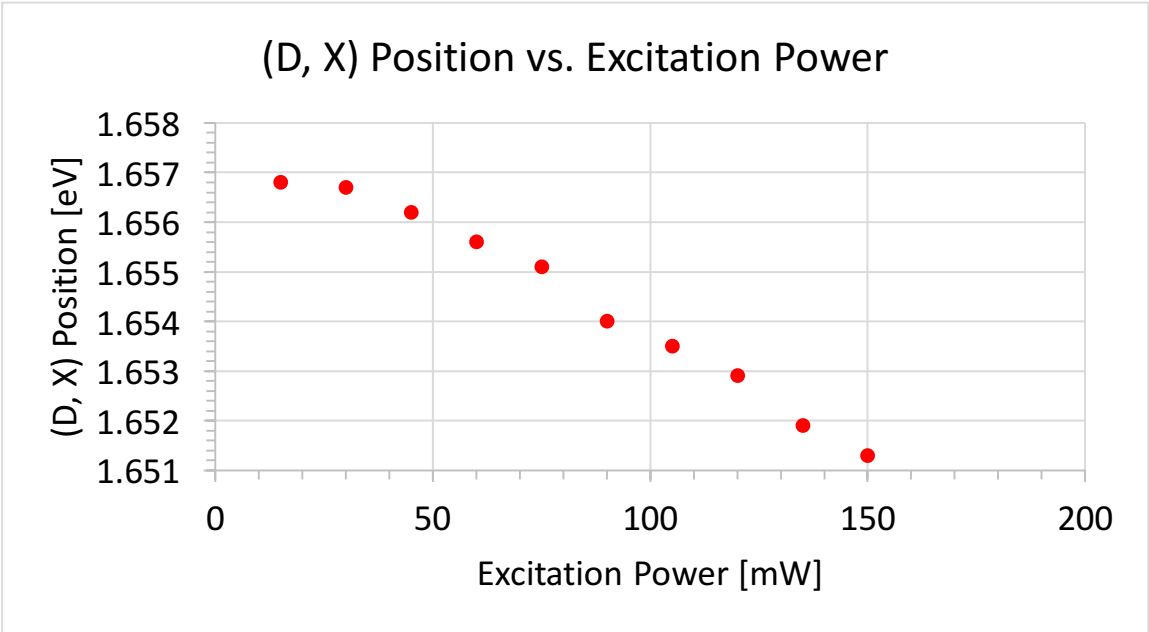

Figure 46 - (D, X) peak position as a function of excitation power.

To understand the phenomena better, and further illustrate the temperature dependence of the CZT sample, we study the transitions of PL spectra in the temperature range from 9 to 100 K. Figure 47 shows temperature dependence of the PL spectra of sample (4746-84-1). As shown in the figure, the intensity of (D, X) peak reduces gradually when the temperature is raised up from 9 to 100 K, however, (A, X) peak disappears rapidly. Figure 48 plots the PL intensity of (D, X) as a function of temperature. The behavior can be explained by thermal quenching phenomenon which is due to thermal excited non-radiative transitions and thermal dissociation of bound exciton states. In addition, it is also noticed that (D, X) peak tends to shift towards lower energy with increasing temperature. The shift of (D, X) peak is due to the shrinkage of the bandgap energy with increasing temperature [80]. Using figure 46 and 47, we estimated the temperature of the sample when exposed to a 150-mW power of the blue laser to be 40 K. Figure 49 plots the intensity of (D, X) peak in log scale versus inverse temperature. To calculate the activation energy, equation 4.3 gives the standard fitting formula.

$$I(T) = A/[1 + \mathrm{B}\exp(-\frac{U}{KT})] \tag{4.3}$$

where I(T) represents the PL intensity, A is the intensity at absolute zero temperature, B is a constant, T is the temperature, k is Boltzmann constant, and U is the activation energy. Using this expression and figure 49, the activation energy is calculated to be roughly 25 meV.

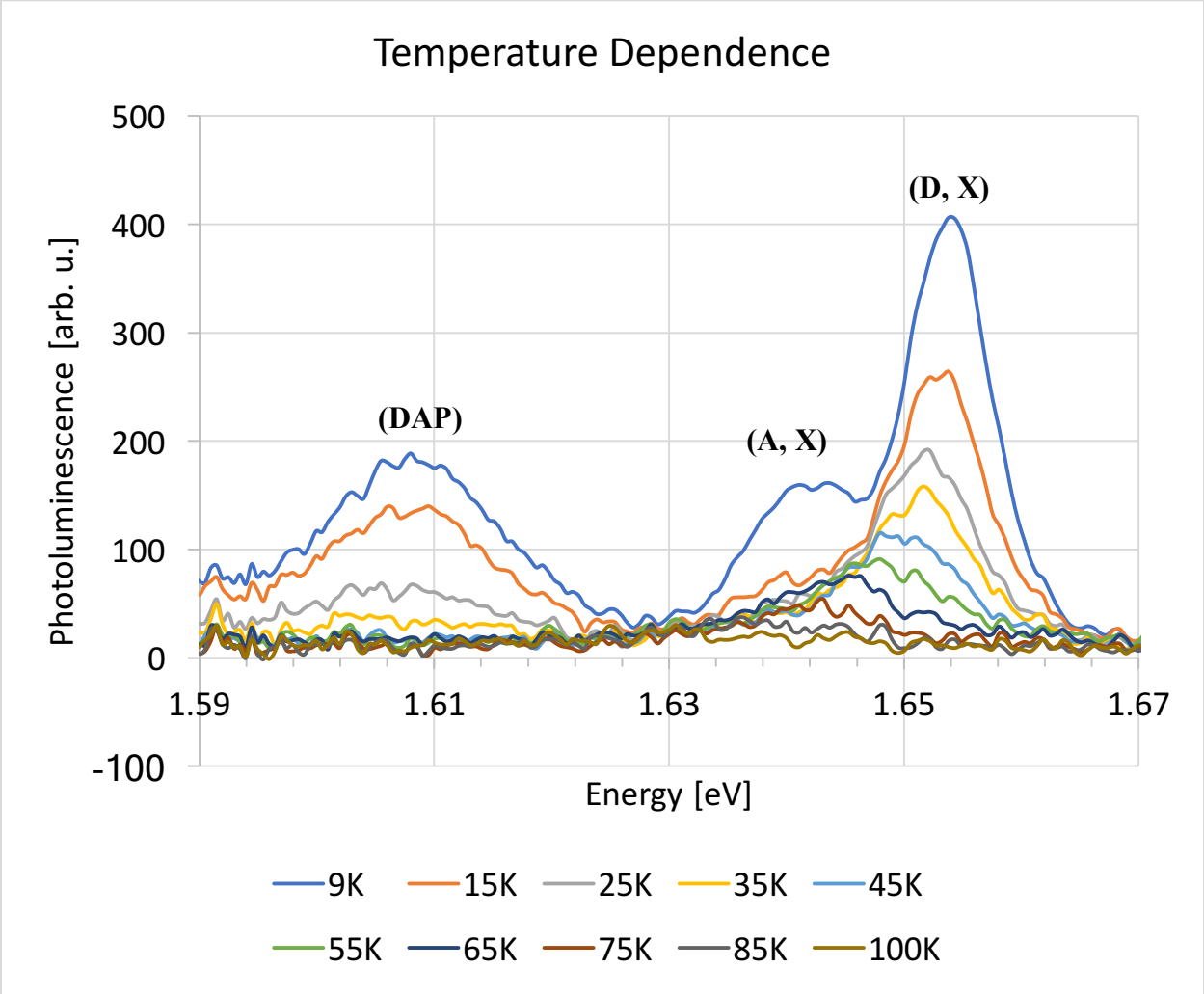

Figure 47 - Temperature dependent PL spectra of sample (4746-84-1) excited by a blue laser using a resolution of 5.6 meV.

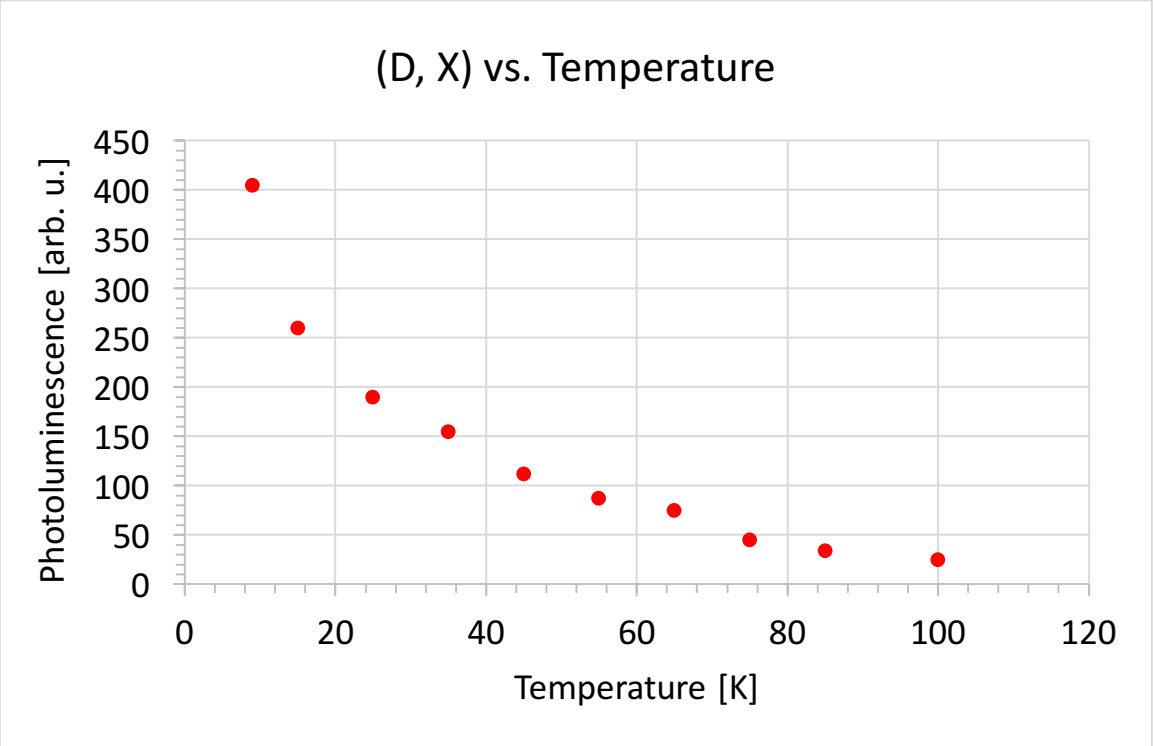

Figure 48 - PL intensity of (D, X) as a function of temperature.

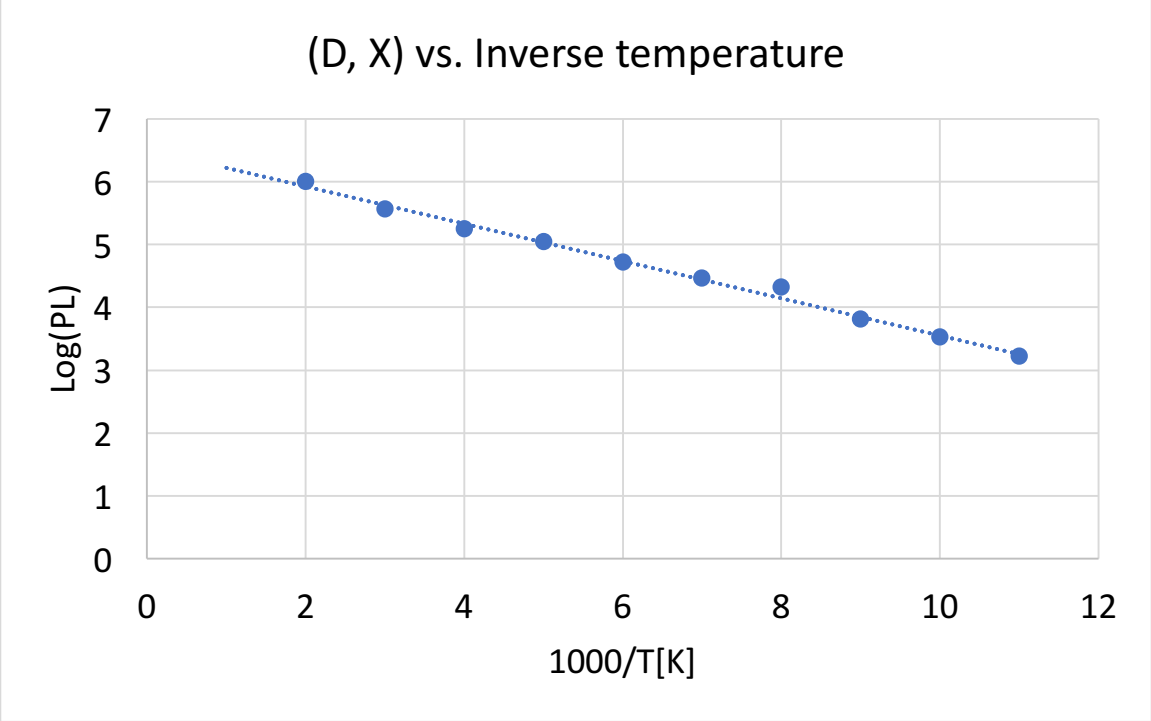

Figure 49 - Temperature dependence of (D, X) peak.

5 Conclusion

In this work, photoluminescence spectroscopy has been applied to study a number of different CZT samples provided by Redlen. Besides the values of the resistivity and stability of the samples, no further information about the samples was provided by Redlen due to confidentiality reasons. The samples had different resistivity and stability and further investigations on the differences among them were needed. No correlations between resistivity, stability, and PL peaks intensity have been found. Nevertheless, PL has been used to further study the samples and understand the features of their defects and impurities. We have analyzed the PL emission peaks to understand their origin. We have addressed the presence, and identified the type of the defects and impurities in the CZT samples, and studied their signatures in the PL spectra. Further, we have compared the PL spectra of different CZT samples, and investigated the differences among them. We hope that our findings from this project could provide useful feedback to improve the crystal growth and detector fabrication processes for higher performance of CZT radiation detectors.

The low temperature (9K) PL spectra of different samples have been analyzed. The uniformity of a CZT sample has been examined. Additionally, the PL spectra of $Cd_{0.9}Zn_{0.1}Te$ and $Cd_{0.96}Zn_{0.04}Te$ have been analyzed and compared. Comparisons among the samples in terms of: the zinc molar concentration, the intensity ratio between the deep level defect and the bound exciton peaks, the existence of DAP peak, the intensity ratio between the DAP and the donor bound exciton peaks, the presence of the free exciton peak, and the intensity ratio between the donor and acceptor bound excitons peaks have been done. Further, excitation power dependence and temperature dependence have been

investigated. Moreover, the defects and impurities near the surfaces of the two faces (B and A) of sample (4272-98-1) have been investigated and compared. We have also used different excitation wavelengths to obtain more information about the defects existing at different depths from the surface of $Cd_{0.96}Zn_{0.04}Te$ sample.

In addition, PL technique has been used to explore the role of the surface passivation treatment in improving the spectrometric performance of the CZT detectors. The surface of sample (1527-121-9) has been etched with Br-MeOH, and then chemically oxidized in H_20_2 aqueous solution. PL measurements have been carried out on the Br-MeOH etched and the H_2O_2 passivated surfaces of the sample, and the PL spectra of the etched and passivated surfaces have been compared. A peak at 1.75 eV has appeared in the PL spectrum of the oxidized surface when excited by UV light. This peak has been attributed to the oxide layer on the passivated surface.

6 Suggestions for future work

Applications of CZT detectors, such as early cancer detection and homeland security, reveal that, improving this technology will have great benefits to humanity. The performance of CZT x-ray and gamma-ray spectrometers is often limited by their surface leakage currents. Thus, reducing surface leakage currents by surface passivation is very important for the fabrication of CZT detectors. Therefore, further investigations could be done on the surface oxide layer using PL method, in an effort to optimize the surface processing and thereby improve CZT detector performance. Interesting experiments that could be done in the future are: Wet and dry ozone surface passivation, XPS measurements of the surface oxide composition and thickness. Additionally, the PL 1.75 eV emission can be further used as an indicator of the surface oxide layer thickness on CZT samples. Further, other surface passivation including wide bandgap II-VI semiconductors such as ZnSe could be investigated.

Bibliography

[1] Radiation Detection and Measurement, G. F. Knoll, John Wiley & Sons, Ltd (2000)

[2] High-purity germanium crystal growing, W.L. Hansen, Nuclear Instruments and Methods, 94, 377-380 (1971)

[3] Compound Semiconductor Radiation Detectors, A. Owens, A. Peacock, Nuclear Instruments and Methods in Physics Research A, 531, 18-37 (2004)

[4] Semiconductors for Room Temperature Nuclear Applications, T. E. Schlesinger, R. B. James, Academic Press, New York, Chapter 9, 335-372 (1995)

[5] CdTe and CdZnTe gamma ray detectors for medical and industrial imaging systems, Y. Eisen, A. Shor, and I. Mardor, Nuclear Instruments and Methods in Physics Research Section A: Accelerators, Spectrometers, Detectors and Associated Equipment, 428, 158-170 (1999)

[6] Role of Zinc in CdZnTe Radiation Detectors, M. Chu, S. Terteriam, D. Ting, IEEE Transactions on Nuclear Science, 51, 2405-2411 (2004)

[7] Recent Developements in CdZnTe Gamma Ray Detector Technology, J. F. Butler, F. P. Doty, C. Lingren, SPIE, 1734, 131-138 (1992)

[8] Distribution and Genesis of Inclusions in CdTe and (Cd,Zn)Te Single Crystals Grown by the Bridgman Method and by the Travelling Heater Method, P. Rudolph, A. Engel, I. Schentke, and A. Grochocki, Journal of Crystal Growth, 147, 297-304 (1995)

[9] Defects in CZT crystals and their relationship to gamma-ray detector performance, Burger, K. Chattopadhyay, H. Chen, X. Ma, J. O. Ndap, M. Schieber, T. E. Schlesinger, H. W. Yao, J. Erickson, R. B. James, Nuclear Instruments and Methods in Physics Research Section A: Accelerators, Spectrometers, Detectors and Associated Equipment, 448, 586-590, (2000)

[10] Photoluminescence as a diagnostic of semiconductors, P. J. Dean, Progress in Crystal Growth and Characterization, 5, 89-174 (1982)

[11] Effects of surface processing on the response of CZT gamma detectors: Studies with a collimated synchrotron X-ray beam, A. E. Bolotnikov, G. S. Camarda, Y. Cui, S. Babalola, A. Burger, and R. B. James, J. Electron. Mater, 37, 1356-1361 (2008)

[12] Seed-Free Growth of (111) Oriented CdTe and CdZnTe Crystals by Solid State Recrystallization, S. Hassani, A. Lusson, A. Thomson-Carli, and R. Triboulet, Journal of Crystal Growth, 249, 121-127 (2003)

[13] Characterisation of Surface Treated CdZnTe and Thin Film CdTe based Devices, S. Babar, PhD thesis, University of Surrey (2016)

[14] Sub-keV resolution detection with Cd1-xZnxTe detectors, J. F. Butler, B. A. Apotovsky, A. Niemela, H. Sipila, International Society for Optics and Photonics, 241, 121-127 (1993)

[15] Mass Spectrometric Study of the CdTe-ZnTe System, A.S. Alikhanian, V.N. Guskov, A.M. Natarovsky, J.H. Greenberg, M. Fiederle, and K.W. Benz, Journal of Crystal Growth, 240, 73-79 (2002)

[16] Deep energy levels in CdTe and CdZnTe, A. Cavallini, B. Fraboni, P. Fernandez, and J. Piqueras, J. Appl. Phys, 83, 2121-2125 (1998)

[17] Modification of the luminescence properties of CZT crystals around tellurium inclusions, N. Zambelli, L. Marchini, G. Benassi, D. Calestani, and A. Zappettini, IEEE Trans. Nucl. Sci, 59, 1526–1530 (2012)

[18] Review of the Shockley–Ramo theorem and its application in semiconductor gamma-ray detectors, He, Zhong, Nuclear Instruments and Methods in Physics Research Section A: Accelerators, Spectrometers, Detectors and Associated Equipment, 463, 250-267 (2001)

[19] Growth of CdZnTe single crystals for radiation detectors, A. A. Melnikov, Journal of crystal growth, 197, 666-669 (1999)

[20] Characterization of Travelling Heater Method (THM) Grown CdZnTe Crystals, H. Chen, S. Awadalla, J. Mackenzie, R. Redden, G. Bindley, A. E. Bolotnikov, G. S. Camarda, G. Carini, R. B. James, IEEE Transactions on Nuclear Science, 54, 811-816 (2007)

[21] $Cd_{1-x}Zn_xTe$ gamma ray detectors, J. F. Butler, C. L. Lingren, and F. P. Doty, IEEE Transactions on Nuclear Science, 39, 605–609 (1992)

[22] Cadmium zinc telluride and its use as a nuclear radiation detector material, T. E. Schlesinger, J. E. Toney, H. Yoon, E. Y. Lee, B. A. Brunett, L. Franks, R. B. James, Material Science and Engineering, 32, 103-189 (2001)

[23] Introduction to Semiconductor Optics, N. Peyghambarian, S.W. Koch, and A. Msyrowicz, Prentice-Hall, Englewood Cliffs (1993)

[24] Fundamentals of Semiconductor Devices, E. S. Yang, McGraw Hill Book Company (1978)

[25] Optical properties of CdTe/$Cd_{1-x}Zn_xTe$ strained-layer single quantum wells, L. Tiesheng, H. J. Lozykowski, J. L. Reno, Physical Review B, 46.11, 6961-6968 (1992)

[26] The Effect of Crystal Defects on the Performance of High-flux CZT X-ray Detectors, N. Sadeghi, MSc thesis, University of Victoria (2015)

[27] Compound semiconductor radiation detectors, A. Peacock, Nuclear Instruments and Methods in Physics Research A, 531, 18-37 (2004)

[28] Band gap energy determination by photoacoustic absorption and optical analysis of $Cd_{1-x}Zn_xTe$ for low zinc concentrations, J. J. Prias-Barragan, L. Tirado-Mejia, H. Ariza-Calderon, L. Banos, J. J. Perez-Bueno, M. E. Rodriguez, Journal of Crystal Growth, 286, 279–283 (2006)

[29] Fundamentals of Semiconductors, E. E. Haller, P. Y. Yu, M. Carlona, Springer Verlag, New York (1996)

[30] Effects of In doping on the properties of CdZnTe single crystals, Y. Ge, Journal of crystal growth, 283.3, 431-437 (2005)

[31] An analysis of point defects induced by In, Al, Ni, and Sn dopants in Bridgman-grown CdZnTe detectors and their influence on trapping of charge carriers, R. Gul, U. N. Roy, R. B. James, JOURNAL OF APPLIED PHYSICS, 121, 115701 (2017)

[32] Accurate measurement of electrical bulk resistivity and surface leakage of CdZnTe radiation detector crystals, M. Prokesch, C. Szeles, Journal of Applied Physics, 100, 014503 (2006)

[33] Study of polarization phenomena in n-type CdZnTe, H. Elhadidy, Journal of Physics D: Applied Physics, 47.5, 055104 (2014)

[34] Radiation detection, W. H. Tait, Butterworths (1980)

[35] Physics and Radiobiology of Nuclear Medicine, G. B. Saha, Springer New York (2013)

[36] Radiation detection and measurement, F. Glenn, third edition John Wiley & Sons (1989)

[37] Interaction of Radiation with Matter, H. Nikjoo, S. Uehara, D. Emfietzoglou, Taylor & Francis (2012)

[38] Introduction to nuclear physics, W. N. Cottingham, D. A. Greenwood, Cambridge (2002)

[39] Electric field studies on Cadmium Zinc Telluride (CdZnTe) Materials, G. I. Prekas, PhD thesis, University of Surrey (2010).

[40] Pixel detectors and electronics for high energy radiation imaging, M. A. Abdalla, MSc thesis, The Royal institute of Technology (2001)

[41] Semiconductor light source for optical coherence tomography, S. Webster, MSc thesis, University of British Columbia (2004)

[42] Photoluminescence and X-ray Diffraction Analysis of Cadmium Zinc Telluride Crystals, R. Jamnejad, MSc thesis, University of Victoria (2014)

[43] Photoluminescence spectroscopy of semi-insulating CdZnTe and its correlation to resistivity and photoconductivity, J. Zazvorka, J. Franc, P. Hlidek, R. Grill, J. Lumin, 143, 382–387 (2013)

[44] Photoconductivity, photoluminescence and charge collection in semiinsulating CdTe and CdZnTe, J. Zázvorka, PhD thesis, Charles University (2016)

[45] Optical investigations of defects in $Cd_{1-x}Zn_xTe$, W. Stadler, D. M. Hofmann, H. C. Alt, T. Muschik, B. K. Meyer, E. Weigel, G. Muller-Vogt, M. Salk, E. Rupp, and K. W. Benz, Phys. Rev. B, 51, 10619–10630 (1995)

[46] Infuence of Deep Levels on Charge Transport in CdTe and CdZnTe, V. Dedic, PhD thesis, Charles University (2014)

[47] Photoluminescence Study of Cadmium Zinc Telluride, S. Jain, MSc thesis, West Virginia University (2001)

[48] The study on the surface state of CdZnTe (1 1 0) surface, G. Zha, W. Jie, Q. Li, D. Zeng, G. Yang, X. Bai, T. Wang, W. Zhang, F. Xu, Applied Surface Science, 252, 8421–8423 (2006)

[49] Defect Characterization in 4% Cadmium Zinc Telluride Semiconductors, S. Penkova, MSc thesis, University of Victoria, (2018)

[50] Optical and electrical properties of indium-doped $Cd_{0.9}Zn_{0.1}Te$ crystal, Q. Li, W. Jie, L. Fu, T. Wang, G. Yang, X. Bai, G. Zha, Journal of Crystal Growth, 295, 124–128 (2006)

[51] Defects in CdTe and $Cd_{1-x}Zn_xTe$, D. M. Hofmann, W. Stadler, P. Christmann, B. K. Meyer, Nuclear Instruments and Methods in Physics Research A, 380, 117-120 (1996)

[52] Excitation-power dependence of the near-band-edge photoluminescence of semiconductors, T. Schmidt and K. Lischka, PHYSICAL REVIEW B, 45, 16-21 (1992)

[53] Influence of surface treatment of CdZnTe for the radiation detector, S. H. Park, Y. K. Kim, H. S. Kim, IEEE, 342, 1399-1401 (2005)

[54] Optimization of Growth Conditions of $GaAs_{1-x}Bi_x$ Alloys for Laser Applications, V. Yekta, PhD thesis, University of Victoria (2016)

[55] Recombination centers in semiinsulating CdTe, J. Zazvorka, MSc thesis, Charles University (2012)

[56] Photoluminescence-based material quality diagnostics in the manufacturing of CdZnTe ionizing radiation sensors, I. Nasiekaa, N. Kovalenko, V. Kutniy, A. Rybka, D. Nakonechnyj, S. Sulima, V. Strelchuk, Sensors and Actuators A, 203, 176– 180 (2013)

[57] Study on the behaviors of impurities in cadmium zinc telluride, T. Wang, W. Jie, J. Zhang, G. Yang, D. Zeng, Y. Xu, S. Ma, H. Hua, K. He, Journal of Crystal Growth, 304, 313–316, (2007)

[58] Photoluminescence analysis of high-resistivity CdZnTe:In single crystals obtained by annealing, P. Yu, W. Jie, Journal of Luminescence, 146, 382–386 (2014)

[59] Large Volume Imaging Arrays for Gamma-Ray Spectroscopy, Schlesinger, Brunett, Yao, VanScyoc, James, Egarievwe, Chattopadhyay, Ma, Burger, Giles, El-Hanany, Shahar, Tsigelman, Journal of Electronic Materials, 28, 6-11 (1999)

[60] Photoluminescence analysis on the indium doped $Cd_{0.9}Zn_{0.1}Te$ crystal, Q. Li, W. Jie, L. Fu, G. Yang, G. Zha, T. Wang, D. Zeng, JOURNAL OF APPLIED PHYSICS, 100, 013518 (2006)

[61] Low temperature photoluminescence and photoinduced current spectroscopy on CdZnTe grown by high-pressure bridgman technique, K. Cherkaoui, S. Mergui, A. Zumbiehl, M. Hage-Ali, G. Marrakchi, G. Bremond, Mat. Res. Soc. Symp. Proc, 588, 34-39 (1999)

[62] Photoluminescence analysis of $Cd_{1-x}Zn_xTe$ single crystals annealed by a two-step method, G. Yang, W. Jie, Journal of Crystal Growth, 294, 250–253 (2006)

[63] Effects of Cd compensation on the photoluminescence of $Cd_{1-x}Zn_xTe$ single crystals grown by the modified Bridgman method, G. Yang, W.Q. Jie, Appl. Phys. A, 85, 457–460 (2006)

[64] Semiconductor Devices: Physics and Technology, S. M. Sze, John Wiley & Sons (1985)

[65] Comparison of In doped and In, Pb co-doped $Cd_{0.9}Zn_{0.1}Te$, Y. Zaman, W. Jie, T. Wang, L. Xu, Y. He, Y. Xu, G. Zha, R. Guo, X. Fu, Nuclear Instruments and Methods in Physics Research A, 790, 10–13 (2015)

[66] Effects of H_2 Atmosphere Annealing on the Properties of CZT:In Single Crystals, P. F. YU and W. Q. JIE, Journal of ELECTRONIC MATERIALS, 42, 12-17 (2013)

[67] Photoluminescence investigation of CdZnTe:In single crystals annealed in CdZn vapors, G. Yang, W. Jie, J. Mater. Res., 21, 7-11 (2006)

[68] Optical property analysis of high-resistivity CZT:In single crystals before and after annealing, P. Yu, W. Jie, Optical Materials, 36, 1213–1218 (2014)

[69] Study of impurity segregation, crystallinity, and detector performance of melt-grown cadmium zinc telluride crystals, M. Schieber, T. E. Schlesinger, R. B. James, H. Hermon, H. Yoon, M. Goorsky, Journal of Crystal Growth, 237, 2082–2090 (2002)

[70] Homogeneity of CdZnTe detectors, H. Hermon, M. Schieber, R. B. James, J. Lund, A. J. Antolak, D. H. Morse, N. N. P. Kolesnikov, Y. N. Ivanov, M. S. Goorskyd, H. Yoond, J. Toneye, T. E. Schlesinger, nuclear Instruments and Methods in Physics Research A, 410, 100-106, (1998)

[71] Photoluminescence investigation of CdZnTe:In single crystals annealed in CdZn vapors, G. Yang, W. Jie, J. Mater. Res., 21, 7-12 (2006)

[72] Determination of the dependence of the band-gap energy on composition for $Cd_{1-x}Zn_xTe$, J. L. Reno and E. D. Jones, Phys. Rev. B, 45, 1440–1442 (1992)

[73] Determination of energy gap in $Cd_{1-x}Zn_xTe$ (x = 0-0.06), J. Franc, P. Hlıdek, P. Moravec, E. Belas, P. Hoschl, L. Turjanska and R. Varghova, Semicond. Sci. Technol, 15, 561–564 (2000)

[74] Photoluminescence investigation of surface oxidation of $Cd_{0.9}Zn_{0.1}Te$ detectors, H. Chen, M. Hayes, K. Chattopadhyay, K. T. Chen, A. Burge, J. Heffelfinger and R. B. James, Mat. Res. Soc. Symp. Proc., 487, 23-28 (1999)

[75] Improvement in Crystalline Quality of $Cd_{1-x}Zn_xTe$ (x=4%) Crystals Grown in Graphite Crucible, A. K. Garg, M. Srivastava, R. C. Narula, R. K. Bagai, V. Kumar, Journal of Crystal Growth, 260, 148-158 (2004)

[76] J. Mckenzie. PCAMM 2014 Conference at University of Victoria, 2014.

[77] Photoluminescence-based material quality diagnostics in the manufacturing of CdZnTe ionizing radiation sensors, I. Nasiekaa, N. Kovalenko, V. Kutniy, A. Rybka, D. Nakonechnyj, S. Sulima, V. Strelchuk, Sensors and Actuators A, 203, 176– 180 (2013)

[78] Characterization of $Cd_{1-x}Zn_xTe$ Crystals Grown from a Modified Vertical Bridgman Technique, Y. Cui, M. Groza, G. W. Wright, U. N. Roy, A. Burger, L. Li, F. Lu, M. A. Black, and R. B. James, Journal of ELECTRONIC MATERIALS, 35, 6-11 (2006)

[79] Study of surface recombination velocity of $Cd_{1-x}Zn_xTe$ radiation detectors by direct current photoconductivity, Y. Cui, M. Groza, D. Hillman, A. Burger, JOURNAL OF APPLIED PHYSICS, 92, 5-9, (2002)

[80] Temperature dependence of photoluminescence properties of In-doped cadmium zinc telluride, T. Wang, W. Jie, D. Zeng, G. Yang, Y. Xu, W. Liu, and J. Zhang, Journal of materials research, 23, 1389–1392 (2008)

[81] Surface and bulk defects in cadmium zinc telluride and cadmium manganese telluride crystals, O. Babalola, PhD thesis, Vanderbilt University (2009)

[82] Recent Progress in CdTe and CdZnTe Detectors, T. Takahashi, S. Watanabe, IEEE TRANSACTIONS ON NUCLEAR SCIENCE, 48, 50-55, (2001)

[83] Progress in the Development of CdTe and CdZnTe Semiconductor Radiation Detectors for Astrophysical and Medical Applications, S. Sordo, L. Abbene, E. Caroli, A. Mancini, A. Zappettini, and P. Ubertini, Sensors, 9, 3491-3526 (2009)

[84] The relationship between stress and photoluminescence of $Cd_{0.96}Zn_{0.04}Te$ single crystal, D. Zeng, W. Jie, T. Wang, W. Li, J. Zhang, Materials Science and Engineering B, 142, 144–147 (2007)

[85] Small pixel CZT detector for hard X-ray spectroscopy, M. Wilson, R. Cernik, H. Chen, C. Hansson, K. Iniewski, L. Jones, P. Seller, M. Veale, Nuclear Instruments and Methods in Physics Research A, 652, 158-161 (2011)

Appendix A
Details of 9K PL spectra of seven $Cd_{0.9}Zn_{0.1}Te$ samples

A.1 Sample 4912-84-2

A.1.1 Green Excitation

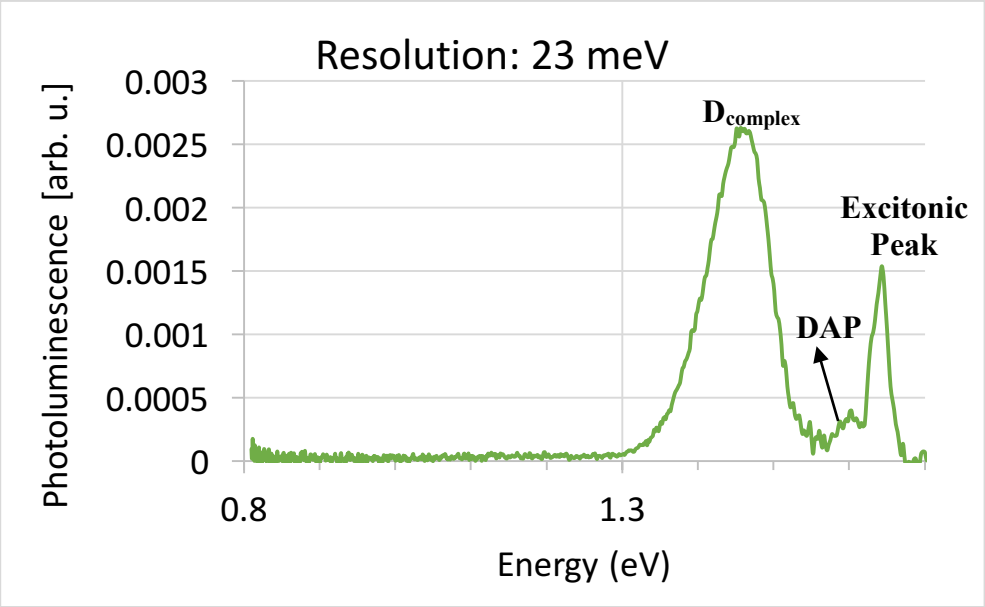

Figure 50 - PL spectrum of sample (4912-84-2) excited by a green at 9K temperature using a resolution of 23 meV.

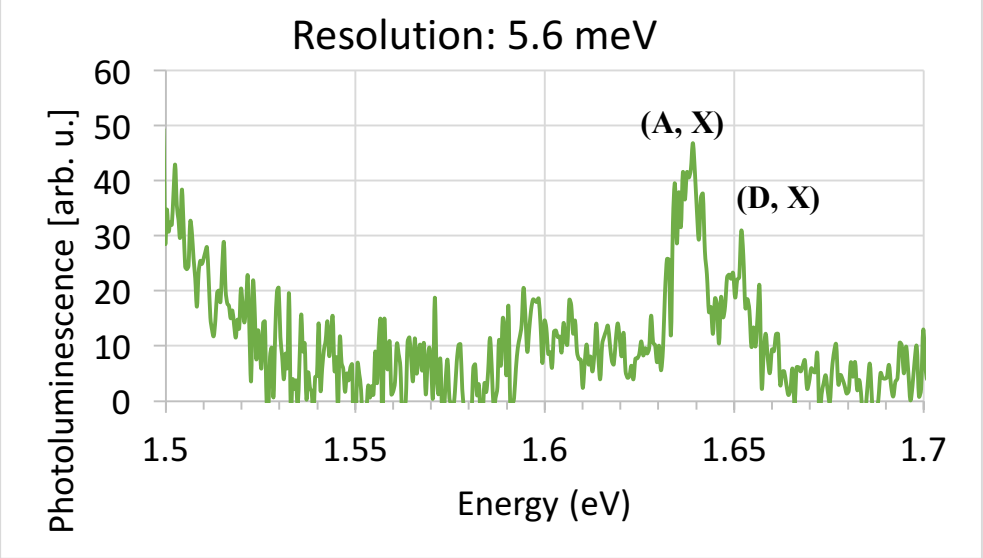

Figure 51 - Typical PL near band edge region spectrum of sample (4912-84-2) excited by a green laser at 9K using a resolution of 5.6 meV.

When sample (4912-84-2) is excited with the green laser, its PL spectrum shows a donor bound exciton (D, X) peak is situated at 1.651 eV. The acceptor bound exciton (A, X) is located at the shoulder of the lower energy side at 1.638 eV. The shallow donor acceptor pair DAP emission and its longitudinal optical phonon replica LO peak also exist. Additionally, the frequently found $D_{complex}$ wide peak is present at 1.46 eV. I(D, X)/I($D_{complex}$) is 0.319, I(A, X)/I($D_{complex}$) is 0.588, I(D, X)/I(A, X) is 0.543.

A.2 Sample 4762-85-1

A.2.1 Green Excitation

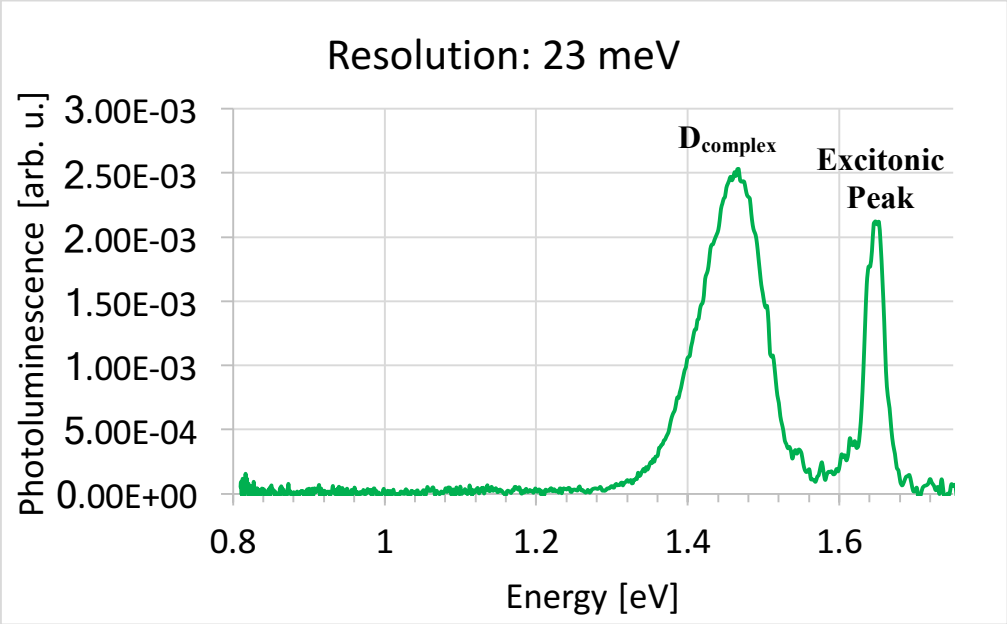

Figure 52 - PL spectrum of sample (4762-85-1) excited by a green laser at 9K temperature using a resolution of 23 meV.

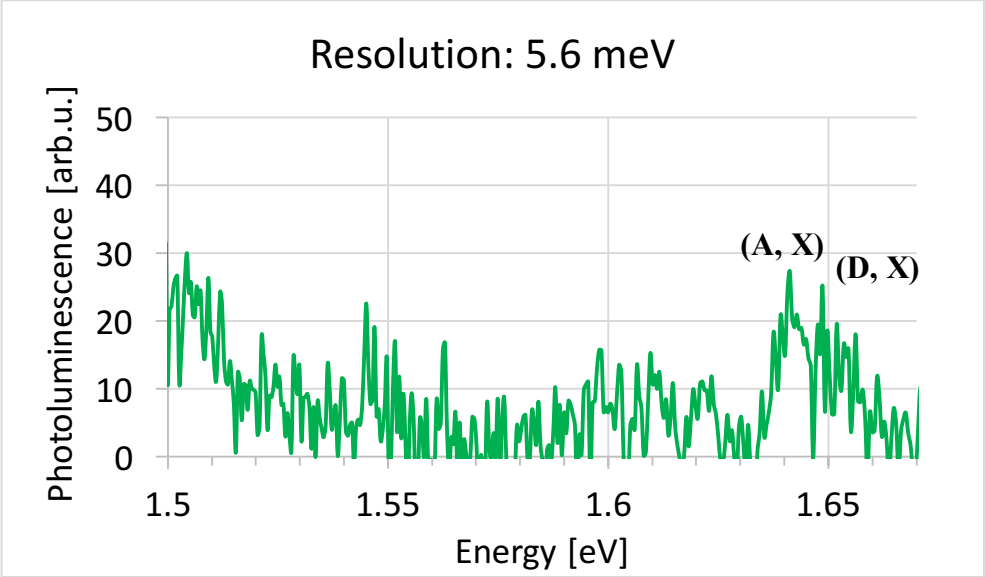

Figure 53 - Typical PL near band edge region spectrum of sample (4762-85-1) excited by a green laser at 9K using a resolution of 5.6 meV.

When Sample (4762-85-1) is excited with the green laser, its PL spectrum shows a donor bound exciton (D, X) peak is situated at 1.653 eV. The acceptor bound exciton (A, X) is located at the shoulder of the lower energy side at 1.642 eV. Additionally, the frequently found $D_{complex}$ wide peak is present at 1.465 eV. I(D, X)/I($D_{complex}$) is 0.662, I(A, X)/I($D_{complex}$) is 0.833, I(D, X)/I(A, X) is 0.794.

A.3 Sample 4392-98-2

A.3.1 Green Excitation

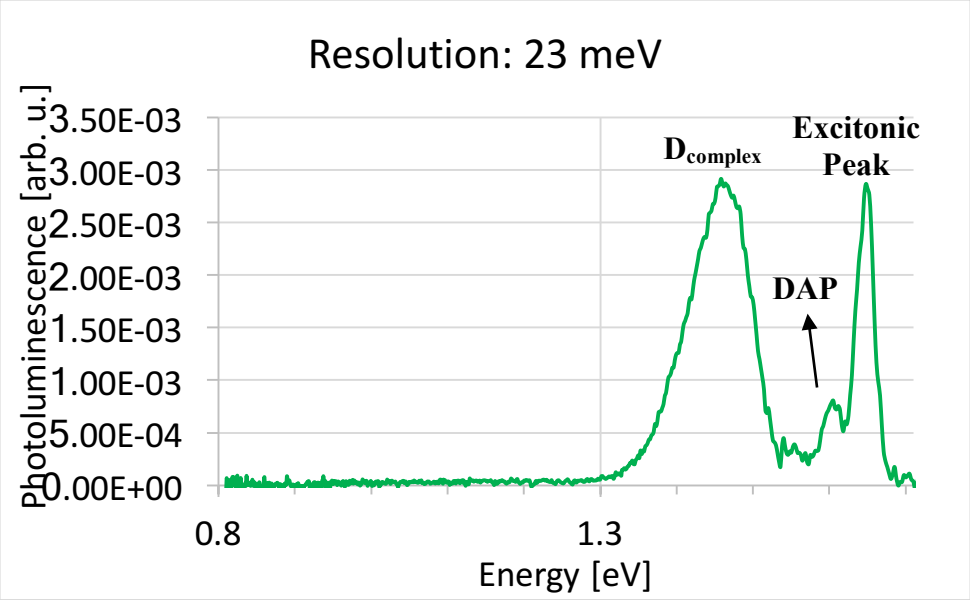

Figure 54 - PL spectrum of sample (4392-98-2) excited by a green laser at 9K temperature using a resolution of 23 meV.

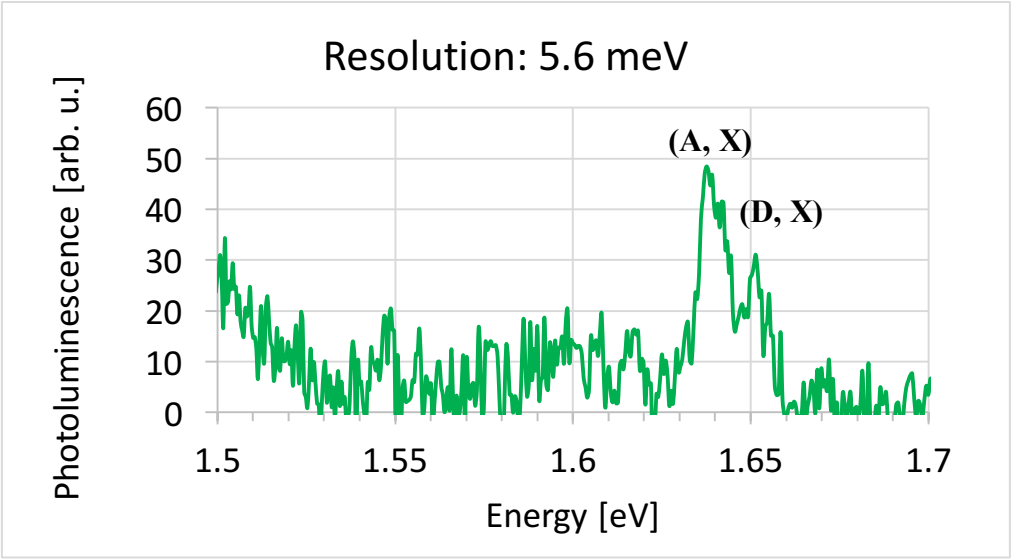

Figure 55 - PL near band edge region spectrum of sample (4392-98-2) excited by a green laser at 9K using a resolution of 5.6 meV.

When sample (4392-98-2) is excited with the green laser, its PL spectrum shows a donor bound exciton (D, X) peak is situated at 1.652 eV. The acceptor bound exciton (A, X) is located at the shoulder of the lower energy side at 1.639 eV. The shallow donor acceptor pair DAP emission at 1.61 eV and its longitudinal optical phonon replica LO peak, also exist. Additionally, the frequently found $D_{complex}$ wide peak is present at 1.46 eV. I(D, X)/I($D_{complex}$) is 0.625, I(A, X)/I($D_{complex}$) is 0.98, I(D, X)/I(A, X) is 0.641.

A.4 Sample 4392-94-4

A.4.1 Green Excitation

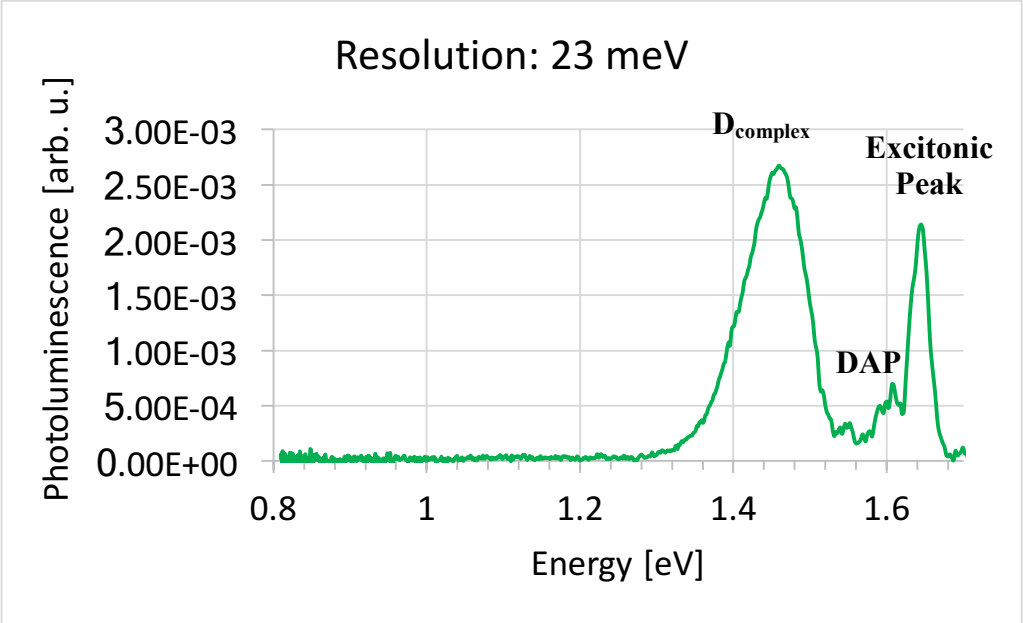

Figure 56 - PL spectrum of sample (4392-94-4) excited by a green laser at 9K temperature using a resolution of 23 meV.

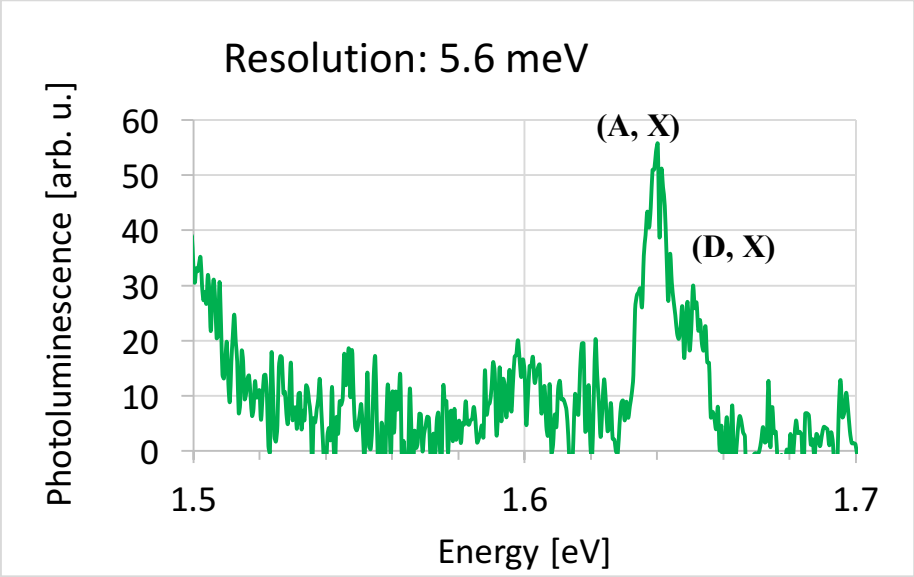

Figure 57 - Typical PL near band edge region spectrum of sample (4392-94-4) excited by a green laser at 9K using a resolution of 5.6 meV.

When sample (4392-94-4) is excited with green laser, its PL spectrum shows a donor bound exciton (D, X) peak is situated at 1.651 eV. The acceptor bound exciton (A, X) is located at the shoulder of the lower energy side at 1.641 eV. The shallow donor acceptor pair DAP emission and its longitudinal optical phonon replica LO peak, also exist. Additionally, the frequently found $D_{complex}$ wide peak is present at 1.462 eV. I(D, X)/I($D_{complex}$) is 0.429, I(A, X)/I($D_{complex}$) is 0.8, I(D, X)/I(A, X) is 0.538.

A.5 Sample 4272-98-1

A.5.1 Green Excitation

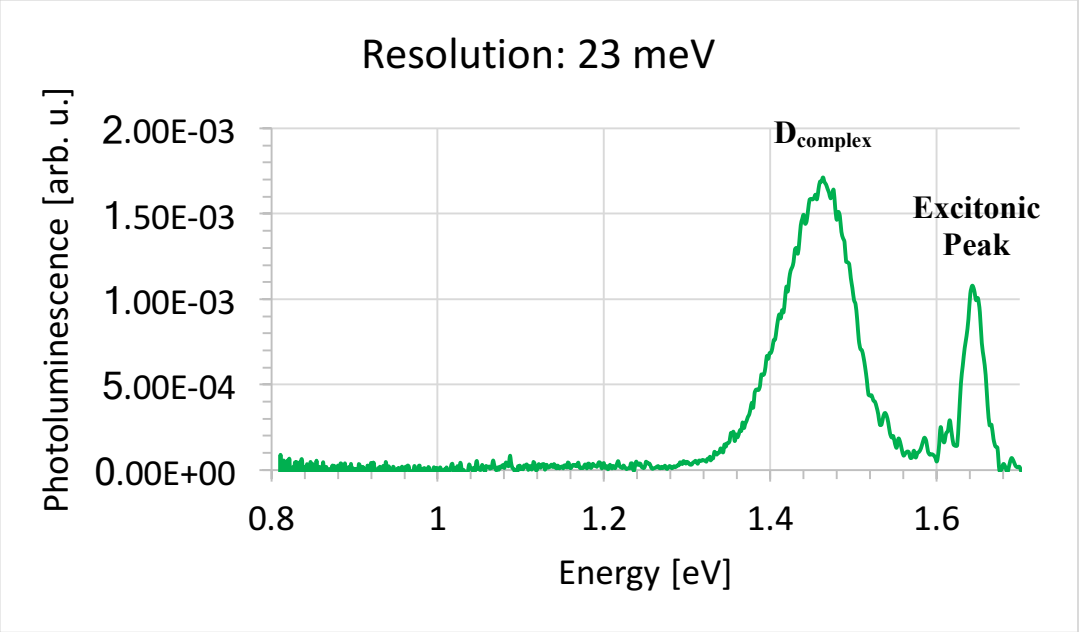

Figure 58 - PL spectrum of sample (4272-98-1) excited by a green laser at 9K temperature using a resolution of 23 meV.

A.5.2 Blue Excitation

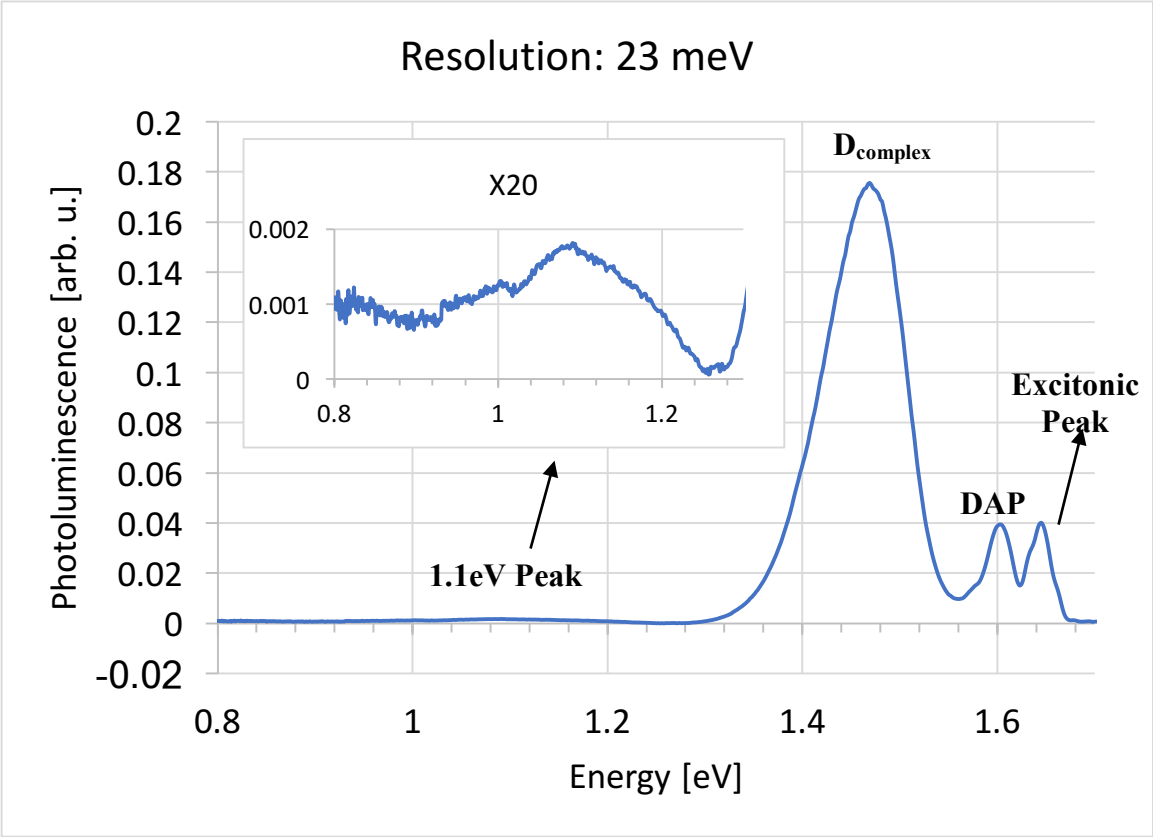

Figure 59 - PL spectrum of Sample (4272-98-1) excited by a blue laser at 9K temperature, using a resolution of 23 meV.

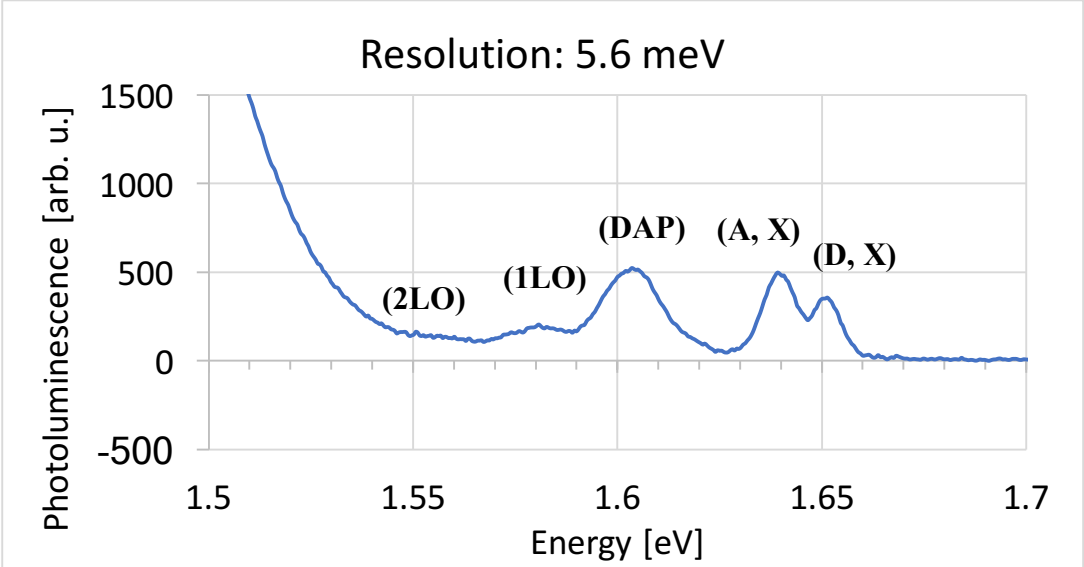

Figure 60 - Typical PL near band edge region spectrum of sample (4272-98-1) excited by a blue laser at 9K using a resolution of 5.6 meV.

When sample (4272-98-1) is excited with the green laser, its PL spectra show a donor bound exciton (D, X) peak is situated at 1.65 eV. The acceptor bound exciton (A, X) is located at the shoulder of the lower energy side at 1.639 eV. The shallow donor acceptor pair DAP emission and its longitudinal optical phonon replica LO peak. Additionally, the frequently found $D_{complex}$ wide peak is present at 1.463 eV. I(D, X)/I($D_{complex}$) is 0.356, I(A, X)/I($D_{complex}$) is 0.629, I(D, X)/I(A, X) is 0.565.

When exciting the sample with the blue laser, the PL spectra reveal a donor bound exciton (D, X) peak located at 1.651 eV. The acceptor bound exciton (A, X) is situated at 1.64 eV. The shallow donor acceptor pair DAP emission at 1.607 eV, and their longitudinal optical phonon replicas LO peaks at 1.582 eV are also present. Additionally, the $D_{complex}$ wide peak exists at 1.469 eV. The 1.1eV deep level defect peak is detected. I(D, X)/I($D_{complex}$) is 0.163, I(A, X)/I($D_{complex}$) is 0.229, I(D, X)/I(A, X) is 0.714, I(DAP)/I($D_{complex}$) is 0.24, and I(1.1eV)/I($D_{complex}$) is 0.01008.

A.6 Sample 4746-84-1

A.6.1 Green Excitation

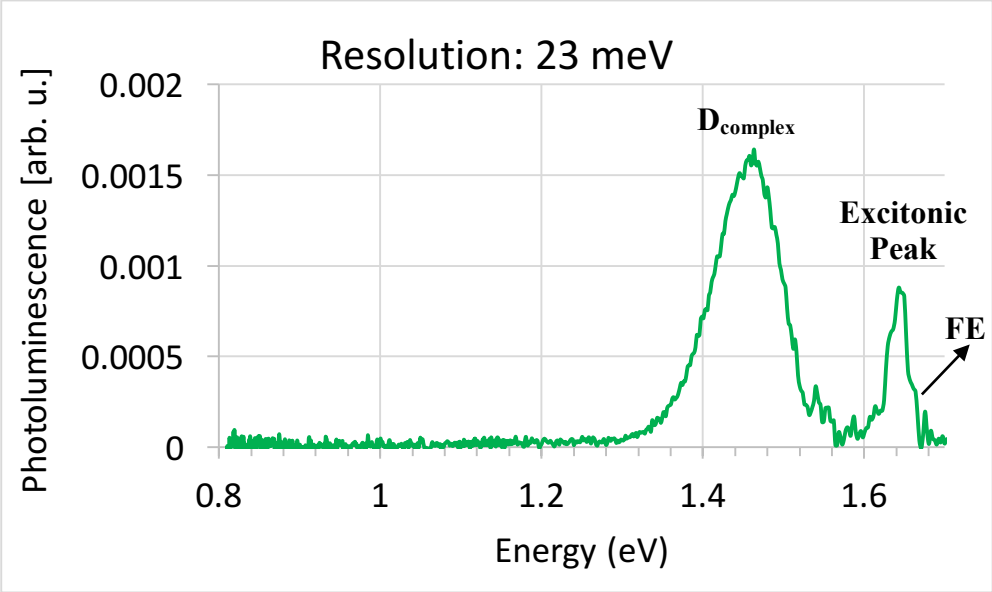

Figure 61 - PL spectrum of sample (4746-84-1) excited by a green laser at 9K temperature using a resolution of 23 meV.

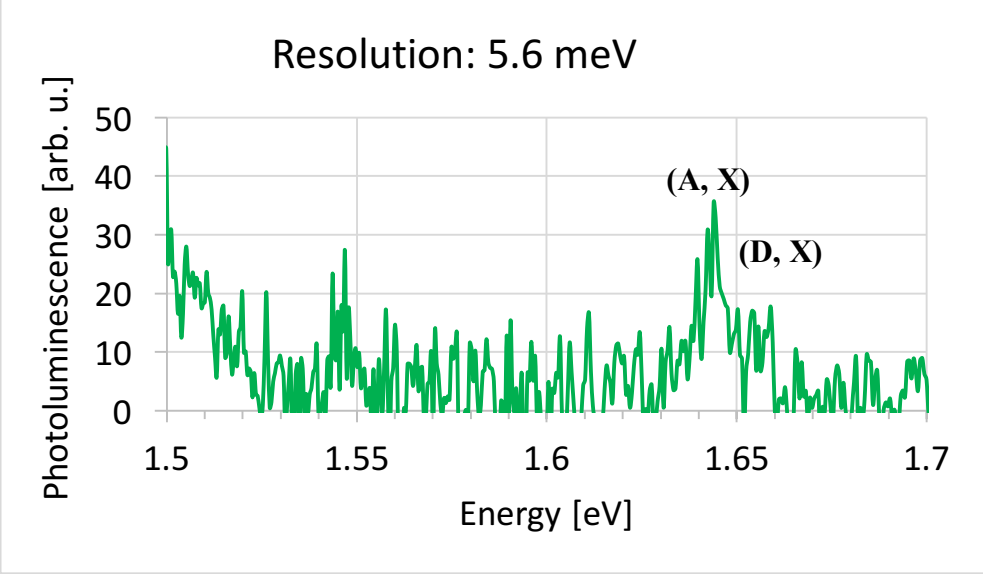

Figure 62 - Typical PL near band edge region spectrum of sample (4746-84-1) excited by a green laser at 9K using a resolution of 5.6 meV.

When sample (4746-84-1) is excited with the green laser, its PL spectrum shows a donor bound exciton (D, X) peak is situated at 1.656eV. The acceptor bound exciton (A, X) is located at the shoulder of the lower energy side at 1.644 eV. The free exciton peak (FE) is observed from the neutral donor bound exciton, indicating that the CZT crystal possesses high quality. Additionally, the frequently found $D_{complex}$ wide peak is present at 1.463 eV. I(D, X)/I($D_{complex}$) is 0.302, I(A, X)/I($D_{complex}$) is 0.549, I(D, X)/I(A, X) is 0.55.

A.7 Sample 4272-98-6

A.7.1 Green Excitation

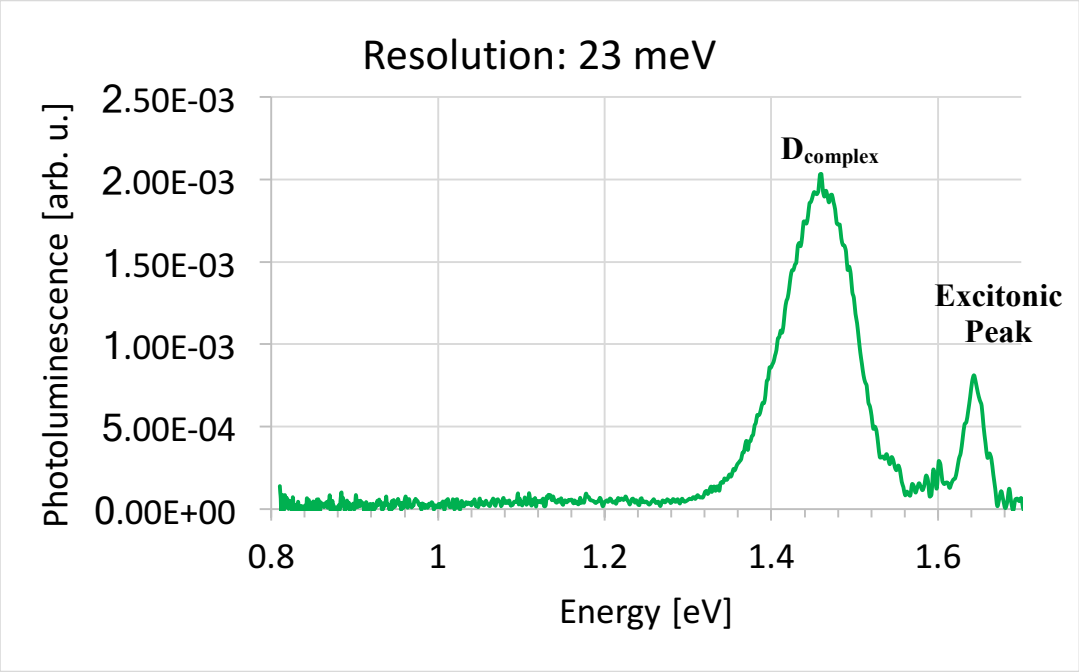

Figure 63 - PL spectrum of sample (4272-98-6) excited by a green laser at 9K temperature using a resolution of 23 meV.

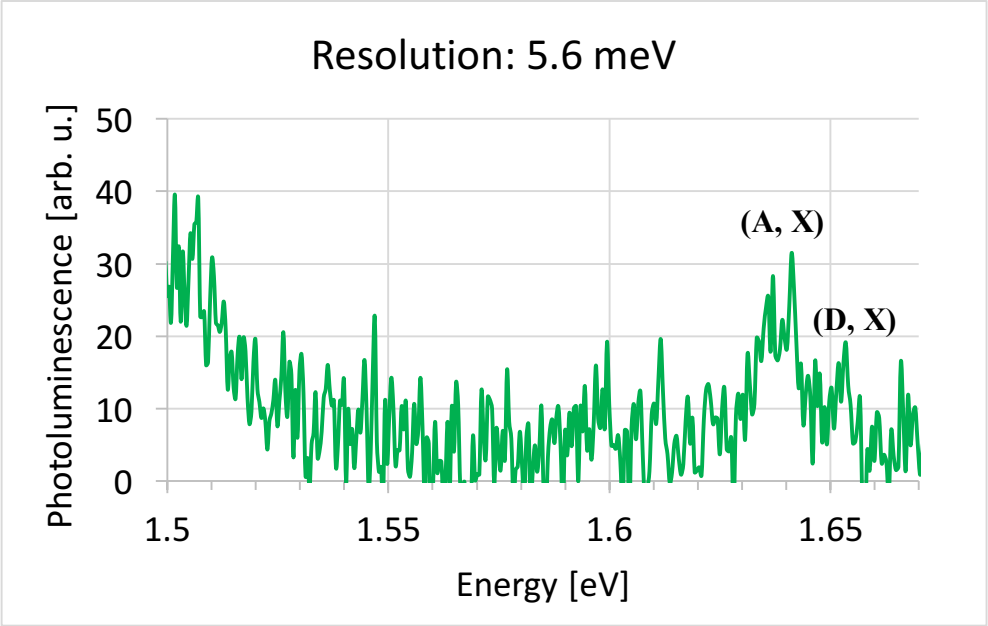

Figure 64 - Typical PL near band edge region spectrum of sample (4272-98-6) excited by a green laser at 9K using a resolution of 5.6 meV.

A.7.2 Blue Excitation

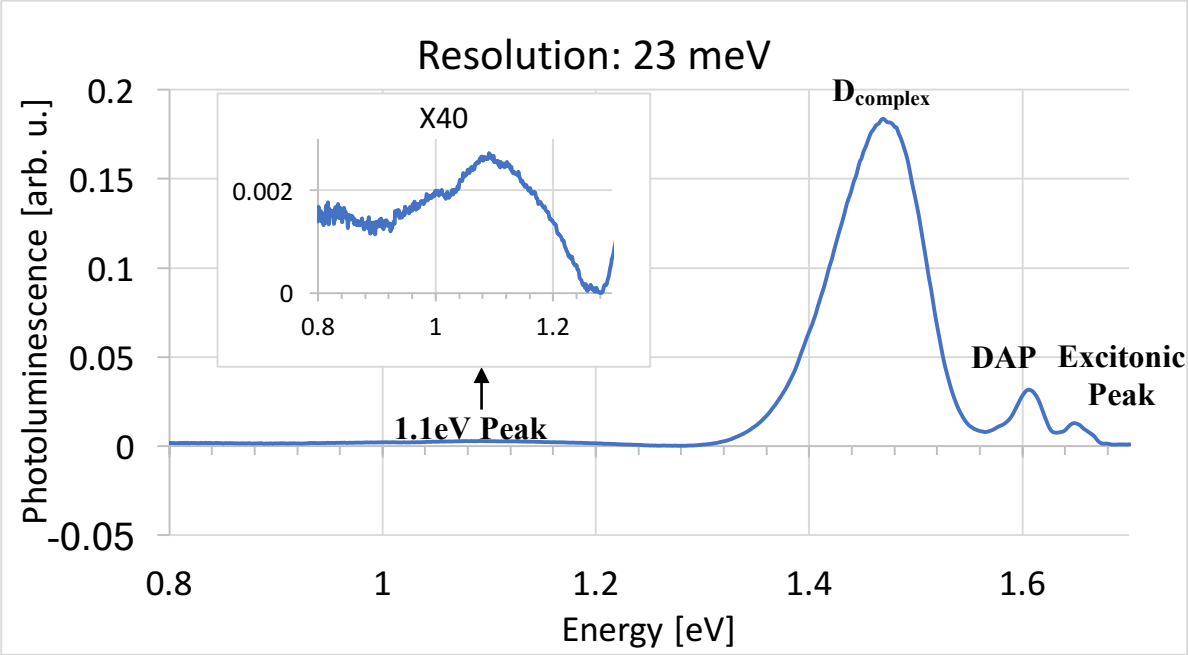

Figure 65 - PL spectrum of Sample (4272-98-6) excited by a blue at 9K temperature using a resolution of 23 meV.

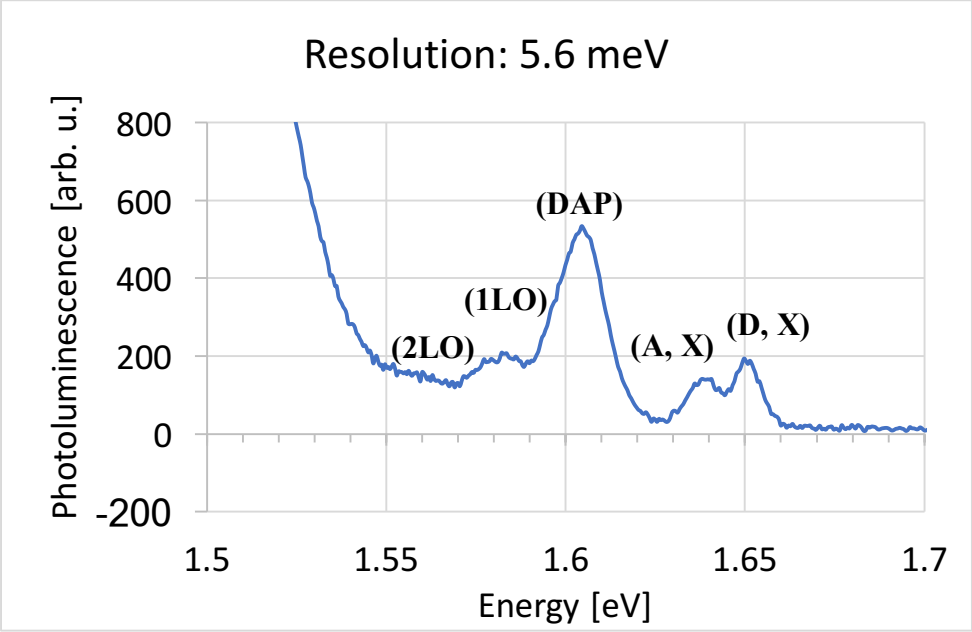

Figure 66 - Typical PL near band edge region spectrum of sample (4272-98-6) excited by a blue laser at 10K using a resolution of 5.6 meV.

When sample (4272-98-6) is excited with the green laser, its PL spectrum shows a donor bound exciton (D, X) peak is situated at 1.653 eV. The acceptor bound exciton (A, X) is located at the shoulder of the lower energy side at 1.639 eV. The free exciton peak is observed from the neutral donor bound exciton, indicating that the CZT crystal possesses high quality. The shallow donor acceptor pair DAP emission and its longitudinal optical phonon replica LO peak, also exist. Additionally, the frequently found $D_{complex}$ wide peak is present at 1.462 eV. I(D, X)/I($D_{complex}$) is 0.246, I(A, X)/I($D_{complex}$) is 0.42, I(D, X)/I(A, X) is 0.585.

When exciting the sample with the blue laser, the PL spectrum reveals a donor bound exciton (D, X) peak located at 1.651 eV. The acceptor bound exciton (A, X) is situated at 1.639 eV. The shallow donor acceptor pair DAP emission at 1.606 eV and its longitudinal optical phonon replica LO peak at 1.581 eV, are also present. Additionally, the $D_{complex}$ wide peak exists at 1.473 eV. Meanwhile, the 1.1eV deep level defect peak is detected. I(D, X)/I($D_{complex}$) is 0.069, I(A, X)/I($D_{complex}$) is 0.052, I(D, X)/I(A, X) is 1.33, I(DAP)/I($D_{complex}$) is 0.2, and I(1.1eV)/I($D_{complex}$) is 0.0142.